

EVALUATING MINERALOGY AT TERRESTRIAL ANALOGS FOR EARLY MARS:
DETECTION AND CHARACTERIZATION OF CLAYS WITH XRD AND INVESTIGATION OF
IRON SUBSTITUTION IN NATROALUNITE

by

LAURA GRACE BECKERMAN

B.A., Northwestern University, 2013

A thesis submitted to the
Faculty of the Graduate School of the
University of Colorado in partial fulfillment
of the requirement for the degree of
Master of Science
Department of Geological Sciences

2016

This thesis entitled "Evaluating Mineralogy at Terrestrial Analogs for Early Mars: Detection and Characterization of Clays with XRD and Investigation of Iron Substitution in Natroalunite"
written by Laura Grace Beckerman
has been approved for the Department of Geological Sciences

Dr. Brian Hynek

Dr. Julio Sepulveda

Dr. Alexis Templeton

Date_____

The final copy of this thesis has been examined by the signatories, and we find that both the content and the form meet acceptable presentation standards of scholarly work in the above mentioned discipline.

ABSTRACT

Beckerman, Laura Grace (M.S., Geological Sciences)

Evaluating Mineralogy at Terrestrial Analogs for Early Mars: Detection and Characterization of Clays with XRD and Investigation of Iron Substitution in Natroalunite

Thesis directed by Associate Professor Brian M. Hynek

The Mars Science Laboratory (MSL) Curiosity rover is equipped with CheMin, the first x-ray diffraction (XRD) instrument on Mars, for *in situ* mineralogy as part of its mission to seek evidence of past habitability at Gale Crater. Detection and characterization of hydrated minerals like clays and sulfates provides crucial insight into Mars' early geochemistry. For example, clays are often interpreted as having formed in lacustrine environments at neutral pHs, while sulfates such as jarosite are evidence of acid sulfate alteration.

However, CheMin's inability to remove non-clay minerals and to preferentially orient samples may pose significant challenges to clay detection and characterization at Gale Crater. To evaluate the effect of particle size separation (<0.2 μm), removal of non-clay minerals, preferred orientation, and ethylene glycol solvation on XRD analyses of clays, we used both a CheMin analog instrument and a traditional laboratory XRD to identify clays in acid sulfate altered basalt from Mars analog sites in Costa Rica. We detected kaolinite in four of the fourteen samples studied, one of which also contained montmorillonite. Kaolinite was not detected in two samples with the analog instrument prior to clay isolation. These results suggest that CheMin may miss detection of some clays at Gale Crater, which could affect interpretations of early Mars' habitability.

Mistaking iron-rich natroalunite ($\text{Na}[\text{Al},\text{Fe}]_3(\text{SO}_4)_2(\text{OH})_6$) for jarosite ($\text{KFe}_3(\text{SO}_4)_2(\text{OH})_6$) could also impact interpretations of early Mars, as natroalunite can form over a broader range of pH, water:rock ratios, and redox conditions than can jarosite. To determine if iron-rich natroalunite is a common alteration product at Mars analog sites, we assessed iron content in

natroalunite from Costa Rica. We detected up to ~30% iron substitution in natroalunite at diverse geochemical settings. We also evaluated the feasibility of using XRD or Raman spectroscopy for *in situ* iron-rich natroalunite detection, and determined that CheMin on Curiosity and the Raman Laser Spectrometer on the upcoming ExoMars rover could detect natroalunite with $\geq 25\%$ iron substitution. Distinguishing between iron-rich natroalunite and jarosite with CheMin could aid in interpreting geochemical conditions and habitability at Gale Crater.

ACKNOWLEDGMENTS

I would like to thank my advisor, Dr. Brian Hynek, for his constant guidance and support throughout my graduate work. I am also grateful for the mentorship of Alexis Templeton, whose feedback helped shape my iron-rich natroalunite investigation. I would also like to thank Dr. Tom McCollom for the use of his natroalunite-natrojarosite standards for my Raman spectroscopy work and his assistance with the SEM, Dr. Lindsay McHenry for her guidance on the clay isolation procedure, and Rachael Hoover for her help with figuring out how to tackle the clay isolation process, and then for making it happen. I am thankful for Graham Lau and Elly Schofield, my stalwart supports through the highs and lows of graduate school, and Sarah Black, my fellow graduate student in the small but mighty Hynek lab, for their advice and friendship. Thanks also go to everyone who read early drafts and provided constructive criticism, especially Xanda Schofield, who also let me borrow her laptop when mine had technical difficulties. Finally, I would like to thank the National Science Foundation Graduate Student Fellowship Award (No. DGE 1144083) for providing financial support for my graduate school career.

CONTENTS

CHAPTER ONE: INTRODUCTION

- 1.1 Search for Life on Mars
 - 1.1.1 Early Observations of Mars
 - 1.1.2 The Viking Mission: 1970s
 - 1.1.3 Follow the Water: 1990s and 2000s
 - 1.1.4 Explore Habitability: 2010s
 - 1.1.5 Seek Signs of Life: 2020s
- 1.2 Mars' Geologic History and Habitability
- 1.3 Investigating Mars' Geologic History with Mineralogy
 - 1.3.1 Phyllosilicates
 - 1.3.2 Sulfates
- 1.4 Mars Analog Sites
- 1.5 Motivation for this Thesis
- 1.6 Thesis Structure

CHAPTER TWO: DETECTION AND CHARACTERIZATION OF CLAYS ON MARS WITH XRD: INSIGHTS FROM CLAY-SPECIFIC XRD PREPARATION PROCEDURES ON SAMPLES FROM A HYDROTHERMAL ANALOG STUDY

- 2.1 Abstract
- 2.2 Introduction
 - 2.2.1 Clay Detections and Formation on Mars
 - 2.2.2 Clay Characterization with XRD
- 2.3 Field Site Description and Sample Collection
- 2.4 Sample Selection
- 2.5 Methods
- 2.6 Results
 - 2.6.1 Clay Detections
 - 2.6.2 Efficacy of Non-Clay Mineral Removal
 - 2.6.3 Complications from Dispersion
 - 2.6.4 Analysis with the Terra XRD Instrument
 - 2.6.5 Ethylene Glycol Solvation
- 2.7 Discussion
 - 2.7.1 Isolation of Clays for XRD Analyses
 - 2.7.2 Implications for *In situ* Clay Analyses
 - 2.7.3 Implications for Interpreting Clay Mineral Assemblages on Mars
- 2.8 Conclusion

CHAPTER THREE: INVESTIGATING IRON SUBSTITUTION IN NATROALUNITE AT TERRESTRIAL ANALOGS FOR EARLY MARS

- 3.1 Abstract
- 3.2 Introduction
 - 3.2.1 Sulfate Detections and Formation on Mars
 - 3.2.2 Previous Work
- 3.3 Field Site Descriptions and Sample Collection

CONTENTS (cont.)

- 3.4 Methods
- 3.5 Results
 - 3.5.1 Quantitative and Semiquantitative Analyses of Iron Content
 - 3.5.2 Detecting and Estimating Iron Content with *in situ* Instruments
- 3.6 Discussion
 - 3.6.1 Iron Substitution in Natroalunite in Costa Rica
 - 3.6.2 X-ray Diffraction and Raman Spectroscopy Characterization of Fe-rich Natroalunite
 - 3.6.3 Partial Dissolution of Fe-rich Natroalunite to Form Hematite Spherules
- 3.7 Implications for Mars

CHAPTER FOUR: CONCLUSIONS

- 4.1 Characterization of the Mineral Assemblage at Poás and Turrialba
 - 4.1.1 Motivation
 - 4.1.2 Findings
 - 4.1.3 Implications
- 4.2 Detection and Characterization of Clays with XRD
 - 4.2.1 Motivation
 - 4.2.2 Findings
 - 4.2.3 Implications
- 4.3 Iron Substitution in Natroalunite at Costa Rica
 - 4.3.1 Motivation
 - 4.3.2 Findings
 - 4.3.3 Implications
- 4.4 Implications for Astrobiology
- 4.5 Recommendations for Future Work

REFERENCES

LIST OF TABLES

- 2.1 Mineralogy of samples selected for clay isolation procedure
- 2.2 Mineralogy of samples before and after clay isolation procedure
- 3.1 Alunite-jarosite group minerals
- 3.2 Mineralogy of samples selected for Fe-rich natroalunite investigation
- 3.3 Summary of EMP and SEM-EDS analyses
- 3.4 Representative compositions (elemental %) of natroalunites as determined by EMP.
- 3.5 Representative compositions (atomic % and atoms per formula unit) of natroalunites as determined by SEM.
- 3.6 Raman peak locations and approximate Fe-content in natroalunites.
- 3.7 XRD peak locations and approximate Fe-content in natroalunites.

LIST OF FIGURES

- 2.1 Context of field sites
- 2.2 Poás volcano sampling sites
- 2.3 Turrialba volcano sampling sites
- 2.4 Samples selected for clay isolation procedure
- 2.5 Terra XRD instrument
- 2.6 Poás Fluv Clay 2 diffraction patterns before and after clay isolation procedure
- 2.7 Tu N6 diffraction patterns before and after clay isolation procedure
- 2.8 Tu Center Crater 1 diffraction patterns before and after clay isolation procedure
- 2.9 Tu Center Crater 3 diffraction patterns before and after clay isolation procedure
- 3.1 Context of field sites
- 3.2 Turrialba volcano sampling sites
- 3.3 Poás volcano sampling sites
- 3.4 Samples selected for investigation of iron content in natroalunite
- 3.5 Diffraction patterns of samples selected for investigation of iron content in natroalunite
- 3.6 Backscattered electron images of representative natroalunite grains
- 3.7 Elemental maps and backscattered electron image of a Ttop6 grain
- 3.8 Elemental maps and backscattered electron image of a PF9 grain
- 3.9 Average natroalunite Raman spectra from TuN5, Ttop2, Ttop6, PDE1, and PDE3
- 3.10 Raman microscope images of Ttop6

CHAPTER ONE: INTRODUCTION

1.1 Search for Life on Mars

1.1.1 Early Observations of Mars

The possibility of life on Mars has fascinated humanity for centuries. When astronomers turned their telescopes towards Mars in the 17th and 18th centuries, they discovered this bright red spot in the sky was another planet, and began observing and mapping the polar ice caps, the light-toned “continents”, and the darker “seas.” In the 1870s, Giovanni Schiaparelli mapped a network of channels, or “canali,” across the Martian surface. Mistranslated from the Italian into “canals,” these features were interpreted as aqueducts built by Martians to irrigate crops, and changes in surface brightness were even considered by some as evidence of plant life [Lowell, 1908]. Early science fiction authors soon captured the public’s imagination with stories of civilizations on the surface, ranging from a dying humanoid race in Ray Bradbury’s *The Martian Chronicles*, to an invading force intent on humanity’s destruction in H.G. Wells’ *The War of the Worlds*.

Exploration of Mars, and the search for Martians, began in earnest in the 1960s. When Mariner 4 reached Mars in 1965, it returned the first 20 images of Mars—a heavily cratered world almost reminiscent of the barren Moon. Subsequent Mariner fly-by and orbiter missions between 1969 and 1971 returned several hundred more photos and conducted measurements of the atmosphere’s composition, pressure, and temperature, and of the surface temperature and composition. Mariner 9 also witnessed a massive dust storm and returned images of Schiaparelli’s famous “canali,” which were revealed to be dried up fluvial channels.

1.1.2 The Viking Mission: 1970s

In the 1970s, Viking 1 and 2 arrived at Mars, equipped with instruments to detect organics or microbial life, if extant. However, results were inconclusive: the Gas Chromatograph-Mass Spectrometer (GCMS), Gas Exchange experiment, and Pyrolytic Release experiment results were negative, but the Labelled Release (LR) experiment on each lander had positive results [Levin and Straat, 1976, 1979]. Re-analysis of Viking GCMS data suggested that chlorinated hydrocarbon detections were not due to terrestrial contamination as initially believed, but were formed during the heating of Martian organics and perchlorates also in the soil [Navarro-González *et al.*, 2010]. Scientific consensus, however, considers the LR experiment results a false positive caused by chemistry rather than biology.

1.1.3 Follow the Water: 1990s and 2000s

Following financial concerns about space exploration in the 1980s, the Pathfinder mission in 1997 proved the feasibility of a low-cost mission to Mars. Renewed public interest led to a decade of exploration focused on searching for signs of water, the solvent required for all life on Earth. The Mars Global Surveyor (MGS) orbiter began mapping the Martian surface in 1997 [Christensen *et al.*, 1998; Albee *et al.*, 2001; Malin and Edgett, 2001; Smith *et al.*, 2001] and identified recent gullies formed by liquid water [Malin and Edgett, 2000]. MGS was soon joined by the 2001 Mars Odyssey, which continues to map the surface composition and morphology, and subsurface and exposed ice deposits [Christensen *et al.*, 2003; Titus *et al.*, 2003; Saunders *et al.*, 2004]. ESA's Mars Express followed shortly afterward and discovered phyllosilicates, sulfates, and other hydrated minerals with the Observatoire pour la Mineralogie, l'Eau, les Glaces et l'Activité (OMEGA) instrument [Bibring *et al.*, 2005; Gendrin *et al.*, 2005; Poulet *et al.*, 2005]. A few years later, NASA's Mars Reconnaissance Orbiter (MRO) arrived with the Compact Resolution Imaging Spectrometer for Mars (CRISM) for further detection and characterization of aqueous mineral assemblages [Mustard *et al.*, 2008; Ehlmann *et al.*, 2009; Murchie *et al.*, 2009]. In addition, MRO's High Resolution Imaging Science Experiment (HiRISE)

camera identified recurring slope lineae (RSL), dark lines formed by ongoing salty water runoff [McEwen *et al.*, 2011, 2013; Chevrier and Rivera-Valentin, 2012].

Back on Earth, analyses of Martian meteorites have provided further insight into the planet's aqueous geochemistry and, according to some, paleobiology. Investigations of shergottites, nakhlites, and chassignites and a water-rich basaltic breccia have revealed aqueously altered minerals and enabled estimates of water content in Martian magmas [Lentz *et al.*, 2001; Treiman, 2005; Agee *et al.*, 2013; Balta and McSween, 2013; He *et al.*, 2013]. McKay *et al.* [1996] asserted that nanometer-sized “ovoid” and “tubular” features, and polyaromatic hydrocarbons, magnetite, and iron sulfides within carbonate globules, were evidence of fossilized bacteria and microbial activity within Martian asteroid ALH84001. The paper created a whirlwind of media attention; however, the scientific consensus is that these features can be explained by inorganic processes [Anders, 1996; Bell, 1996].

Meanwhile, operating on the surface itself, the Mars Exploration Rovers Spirit and Opportunity started searching for geological clues to an aqueous past in January 2004. At Meridiani Planum, Opportunity uncovered hematite and jarosite [Klingelhöfer *et al.*, 2004; Squyres *et al.*, 2004a], and in Gusev Crater, Spirit found hydrated silica and sulfur-rich soils [McSween *et al.*, 2004; Squyres *et al.*, 2004b; Ming *et al.*, 2006; Yen *et al.*, 2008]. These mineral assemblages discovered by Spirit and Opportunity likely formed through aqueous acid sulfate alteration processes [Elwood Madden *et al.*, 2004; Squyres and Knoll, 2005; Ming *et al.*, 2006; Squyres *et al.*, 2008, 2012; Yen *et al.*, 2008]. In 2008, up in the northern lowlands, the Phoenix Mars Lander detected carbonates, perchlorates, and water ice in the soil, and observed water-ice clouds and precipitation [Hecht *et al.*, 2009; Smith *et al.*, 2009; Whiteway *et al.*, 2009]. Spirit ceased its mission in 2011, but Opportunity is still investigating signs of aqueous alteration in bedrock fractures and providing *in situ* context for orbital smectite detections [Arvidson *et al.*, 2016; Crumpler *et al.*, 2016].

1.1.4 Explore Habitability: 2010s

With the Mars Science Laboratory (MSL) mission, NASA expanded the definition of “habitability” to include not only signs of water, but also sources of carbon and energy for microbes [Grotzinger *et al.*, 2012]. Shortly after arriving at Gale Crater in August 2012, the MSL rover Curiosity explored an ancient lake bed containing elements essential to life on Earth at Yellowknife Bay [Grotzinger *et al.*, 2014]. Discoveries of organic molecules within smectite-bearing samples further support the interpretation of Gale Crater as a formerly habitable environment [Freissinet *et al.*, 2015, 2016]. Now at its main destination, Aeolis Mons or “Mount Sharp,” Curiosity has discovered evidence for another shallow lake that was once located where the ~5 km tall mountain stands today [Grotzinger *et al.*, 2015]. Recent analyses of sediments at the base of Mount Sharp reveal evidence of acid sulfate alteration [Rampe *et al.*, 2015, 2016].

Joining Mars Odyssey, Mars Express, and MRO in orbit, the Mars Atmospheric and Volatile Evolution (MAVEN) mission is studying processes in the magnetosphere, atmosphere, and ionosphere to evaluate Mars’ atmospheric loss and climate change, which will provide constraints on Mars’ past habitability [Jakosky *et al.*, 2015].

1.1.5 Seek Signs of Life: 2020s

Upcoming missions to Mars will continue the search for water and habitable environments, but with a greater focus on life detection. The first part of the ESA’s Exobiology on Mars (“ExoMars”) mission consists of a trace gas orbiter looking for methane and other possibly biogenic gases and a descent module named *Schiaparelli*, and will arrive in October 2016. The second part, a platform and rover, will study Mars’ surface environment, shallow subsurface geochemistry, and its interior, with a primary objective to seek signs of life, past or present [Vago and Kminek, 2007; Cassi, 2008]. Partly a demonstration of *in situ* resource utilization technology and partly a sample cache mission, the NASA Mars 2020 rover will also investigate habitability and seek signs of life on Mars [Mustard *et al.*, 2013]. The ExoMars and NASA 2020 rovers will both be equipped with Raman spectrometers for investigating minerals and organic

molecules, and the ExoMars rover will also have an instrument dedicated to detecting organic molecules.

1.2 Mars' Geologic History and Habitability

Roughly half the size and one-tenth of the mass of Earth, the planet Mars is coated with iron oxides, giving it a red hue. Beneath the rust, Mars has two main types of lava; type 1 is basalt, while type 2 is basaltic andesite or andesite [Bandfield, 2000]. The surface of Mars is split between northern lowlands and southern highlands. Mars' major surface features include Tharsis, a volcanic province that includes the solar system's tallest volcano, and Valles Marineris, an enormous network of graben that stretches more than 4000 km in length.

The planet's geologic history is divided into three main periods, some more conducive to life than others. Preceding these geologic eras, the Pre-Noachian extends from the planet's rapid accretion and differentiation ~4.5 Ga to the formation of the Hellas Basin ~4.1 Ga [Carr and Head, 2010b]. Pre-Noachian Mars was subjected to frequent heavy bombardment and therefore likely inhospitable on the surface, despite the presence of a strong magnetic field and warming from the repeated impacts [Acuna et al., 1999; Solomon et al., 2005; Carr and Head, 2010b]. Sleep and Zahnle [1998], however, propose that thermophilic microbes could have eked out a living deep in the subsurface during this time.

The next few hundred million years were wetter, and perhaps warmer, than conditions on Mars today. Deltas, valleys, channels, gullies, alluvial fans, and other features of flowing water have been observed across Mars [Carr, 1996; Malin and Edgett, 2003; Carr and Head, 2010a, 2010b], mainly dated to the Noachian (~4.1 to 3.7 Ga). Hundreds of craters and topographic lows likely hosted open-basin lakes fed by both precipitation and groundwater seepage [Fassett and Head, 2008]. A fluvio-lacustrine origin has also been proposed for Gale Crater [Grotzinger et al., 2014, 2015] and Meridiani Planum [Squyres et al., 2004a].

On a more global scale, an ocean covering the northern hemisphere has been proposed based on putative paleoshorelines [*Head et al.*, 1999; *Di Achille and Hynes*, 2010; *Rodriguez et al.*, 2016]. These networks and bodies of water were likely recharged via precipitation, with some contribution from groundwater [*Craddock and Howard*, 2002; *Hynes and Phillips*, 2003; *Howard et al.*, 2005]. An active hydrologic cycle, especially if long-lived, could provide a favorable environment for life and could re-circulate elements used as microbial energy sources.

Yet how valleys, lakes, or even an ocean could be sustained on Mars' surface—whether short-lived, episodic, or sustained for tens of thousands of years—remains a mystery. Models of early Mars' atmosphere have yet to produce surface temperatures and pressures that could permit liquid water. Consequently, ice- and groundwater-driven processes and subsurface hydrothermal systems have been investigated as alternative mechanisms for aqueous features observed on Mars' surface [*Carr*, 2002; *Ehlmann et al.*, 2008, 2011]. Groundwater and/or hydrothermal activity, especially in the deep subsurface, could supply carbon and cations for an active thermophilic, chemolithotrophic biosphere [*Ehlmann et al.*, 2008; *Michalski et al.*, 2013].

Evidence for valley formation, albeit at lower rates than in the Noachian, extends into the Hesperian period, which began ~3.7 Ga [*Carr and Head*, 2010b; *Hynes et al.*, 2010]. During the Hesperian, Valles Marineris may have episodically filled with water, potentially forming a habitable niche. More outflow channels are dated to the Hesperian than to the Noachian, indicating sudden floods from lakes, groundwater aquifers under pressure, or melting of ice during this period [*Carr and Head*, 2010b]. These events likely had high initial discharge rates before tapering off over several days or weeks [*Andrews-Hanna and Phillips*, 2007]; microbial communities that survived the initial torrent could have benefitted from the subsequent trickle of water. However, Mars' active hydrologic cycle may have morphed into a global cryosphere during the Hesperian, providing fewer surface environments suitable for life.

The Amazonian, the most recent geologic period, began ~3 Ga and is characterized by limited geologic activity [*Hartmann and Neukum*, 2001; *Carr and Head*, 2010b]. Arid, cold, and

highly oxidized, Mars' surface is bombarded by radiation [Hassler et al., 2014] and only occasionally reworked by impacts, volcanic activity, wind, and ice. In the absence of other active processes, Mars' fluctuating obliquity plays a more significant role, contributing to the advance and retreat of ice, glaciation, and changes in the polar caps. Currently, water ice exists at the northern and southern poles, as well as mere centimeters beneath the surface down to latitudes of 30° [Smith et al., 2009; Carr and Head, 2010b]. A few valleys have been dated to the Amazonian, and young gullies [Malin and Edgett, 2000] and RSL [McEwen et al., 2011, 2013; Chevrier and Rivera-Valentin, 2012] could indicate the existence of inhabitable brines in the subsurface.

1.3 Investigating Mars' Geologic History with Mineralogy

In addition to the geomorphic evidence for past water and detections of ice discussed in the previous section, proof of Mars' aqueous past comes from hydrated minerals, which include phyllosilicates, sulfates, hydrated or opaline silica, zeolites, iron oxides, carbonates, and nitrates. The first definitive orbital detections of hydrated minerals were of phyllosilicates and sulfates, discovered with OMEGA on Mars Express [Bibring et al., 2005; Gendrin et al., 2005; Poulet et al., 2005]. These detections revolutionized the study of Mars by revealing a history of chemical interactions between rocks and water. Further detections of hydrated minerals have been made with CRISM on MRO [Arvidson et al., 2005; Bibring et al., 2005, 2006; Gendrin et al., 2005; Langevin et al., 2005; Poulet et al., 2007; Murchie et al., 2009; Ehlmann et al., 2010].

Each discovery reveals different clues about early Mars' geochemical conditions and aqueous past. For example, phyllosilicates are often interpreted as evidence of widespread surface water at neutral pH, while sulfates such as jarosite likely formed through acid sulfate alteration processes. The characterization of each mineral within an assemblage is therefore crucial to interpreting how the mineral assemblage formed, which in turn has implications for habitability and organic matter preservation. This section provides background material on

phyllosilicates and sulfates, the two groups of hydrated minerals that are the focus of the research described in Chapters 2 and 3, respectively.

1.3.1 Phyllosilicates

Phyllosilicates are made of repeating SiO_5 units arranged in sheets and include serpentine, talc, micas, chlorites, smectites, and kaolin group minerals. The latter three groups are hereafter referred to as clays, and their *in situ* detection will be the focus of Chapter 2.

1.3.1.1 Orbital Detections

Orbital detections of phyllosilicates have identified Fe,Mg smectites in 75% of locations where hydrated silicates are found [Poulet *et al.*, 2005; Mustard *et al.*, 2008; Ehlmann *et al.*, 2011, 2013], although mixed-layer clays may also be included in that count. Chlorites are the second most abundant clay detected [Ehlmann *et al.*, 2013]. Al phyllosilicates are less widespread than Fe,Mg smectites and chlorites are, and usually include kaolin family minerals, although Al smectites like montmorillonite are also found on Mars [Poulet *et al.*, 2005; Ehlmann *et al.*, 2011, 2013]. Where Al phyllosilicates occur, they are often found in strata above Fe,Mg smectites [Mustard *et al.*, 2008; Ehlmann *et al.*, 2013]. Most phyllosilicates are found in Noachian terrains.

1.3.1.2 *In situ* Observations and Detections

With the Alpha Particle X-Ray Spectrometer (APXS), the Opportunity rover is currently investigating Fe(III) smectites at Endeavour Crater that were observed from orbit [Wray *et al.*, 2009; Noe Dobrea *et al.*, 2012; Arvidson *et al.*, 2014; Crumpler *et al.*, 2016]. Based on APXS data, the mineral assemblage also includes a substantial amount of Al smectite, as well as calcium sulfates and silica [Arvidson *et al.*, 2014].

In 2013, the Curiosity rover detected an Fe,Mg smectite at Gale Crater [Vaniman *et al.*, 2014]. This smectite, inferred to be a ferrian saponite, comprised ~20 wt% of two samples at Yellowknife Bay. Phyllosilicates have also been detected en route to Mt. Sharp in the Kimberley Formation [Treiman *et al.*, 2016] and at the base of Mt. Sharp in the Murray Formation

[Cavanagh *et al.*, 2015; Rampe *et al.*, 2015, 2016]. These detections were made with CheMin, an instrument specifically intended for analysis of mineral assemblages [Blake *et al.*, 2012].

Chapter 2 will examine the capability of CheMin to detect clays *in situ*.

1.3.1.3 Formation

Characterization of a clay and its associated mineral assemblage can provide insight into the geochemical conditions at the time of deposition. The formation of a particular clay and co-deposited minerals depends on a variety of factors, including thermodynamic variables, such as temperature and pressure, kinetics, and atmospheric chemistry, if formed on the surface [Ehlmann *et al.*, 2011, 2013]. Water chemistry, such as whether the system is open or closed, water-rock ratios, pH, ion activity, and oxidation state, plays a particularly crucial role in clay formation [Ehlmann *et al.*, 2011, 2013]. On Earth, smectite formation is generally favored in closed systems where soluble ions can be retained due to low water-rock ratios [Eberl *et al.*, 1984; Ehlmann *et al.*, 2011]. Drier environments that favor smectites also favor the formation of evaporites and organic material preservation. Open systems with higher water-rock ratios where Si and Al are retained tend to produce Al-rich clays such as kaolinite and montmorillonite [Eberl *et al.*, 1984].

Although different formation mechanisms likely operated across early Mars, several theories have been proposed to explain how and when the majority of clays formed. By comparison to many terrestrial clay deposits, clays on Mars may have formed in lacustrine environments at neutral pH [e.g., Bibring *et al.*, 2006]. An alternative hypothesis is that Fe,Mg smectites and chlorites formed in the subsurface in hydrothermal groundwater-driven systems [Ehlmann *et al.*, 2011]. Although clays are generally considered evidence of neutral pH, at least some clay deposits likely formed through acid sulfate alteration, such as the mineral assemblages at Noctis Labyrinthus [Weitz *et al.*, 2011; Thollot *et al.*, 2012], Columbus Crater [Wray *et al.*, 2011], and Cross Crater [Ehlmann *et al.*, 2016].

1.3.1.4 Implications for Habitability and Organic Matter Preservation

The mechanisms of clay formation on Mars also have implications for habitability. Surface weathering processes and *in situ* precipitation require a long-lived water source, which could have supported a sustained habitable environment concurrent with clay formation [e.g., *Grotzinger et al.*, 2014]. Alternatively, if clays formed in closed, subsurface, low-grade hydrothermal systems, chemoautotrophic organisms may have had sufficient water and energy sources for an active biosphere similar to that in Earth's subsurface [*Sleep and Zahnle*, 1998; *Cockell and Barlow*, 2002; *Ehlmann et al.*, 2011]. At sites where clays formed alongside sulfates via acid sulfate alteration, acidophiles could have survived in the low pHs [e.g., *Pace*, 1997].

Fine-grained sediments like clays also can foster long-term organic matter preservation. Organic molecules can bind to charged mineral surfaces of phyllosilicates or be incorporated within the clay structure during formation [*Farmer and Des Marais*, 1999]. Organic matter preservation on Mars faces significant challenges, however, including high levels of near-surface radiation, perchlorates in the soil, and the potential for deep burial, metamorphism, or diagenesis [e.g., *Farmer and Des Marais*, 1999; *Archer et al.*, 2014; *Hassler et al.*, 2014]. Despite these obstacles to organic molecules, Viking detected two chlorinated hydrocarbons [*Biemann et al.*, 1976; *Navarro-González et al.*, 2010], and the Sample Analysis at Mars instrument suite on Curiosity has detected chlorinated and non-chlorinated hydrocarbons at Gale Crater [*Freissinet et al.*, 2015, 2016]. Further investigation will hopefully provide insight into whether these molecules are exogenous or endogenous to Mars, and whether they could indicate an ancient biosphere.

1.3.2 Sulfates

Sulfate minerals contain one or more sulfate (SO_4^{2-}) anions and range in water content from anhydrous (e.g. anhydrite: CaSO_4) to poly-hydrated (e.g. gypsum: $\text{CaSO}_4 \cdot 2\text{H}_2\text{O}$). One particular group of sulfates, the alunite-jarosite group, will be the focus of Chapter 3.

1.3.2.1 *In situ* Detections

Unlike clays, sulfates were first discovered on Mars *in situ*. Shortly after arriving at Meridiani Planum, Opportunity found a jarosite-rich outcrop with Mössbauer spectroscopy [Klingelhöfer *et al.*, 2004]. With its Miniature Thermal Emission Spectrometer, Opportunity also found Ca and Mg sulfates [Christensen *et al.*, 2004]. At Gusev Crater, Spirit found sulfate-rich soil at the Columbia Hills [Gellert *et al.*, 2006; Ming *et al.*, 2006; Morris *et al.*, 2006; Squyres *et al.*, 2006; Yen *et al.*, 2008; Arvidson *et al.*, 2010].

More recently, Curiosity has detected minor amounts of anhydrite, bassanite, and jarosite with CheMin at Yellowknife Bay [Bish *et al.*, 2013; Vaniman *et al.*, 2014] and in the Kimberley Formation [Treiman *et al.*, 2016]. At the base of Mt. Sharp, Curiosity has now discovered more significant amounts of jarosite in the basal section of the Murray Formation [Cavanagh *et al.*, 2015; Rampe *et al.*, 2015, 2016]. Chapter 3 will investigate iron-rich natroalunite, an intermediate member of the alunite-jarosite group, and will evaluate the feasibility of distinguishing between iron-rich natroalunite and jarosite *in situ*.

1.3.2.2 Orbital Detections

Mainly found in Hesperian terrains, numerous detections of gypsum, kieserite, and additional mono- and polyhydrated Ca and Mg sulfates have also been made from orbit [Arvidson *et al.*, 2005; Bibring *et al.*, 2005, 2006; Gendrin *et al.*, 2005; Langevin *et al.*, 2005; Poulet *et al.*, 2007; Murchie *et al.*, 2009]. Ferric sulfates have been identified in Mars at Aram Chaos [Lichtenberg *et al.*, 2010] and within layered deposits of Valles Marineris [Weitz *et al.*, 2010], and jarosite in particular has been detected at Mawrth Vallis [Farrand *et al.*, 2009], Northeast Syrtis Major [Ehlmann and Mustard, 2012], Noctis Labyrinthus [Weitz *et al.*, 2011; Tholot *et al.*, 2012], and Columbus Crater [Wray *et al.*, 2011]. Alunite has also been found in Columbus Crater [Wray *et al.*, 2011] and in nearby Cross Crater [Ehlmann *et al.*, 2016].

1.3.2.3 Formation

Several main mechanisms for sulfate formation have been proposed to explain sulfate deposits on Mars, particularly at Meridiani Planum, Gusev Crater, and Gale Crater. Each of the possible processes has different implications for Mars' geochemistry and aqueous history. One possible formation mechanism for ferric sulfates formed at Meridiani Planum is sulfide oxidation, which is frequently associated with acid mine drainage and is well studied at the Río Tinto in Spain [*Fernández-Remolar et al.*, 2005; *Dehouck et al.*, 2012]. This option would indicate abundant sulfide-rich basalt and either highly oxidizing conditions or microbial mediation. The Mars Exploration Rover (MER) team proposed that the mineral assemblage at Meridiani Planum formed through evaporation of acid saline lakes [*Squyres et al.*, 2004a], which requires an early atmosphere conducive to sustained lakes.

Alternatively, circulation and release of hydrothermal groundwaters interacting with H₂S or SO₂ would not require long-lived surface waters. The migration of acid sulfate fluids was recently proposed to explain the mineral assemblage in the Murray Formation at Gale Crater [*Rampe et al.*, 2015, 2016]. Acid sulfate alteration could also occur in even more water-limited conditions through sulfur-rich fumarolic activity [*McCullom and Hynek*, 2005] or “acid fog” [*Banin et al.*, 1997; *Tosca*, 2004]. As with the varied mechanisms for clay formation, these mechanisms for sulfate formation may have operated at different places and different times on the Martian surface.

1.3.2.4 Implications for Habitability and Organic Matter Preservation

Regardless of the particular mechanism, sulfate formation almost certainly required acidic conditions. This would not deter acidophiles, however, who could have thrived in these low pHs. On Earth, thermophiles survive in hydrothermal acid sulfate environments [e.g., *Pace*, 1997], and microbes can also survive periodic desiccation, such as through the evaporation of acid saline lakes [*Benison and Bowen*, 2006]. Sulfide oxidation on Earth is frequently biologically mediated, although this mechanism is less likely to explain Mars' abundant sulfates

due to the absence of large buried sulfide deposits. Sulfates are generally considered not as conducive to long-term organic matter preservation as are clays [*Farmer and Des Marais*, 1999; *Sumner*, 2004; *Fairén et al.*, 2010], but amino acids and their degradation products have been found in ancient deposits of jarosite, gypsum, and anhydrite on Earth [*Aubrey et al.*, 2006].

1.4 Mars Analog Sites

A Mars analog site is a place on Earth with climatic, geomorphological and/or geochemical processes similar to a site on past or present Mars. Studying terrestrial mineral assemblages comparable to those observed from orbit or *in situ* can help “ground-truth” interpretations of their Martian equivalents. At an analog site, water-rock ratios, pH, and temperature can be measured, and parent rock lithology, reaction pathways, and alteration products can be characterized with a suite of instruments both *in situ* and in the laboratory. By constraining the formation and context of a mineral assemblage, and conducting detailed evaluation of key hydrated minerals, this thesis can contribute to the ever-expanding understanding of early Mars’ geochemistry.

Spread across the seven continents, terrestrial analog sites are used to represent Martian environments from the earliest Noachian to the Amazonian. The annual Arctic Mars Analog Svalbard Expedition (AMASE) to Svalbard, Norway investigates geochemical processes and formations, including carbonate globules similar to those in ALH84001 [*McKay et al.*, 1996], in an example of glacial, formerly volcanically active Mars with instruments currently in use or in development for Mars missions [e.g., *Amundsen et al.*, 2010; *Stern et al.*, 2013]. The Río Tinto in Spain, named for its red color from high ferric iron concentrations, is often invoked as an analog for sulfate and iron oxide mineral assemblages on Mars, including those at Meridiani Planum [*Fernández-Remolar et al.*, 2005, 2009; *Amils et al.*, 2007]. Ongoing volcanism at Kilauea, Hawaii, is compared to ancient volcanism on Mars and studied for the geophysics of the eruptions and lava flows, geochemistry of the fresh basalt and ash, and the subsequent

weathering processes producing silica and other hydrated minerals [Farr, 2004; Seelos *et al.*, 2010; McCanta *et al.*, 2014]. The McMurdo Dry Valleys in Antarctica [Doran *et al.*, 2010], the Mojave Desert in the United States [e.g., Peters *et al.*, 2008], and the Atacama Desert in Chile [Navarro-González *et al.*, 2003; Azua-Bustos *et al.*, 2012] are among the coldest, driest locations on Earth and serve as examples of modern Mars [Marlow *et al.*, 2008; Fairén *et al.*, 2010]. These well-studied field sites are only a few of the dozens of Mars analog environments under investigation.

1.5 Motivation for this Thesis

The two studies undertaken for this thesis address challenges with detection and characterization of hydrated minerals on Mars. I investigate clays and alunite-jarosite group minerals at Poás and Turrialba volcanoes, two new Mars analog sites in Costa Rica [Hynek *et al.*, 2014]. Ongoing acid sulfate alteration at Poás and Turrialba is analogous to processes that formed at least some of the mineral assemblages on Mars in the late Noachian and early Hesperian. Characterizing the mineral assemblages at these novel Mars analog sites enables interpretations for the formation of mineral assemblages discovered by Opportunity and Curiosity *in situ*. I also evaluate the capability of current or upcoming instruments for *in situ* mineralogy to detect clays and iron-rich natroalunite, a member of the alunite-jarosite family.

This thesis contributes to the growing body of geochemical and mineralogical studies of Mars analog sites, and has implications for the habitability of early Mars.

1.6 Thesis Structure

Chapter 1 introduced relevant background information on the history of the search for life, past or present, on Mars; the geologic history of Mars; the analysis of hydrated minerals to understand Mars' aqueous past; and the benefit of analog studies for improving our

understanding of Mars. This chapter also placed this thesis within the context of ongoing Mars analog research.

Chapters 2 and 3 are written in paper format for submission to peer-reviewed journals. Chapter 2 explores the ability of the Curiosity rover's x-ray diffraction (XRD) instrument, CheMin, to detect and characterize clays on Mars. XRD is a powerful tool for analysis of mineral assemblages, but the study of clay minerals benefits from additional sample preparation prior to XRD analyses. I evaluate the effect of removal of non-clay minerals, particle size separation, and preferred orientation on clay detection and identification with both a CheMin analog instrument and a traditional laboratory XRD to determine if CheMin may be missing clays present in samples at Gale Crater.

Chapter 3 investigates iron substitution in natroalunite in Costa Rica and evaluates methods for distinguishing between jarosite and iron-rich natroalunite on Mars. Following the recent discovery of iron-rich natroalunite in Nicaragua, I determine whether this mineral is a common product of acid sulfate alteration. I then assess whether XRD and Raman spectroscopy can be used to detect iron-rich natroalunite on Mars.

Chapter 4 concludes this thesis with a summary of the findings, followed by implications for assessing mineralogy on Mars, especially at Gale Crater. I also make recommendations for future avenues of research.

CHAPTER TWO:

DETECTION AND CHARACTERIZATION OF CLAYS ON MARS WITH XRD: INSIGHTS FROM CLAY-SPECIFIC XRD PREPARATION PROCEDURES ON SAMPLES FROM A HYDROTHERMAL ANALOG STUDY

2.1 Abstract

The Mars Science Laboratory (MSL) Curiosity rover is equipped with CheMin, the first x-ray diffraction (XRD) instrument on Mars, for quantitative *in situ* analysis of minerals. However, CheMin's inability to remove non-clay minerals and to preferentially orient samples, as is traditionally done on Earth, may pose significant challenges to the detection and characterization of clays on Mars. Clays require water to form and are well suited for organic matter preservation, and therefore the discovery and analysis of clays can provide crucial insight into the habitability of early Mars. To evaluate the effect of particle size separation (<0.2 μm), removal of non-clay minerals, preferred orientation, and ethylene glycol solvation on XRD analyses of clays, we used both a CheMin analog instrument and a traditional laboratory XRD instrument to determine the clays present in several samples of acid sulfate altered basalt from two volcanic analogs in Costa Rica. Of the 14 samples chosen for this project, four contained kaolinite and one also contained montmorillonite. Kaolinite was not detected in two of those samples with the analog instrument prior to the clay isolation procedure. These results suggest that CheMin may miss detection of some clays at Gale Crater, which could impact ensuing interpretations of Mars' early habitability.

2.2 Introduction

2.2.1 Clay Detections and Formation on Mars

Phyllosilicates are minerals built of repeating Si_2O_5 units and include micas, serpentine, and clay minerals such as smectites, kaolin group minerals, and chlorite. The discovery of these and other hydrated minerals with Observatoire pour la Mineralogie, l'Eau, les Glaces et l'Activité

(OMEGA) on Mars Express [Bibring *et al.*, 2005; Poulet *et al.*, 2005] and with Compact Reconnaissance Imaging Spectrometer for Mars (CRISM) on the Mars Reconnaissance Orbiter [Mustard *et al.*, 2008; Ehlmann *et al.*, 2010] was pivotal in the study of Mars' geochemistry and habitability. Orbital detections of phyllosilicates have primarily identified Fe,Mg smectites, ranging in composition from Fe-endmember nontronite to Mg-endmember saponite [Poulet *et al.*, 2005; Mustard *et al.*, 2008; Ehlmann *et al.*, 2011, 2013]. Chlorites are the second most abundant clay detected [Ehlmann *et al.*, 2013], followed by Al phyllosilicates, mainly of the kaolin family, and less often Al smectites such as montmorillonite [Poulet *et al.*, 2005; Ehlmann *et al.*, 2011, 2013].

The vast majority of clays are detected in Noachian terrains (>3.7 billion years old). The areally largest deposits are found in Meridiani Planum, Mawrth Vallis, Nili Fossae, and Aram Chaos [Poulet *et al.*, 2007; Ehlmann *et al.*, 2013]. Thousands of smaller deposits have been detected in the southern highlands, and some clay deposits have been identified in large craters in the northern lowlands [Mustard *et al.*, 2008; Ehlmann *et al.*, 2013]. These detections include deposits within several putative paleolakes and fluvial basins, such as Eberswalde, Jezero, and Holden craters [Mustard *et al.*, 2008; Ehlmann *et al.*, 2013]. Although no direct relationship between the clay deposits and these fluvial features has been discovered, the clays in these basins and across Mars' surface are clearly indicative of an aqueous past [Eberl *et al.*, 1984; Mustard *et al.*, 2008; Ehlmann *et al.*, 2011, 2013].

Various pathways of clay formation likely operated across early Mars, but several theories have been proposed to explain how and when the majority of clays formed. As is common on Earth, weathering through sustained contact with liquid water in a lacustrine or fluvial environment could have produced Mars' abundant clay deposits. Alternatively, clays could have formed concurrently with sulfates and iron oxides via hydrothermal acid sulfate alteration, as suspected for mineral assemblages at Noctis Labyrinthus [Weitz *et al.*, 2011; Thollet *et al.*, 2012], Columbus Crater [Wray *et al.*, 2011], and Cross Crater [Ehlmann *et al.*,

2016]. Another possibility that bypasses the challenge of explaining Mars' changing surface geochemistry is that clay formation occurred in the subsurface in low-grade hydrothermal (<400°C) systems [Ehlmann *et al.*, 2011].

To explain the different geochemical conditions needed to produce the range of minerals on Mars, as well as the general stratigraphy of sulfates overlying clays, Bibring *et al.* [2006] proposed that Mars' clay deposits formed in neutral pH prior to a global climate change, after which an acidic era of sulfate formation occurred. At a more local scale, the mechanism by which a particular clay deposit forms depends on a variety of factors, including thermodynamics (e.g. temperature and pressure); kinetics; and water chemistry (e.g. open or closed system, water-rock ratios, pH, ion activity, and oxidation state) [e.g., Ehlmann *et al.*, 2011, 2013]. Smectite formation is generally favored in closed systems with low water-rock ratios, whereas open systems with higher water-rock ratios tend to produce Al-rich clays such as kaolinite and montmorillonite [Eberl *et al.*, 1984; Ehlmann *et al.*, 2011].

The geochemical conditions that lead to different clay formation processes also affect habitability. *In situ* precipitation requires a long-lived water source, which could in turn produce a sustained habitable environment on the surface, while formation in subsurface, low-grade hydrothermal systems could support chemoautotrophic organisms [Cockell and Barlow, 2002; Ehlmann *et al.*, 2011]. Fine-grained sediments like clays also foster long-term organic matter preservation, as evidenced by the recent detections of hydrocarbons in mudstones by the Sample Analysis at Mars (SAM) instrument suite onboard Curiosity [Freissinet *et al.*, 2015, 2016].

2.2.2 Clay Characterization with XRD

X-ray diffraction (XRD) is a powerful tool for mineralogy that can distinguish between phyllosilicates based on minute differences in their interlayer spacing. The Mars Science Laboratory (MSL) Curiosity rover is equipped with CheMin, the first x-ray diffraction (XRD) instrument on Mars [Blake *et al.*, 2012]. XRD provides small scale mineralogy assessments by

using the diffraction of X-rays off atoms in a crystal structure to determine interlayer spacing, which is unique for every mineral. Other instruments on MSL complement mineral identification and analysis with CheMin; in particular the Alpha Particle X-ray (APXS) spectrometer, the SAM instrument suite, and ChemCam (a combined Remote Micro-Imager [RMI] and Laser-induced Breakdown Spectrometer [LIBS]).

CheMin uses a Co X-ray source in the range of $5-50^\circ 2\theta$ with a $<0.35^\circ 2\theta$ resolution and contains 27 reusable sample cells [Blake *et al.*, 2012]. As the sieve, funnel, and sample cells cannot be cleaned between samples, a predicted $\leq 5\%$ internal contamination between samples could result from material remaining in the funnel or in a previously used sample cell [Blake *et al.*, 2012]. CheMin analyzes particles $<150 \mu\text{m}$ and has a detection limit of 3 wt% [Blake *et al.*, 2012]. Unlike traditional powder diffraction XRD instruments which keep the sample stationary and rotate the x-ray source to investigate all crystal orientations, CheMin uses a stationary x-ray beam and samples are vibrated to produce random orientation [Blake *et al.*, 2012].

Curiosity landed in Gale Crater in August 2012 and investigated Yellowknife Bay before heading towards its primary mission target of Aeolis Mons, informally known as Mt. Sharp [Grotzinger *et al.*, 2014]. Vaniman *et al.* [2014] reported the detection of a smectite in two samples from the Sheepbed mudstone in Yellowknife Bay, which comprised ~ 22 wt% and ~ 18 wt% of the John Klein (JK) and Cumberland (CB) samples, respectively. Based on modeling and comparison with samples analyzed with a CheMin testbed instrument, the smectite in both samples was inferred to be a ferrian saponite derived from aqueous alteration of olivine [Vaniman *et al.*, 2014; Bristow *et al.*, 2015]. Differences in d-spacing between clays in JK and CB was attributed to different swelling behaviors [Vaniman *et al.*, 2014; Bristow *et al.*, 2015]. En route to Mt. Sharp, CheMin analyzed the Windjana (WJ) sample from the Kimberley formation, which contained kaolinite near the detection limit and ~ 10 wt% phyllosilicate inferred to be mostly a collapsed smectite based on comparison to JK and CB [Treiman *et al.*, 2016].

Now at the base of Mt. Sharp, Curiosity has analyzed four samples from the Murray Formation. The Confidence Hills (CH) and Mojave 2 (MJ) samples from Pahrump Hills, the basal member of the Murray Formation, both contain clays [Cavanagh *et al.*, 2015; Rampe *et al.*, 2015, 2016]. The phyllosilicate in CH is believed to be a collapsed smectite or poorly ordered mineral such as illite and comprises ~11 wt% of the sample, while preliminary analyses indicate less clay is present in MJ [Cavanagh *et al.*, 2015; Rampe *et al.*, 2015, 2016]. Farther up section in the Murray Formation, phyllosilicates were not detected in either Telegraph Peak (TP, ~6 meters up from MJ) or Buckskin (BK, ~6 meters up from TP) [Rampe *et al.*, 2015, 2016; Morris *et al.*, 2016].

The detection of clays in JK, CB, WJ, CH, and MJ does not guarantee that all phyllosilicates present in these samples were detected, and the absence of clay detections in TP and BK is not proof of absence. In addition, clay characterization at Gale depends on modeling different swelling behaviors and comparison between the samples. On Earth, XRD analyses take into account that clays generally have similar X and Y dimensions, so orientation to increase the basal (00 l) reflection is preferred over random orientation [Moore and Reynolds, 1997]. In addition, non-clay minerals often produce peaks that interfere with clay peaks, so isolation of clays from other minerals in a sample improves clay detection and identification.

To determine if CheMin's inability to remove non-clay minerals and to preferentially orient samples significantly impairs clay analysis at Gale Crater, we evaluated the effects of a clay mineral isolation procedure and preferred orientation on XRD analyses for a suite of samples from acid sulfate altered basalt from volcanic Mars analog sites in Costa Rica [Hynek *et al.*, 2014]. We compared results before and after particle size separation (<0.2 μm), removal of non-clay minerals, and preferred orientation using a CheMin analog instrument and a traditional laboratory XRD instrument to determine the extent to which these steps would aid clay mineral detection at Gale Crater.

2.3 Field Site Description and Sample Collection

Fieldwork was conducted in November 2013 at Poás and Turrialba volcanoes in Costa Rica (Figure 2.1). The subduction of the Cocos Plate beneath the Caribbean Plate forms the

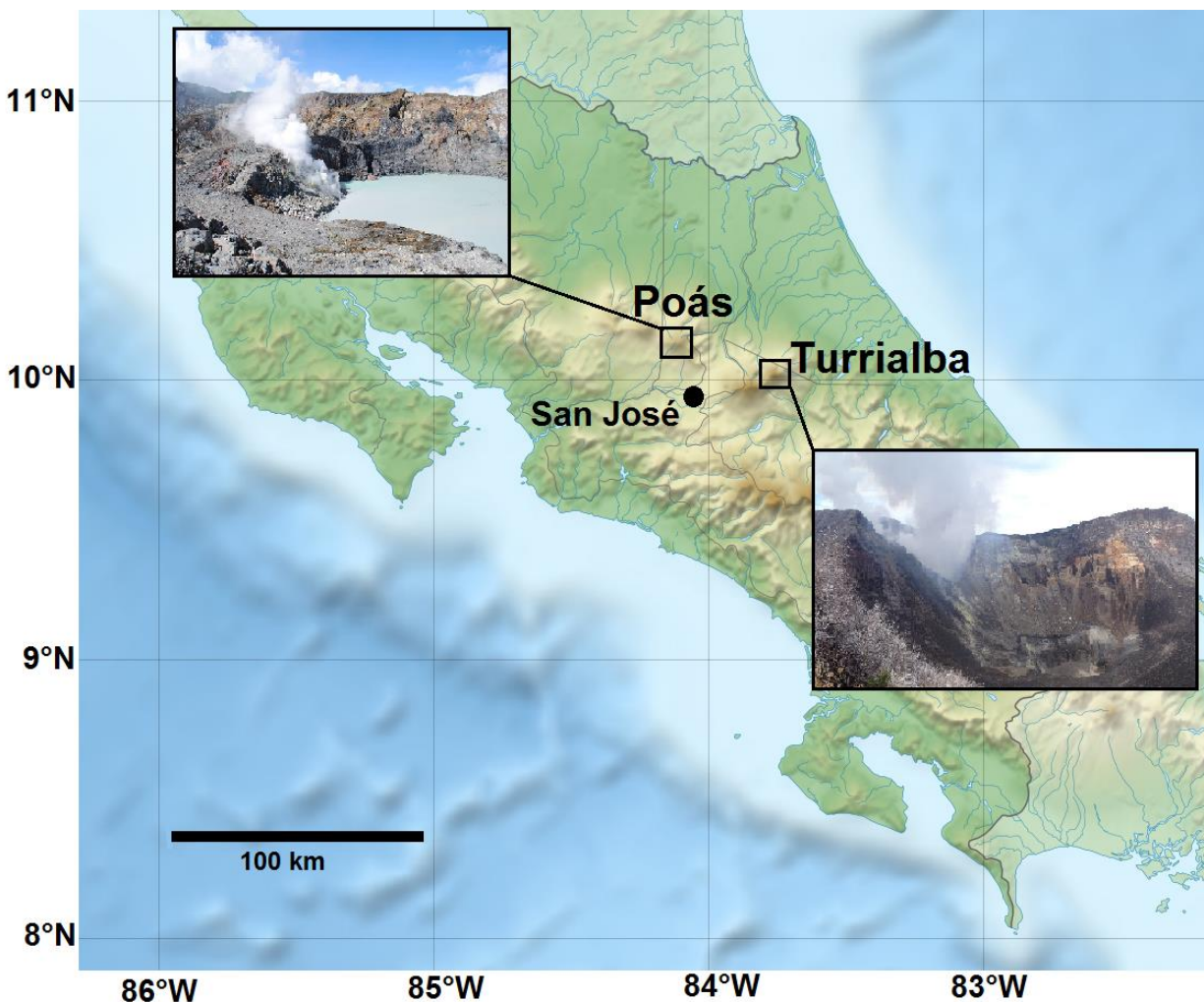


Figure 2.1: Fieldwork was conducted at Poás Volcano and Turrialba Volcano [photos inset]. The two volcanoes are part of the Central American Volcanic Chain formed by the subduction of the Cocos Plate under the Caribbean Plate. Adapted from elevation map by Eric Gaba.

Central American volcanic chain, which stretches 1100 km from Costa Rica through Guatemala [Prosser and Carr, 1987; Cigolini et al., 1991]. Lava composition in central Costa Rica is generally consistent with an ocean island basalt (OIB) with minimal contribution from the subducting slab, although He isotopic analysis suggests Turrialba has both mid-ocean ridge

basalt (MORB) and OIB components [Herrstrom et al., 1995; Di Piazza et al., 2015]. Poás and Turrialba are members of Cordillera Central, a large massif of overlapping pyroclastic deposits in central Costa Rica [Prosser and Carr, 1987].

Poás has an estimated age of 1 million years and has been continuously mildly active throughout its recorded history, with ongoing fumarole activity and frequent phreatic eruptions through the crater lake ranging from small gas emissions to major pyroclastic eruptions reaching >400 m high in recent years [Prosser and Carr, 1987; de Moor et al., 2016]. Magma composition follows a cyclical sequence of felsic to mafic, with recent eruptions indicating that the volcano is currently in the mafic stage [Prosser and Carr, 1987].

The current volcanic activity at Turrialba also began ~1 million years ago [Reagan et al., 2006]. Turrialba has three interior craters referred to as the center, east, and west craters and an andesitic to basaltic lava composition [Reagan et al., 2006; Di Piazza et al., 2015].

Turrialba's most recent major eruptive period occurred between 1864 and 1866 and resulted in lahars, pyroclastic deposits, and ash deposits [Reagan et al., 2006]. Before fieldwork, phreatic eruptions occurred in January 2010 and January 2012, which formed new openings near the west crater, and further eruptions occurred near the west crater in May 2013 [van Manen, 2014; Di Piazza et al., 2015].

Samples were collected from several sites at each volcano chosen to represent a range of environmental conditions (Figures 2.2 and 2.3). Sites ranged from outwash basins near crater lakes to active fumaroles, and temperatures and pH at time of sampling ranged from ~16°C to 180°C and <1 to 5, respectively. Samples had varied colors including white, yellow, red, and purple, and were predominantly loose sediments or hand samples.

Samples selected for this study came from three of four sampling sites at Poás (Figure 2.2) and three at Turrialba (Figure 2.3). "Poás Dome Edge" samples are from the edge of a mound on the crater lake's southern rim, which had an ambient temperature and was too dry for



Figure 2.2: Poás volcano, Costa Rica. Samples used in this study were collected from the dome edge (a, Poás Dome Edge), a few meters to the west at the edge of active fumaroles (b, Poás Fumaroles), and on an outwash basin occasionally inundated with lake water and hot pyroclastic material (c, Poás Fluv).

pH measurements at the time of sampling (Figure 2.2a). “Poás Fumarole” samples were collected a few meters west of Poás Dome Edge and immediately adjacent to active fumaroles, and were $\sim 90^{\circ}\text{C}$ and $\text{pH} < 1$ (Figure 2.2b). “Poás Fluv” samples were collected on an outwash basin containing welded pyroclastic deposits and sometimes inundated with lake water. The Poás Fluv site had an ambient temperature and was too dry for pH measurements during sampling, although the crater lake itself was 45°C with $\text{pH} 0.3$ at the time of fieldwork (Figure 2.2c). “Turrialba” and “Turritop” samples came from two parallel fumarolic gullies, each roughly a meter deep, on the western crater’s outer slope and had a temperature $\sim 100^{\circ}\text{C}$ and $\text{pH} \sim 1.5\text{-}2$ at time of sampling (Figure 2.3a). “TuN” samples are from an active fumarolic region north of the center crater with temperature $\sim 60\text{-}100^{\circ}\text{C}$ and $\text{pH} 3\text{-}5$ (Figure 2.3b). “Tu Center Crater” samples

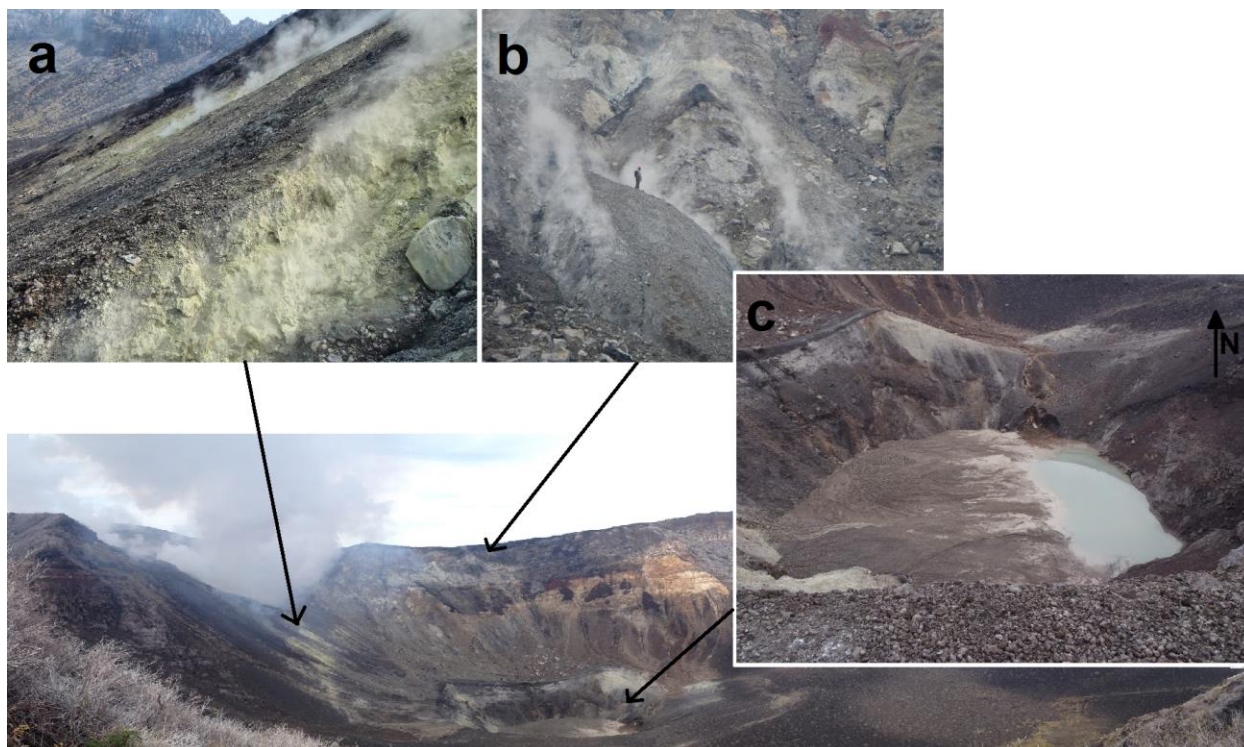


Figure 2.3: Turrialba volcano, Costa Rica. Samples used in this study were collected from roughly meter deep parallel fumarolic gullies on western crater outer slope (a, Turrialba or Turritop), active fumaroles north of the center crater (b, Tu N), and from the center crater lake's northeast edge (c, Tu Center Crater). Note the person for scale in (b).

were collected from the northeast edge of the center crater above the lake shoreline (Figure 2.3c). The lake itself was 15.7°C and pH 3.3 at time of sampling.

The hydrothermal acid sulfate alteration environments at Poás and Turrialba are analogous to those proposed for several sites on Mars, such as Gusev Crater [Squyres *et al.*, 2008; Yen *et al.*, 2008], Noctis Labyrinthus [Weitz *et al.*, 2011; Thollot *et al.*, 2012], and most recently Gale Crater [Rampe *et al.*, 2015, 2016]. Sulfate-rich soils and silica deposits at Gusev Crater have been interpreted as consistent with a fumarolic formation [Squyres *et al.*, 2008; Yen *et al.*, 2008]. Hydrothermal acid sulfate alteration also likely formed a varied mineralogical assemblage, including kaolinite, Fe smectites, and Fe(III) sulfates, at Noctis Labyrinthus in the late Hesperian [Weitz *et al.*, 2011; Thollot *et al.*, 2012]. Preliminary analyses of mudstones containing phyllosilicates, iron oxides, jarosite, and amorphous and crystalline silica at Pahrump

Hills in Gale Crater have been attributed to leaching by acid-sulfate fluids [Rampe *et al.*, 2015, 2016].

2.4 Sample Selection

Of 57 samples collected at Poás and Turrialba and analyzed with XRD, 14 were selected for further clay mineral analyses based on the following criteria (Table 2.1; Figure 2.4):

1. A strong rise in intensity in the low ($<10^\circ$) 2θ region in XRD patterns.
2. Small, broad peaks in the $<15^\circ$ 2θ region, some of which were already identified or tentatively identified as clays with one or both XRD instruments prior to these analyses.
3. Visual and tactile examination in both the field and the laboratory that suggested the presence of clay-sized particles, and/or sample collection from Poás Fluv or Tu Center Crater sites.
4. Clays identified with VNIR in this sample set [Black *et al.*, 2015, 2016] but not suspected based on any above criteria.

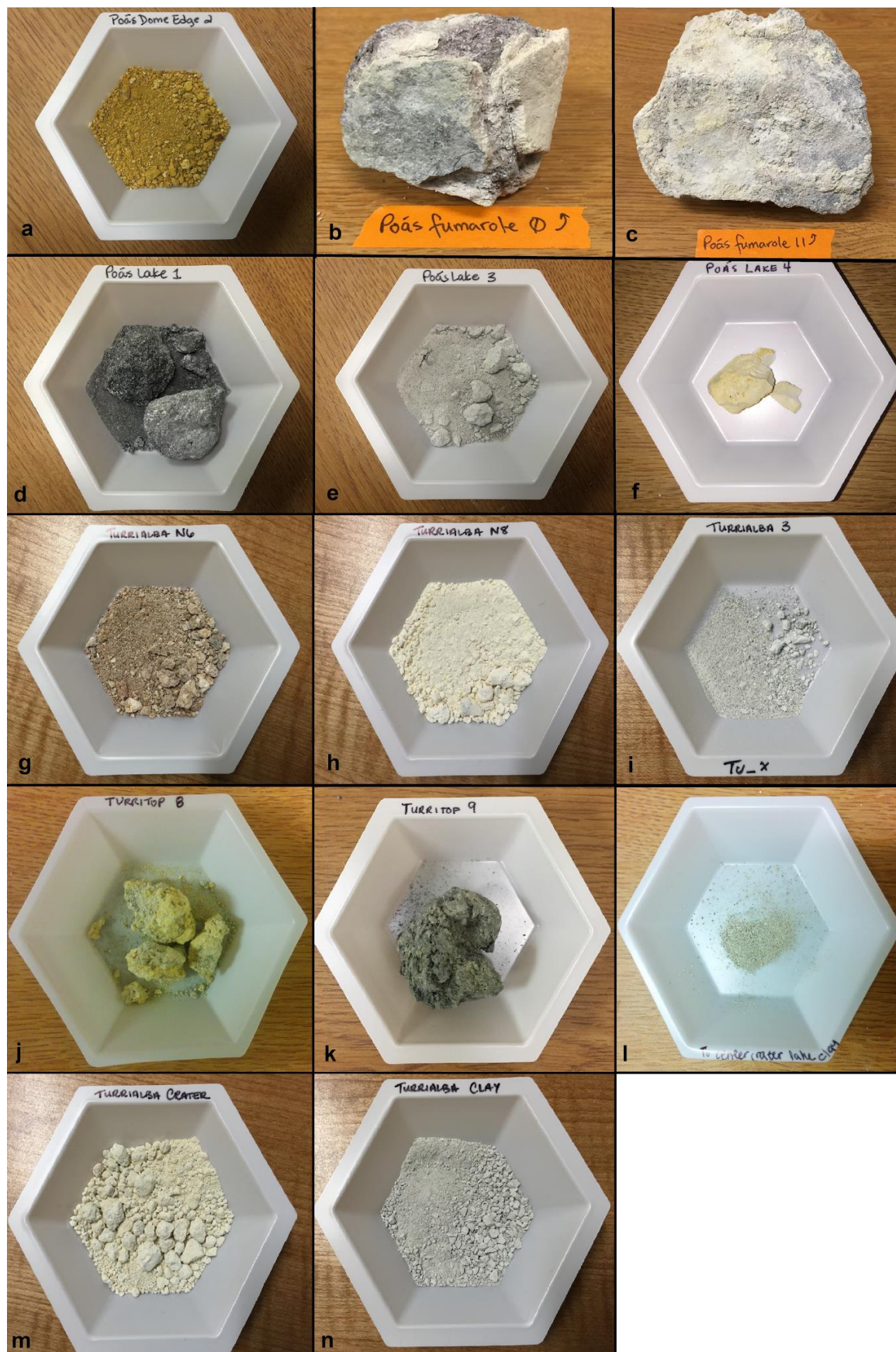
Additional minerals commonly present in these samples based on XRD analyses conducted prior to this study (Table 1) included amorphous silica, cristobalite, natroalunite, anhydrite, and unaltered labradorite. A few samples also had anatase (titanium oxide), gypsum, sulfur, and tridymite, and two to three contained iron oxides (hematite, goethite, and a tentative magnetite detection). Alunogen, pargasite, and jarosite were detected in one sample each.

Prior to the study, kaolinite was already identified in two samples (Tu N6 and Poás Fluv Clay 2) and montmorillonite was also detected in Poás Fluv Clay 2. Nontronite was tentatively identified with the analog XRD instrument in Tu N8 and Poás Fumarole 0 based on broad peaks centered at $\sim 9^\circ$ 2θ , and chlorite was tentatively identified in Tu Center Crater 1 with the laboratory XRD instrument.

Sample	Criteria matched	Minerals identified with Terra before study	Minerals identified with Bruker D2 Phaser before study
Poás Dome Edge 2	1	Natroalunite, cristobalite, and labradorite	Natroalunite and cristobalite
Poás Fumarole 0	1 and 2 (tentative nontronite)	Amorphous silica, labradorite, cristobalite, tridymite, hematite, <i>anhydrite</i> , <i>nontronite</i> , <i>natroalunite</i>	Gypsum, cristobalite, natroalunite, labradorite, amorphous silica
Poás Fumarole 11	1	Natroalunite, cristobalite, anatase, amorphous silica	Cristobalite, tridymite, natroalunite, anatase, labradorite, amorphous silica
Poás Fluv "Rock"	1 and 3	Amorphous silica, labradorite	Amorphous silica, labradorite, cristobalite, anhydrite, <i>natroalunite</i> , <i>magnetite</i> , <i>tridymite</i>
Poás Fluv Clay 1	1 and 3	Natroalunite, cristobalite, labradorite, amorphous silica	Natroalunite, cristobalite, sulfur, labradorite, amorphous silica
Poás Fluv Clay 2	1, 2, and 3 (kaolinite and montmorillonite)	Natroalunite, cristobalite, kaolinite , montmorillonite , alunogen	Natroalunite, cristobalite, kaolinite , alunogen, magnetite, montmorillonite
Tu N6	1 and 2 (kaolinite)	Natroalunite, cristobalite, hematite, goethite, kaolinite , amorphous silica	Natroalunite, cristobalite, goethite, hematite, kaolinite , amorphous silica
Tu N8	1 and 2 (tentative nontronite)	Anatase, amorphous silica, <i>natroalunite</i> , nontronite	Anatase, amorphous silica, natroalunite
Turrialba 3	4 (control)	Natroalunite, gypsum, cristobalite, amorphous silica, <i>anhydrite</i>	Natroalunite, gypsum, anhydrite, cristobalite
Turritop 8	1	Natroalunite, jarosite, cristobalite, amorphous silica	Natroalunite, jarosite, natrojarosite, cristobalite, amorphous silica
Turritop 9	4 (control)	Sulfur, anhydrite, anatase, amorphous silica	Sulfur, anhydrite, anatase, amorphous silica
Tu Center Crater 1	2 and 3 (tentative chlorite)	Natroalunite, cristobalite, labradorite, anhydrite, amorphous silica	Natroalunite, cristobalite, labradorite, anhydrite, amorphous silica, chlorite
Tu Center Crater 2	3	Natroalunite, amorphous silica, <i>tridymite</i> , <i>cristobalite</i>	Natroalunite, amorphous silica, <i>cristobalite</i>
Tu Center Crater 3	2 and 3 (kaolinite)	Natroalunite, cristobalite, amorphous silica, sulfur, <i>tridymite</i>	Natroalunite, cristobalite, kaolinite , labradorite, sulfur, pargasite, amorphous silica

Table 2.1: Fourteen samples selected for study, the criteria on which they were selected (see text for description of criteria), and the other minerals identified with Terra and Bruker D2 Phaser XRD instruments prior to study. Clays detected or suspected are bolded. Tentative mineral detections are italicized.

Figure 2.4 (next page): The 14 samples used in this study: (a) Poás Dome Edge 2, (b) Poás Fumarole 0, (c) Poás Fumarole 11, (d) Poás Fluv Rock, (e) Poás Fluv Clay 1, (f) Poás Fluv Clay 2, (g) Tu N6, (h) Tu N8, (i) Turrialba 3, (j) Turritop 8, (k) Turritop 9, (l) Tu Center Crater 1, (m) Tu Center Crater 2, (n) Tu Center Crater 3. Criteria for sample collection and mineralogy determined prior to study in Table 2.1. All images ~7 cm wide, except for b (~9 cm wide) and c (~12 cm wide).



2.5 Methods

To test the detection or non-detection of clays with CheMin, the following clay-isolation procedure was developed, based on *Moore and Reynolds* [1997] and the protocol of Dr. Lindsay McHenry [personal communication]. Two grams (+/- 0.05 grams) of sample were gently grinded with mortar and pestle while submerged in dl water to increase surface area of grains without crushing non-clay minerals into clay particle sizes [*Moore and Reynolds*, 1997]. Samples were submersed in water for ≥ 24 hours, then dried. One gram of Turrialba 3 and Tu Center Crater 1 was used due to limited sample quantity.

1. *Sulfate Removal.* Following the procedures of *Bodine and Fernald* [1973] for selective extraction of gypsum and anhydrite from samples, a 0.25 M solution of ethylenediaminetetraacetic acid (EDTA) was used with its pH adjusted to 11 by addition of sodium hydroxide pellets. A new 0.25 M EDTA solution was made for each batch of 2-4 samples to ensure its efficacy. Two grams of dried sample and 60 mL of 0.25 M EDTA solution were added to glass beakers, which were then boiled at $\sim 275^{\circ}\text{C}$ for 4 hours. Lids were loosely placed on the beakers to minimize solution vapor loss, although some loss did occur (≤ 30 mL per sample). 30 mL of 0.25 M EDTA solution was used for the two 1 gram samples. After cooling samples, we attempted to separate soluble and insoluble fractions into two 50 mL falcon tubes. The insoluble fractions were repeatedly rinsed by centrifugation at 2000 rpm for 3 minutes until color and pH (< 7.5) indicated complete removal of solution. However, as clays and sulfates were present in both soluble and insoluble fractions, both fractions underwent all subsequent steps. Both soluble and insoluble fractions of each sample were dried for analyses with both XRD instruments.

2. *Dispersion.* Samples were further rinsed until supernatant appeared cloudy, indicating clay dispersal, and was decanted. 3.5-4 mg of sodium pyrophosphate was added to supernatant to aid dispersion. An additional 2-3 mg of sodium carbonate was added, as *Moore and*

Reynolds [1997] noted that this is effective with samples rich in amorphous silica. Samples were allowed to rest for several minutes after the addition of each dispersal agent.

3. *Flocculation*. Samples were centrifuged at 750 rpm for 3.3 minutes, then the supernatant was quickly decanted. Clays were flocculated overnight in a 0.1 M calcium chloride solution. Samples were centrifuged at 2000 rpm for 3 minutes the following morning to further concentrate flocculated clays, which were then plated on P-type, B-doped zero diffraction silicon wafers (MTI Corporation, Richmond, CA) and allowed to air dry overnight. Samples were analyzed with the bench-top XRD instrument. When ≥ 15 mg of sample remained following flocculation and plating, additional sample was air dried for the analog XRD instrument analysis.

4. *Ethylene glycol solvation*. Several plated air-dried samples were exposed to ethylene glycol vapors in a room temperature dessicator for ≥ 24 hours, then re-analyzed with the bench-top XRD instrument within one hour of removal from desiccator to prevent collapse of expanded smectite layers.

5. *XRD Analysis*. Sample analysis was performed before and after the clay isolation procedure with both Bruker D2 Phaser and Terra XRD instruments. The Bruker D2 Phaser was operated at 30 kV and 10 mA using $\text{CuK}\alpha$ radiation ($\lambda = 1.5418\text{\AA}$) in the range $3\text{-}55^\circ 2\theta$ with a Lynxeye 1D detector with a 0.02° step size and 0.5 s per step collection time. The divergence slit was set to 0.6 mm and the antiscatter shield placed 1 mm above the plated sample. Samples dried after sulfate removal and/or after flocculation were also run with a portable Terra X-ray diffraction/X-ray fluorescence (XRD/XRF) instrument (formerly inXitu Incorporated, now marketed by Olympus Corporation, Tokyo, Japan; Figure 2.5). The Terra instrument was designed as a commercial CheMin instrument testbed [Blake et al., 2012]. It weighs ~ 20 kg and is built into a carrying case with a handle, making it field portable. Analyses were conducted at 30 kV using $\text{CuK}\alpha$ radiation in the range $5\text{-}55^\circ 2\theta$. The Terra instrument has a resolution of $\sim 0.05^\circ 2\theta$ and an intended 1 wt% detection limit [Treiman et al., 2010].



Figure 2.5: The Terra X-ray diffraction/X-ray fluorescence (XRD/ XRF) instrument in use near the Turritop site (near top of photo) and the center crater (out of frame to right).

2.6 Results

2.6.1 Clay Detections

Of the 14 samples that fit one or more of the above criteria (rise in intensity $<10^\circ 2\theta$, small broad peaks $<15^\circ 2\theta$, *in situ* physical observations, and/or identification with VNIR), clay detections or tentative detections were confirmed in four samples following the clay isolation procedure (Table 2.2; Figures 2.6, 2.7, 2.8, and 2.9). Kaolinite was identified in all four, and one Poás Fluv sample also contained montmorillonite (Poás Fluv Clay 2, Figure 2.6). The other clay

detections were in Turrialba samples from Tu N (Tu N6, Figure 2.7) and Tu Center Crater (Tu Center Crater 1, Figure 2.8; Tu Center Crater 3, Figures 2.9) sites.

Clays were only detected in samples with definitive or tentative detections prior to the clay isolation procedure. Kaolinite was detected in Tu N6 and Poás Fluv Clay 2 with both XRD instruments prior to the procedure. Clays were tentatively identified prior with the Bruker D2 Phaser but not with the Terra in Tu Center Crater 1 and Tu Center Crater 3. Two samples with a tentative nontronite detection (Tu N8 and Poás Fumarole 0) with the Terra XRD instrument prior did not contain any sign of clays in diffraction patterns from either instrument after the procedure.

2.6.2 Efficacy of Non-Clay Mineral Removal

The clay isolation procedure only removed all non-clay minerals in one sample (Poás Fluv Clay 2, Table 2.2, Figure 2.6). Sulfur was removed from all applicable samples, and amorphous silica, cristobalite, and labradorite were removed from most. Cristobalite and amorphous silica are often present in the clay-sized fraction, making these minerals more difficult to remove [Moore and Reynolds, 1997]. As chemical removal of iron and titanium oxides was not attempted, hematite, goethite, and anatase were not removed. Although fluorescent x-rays from iron can produce a background that may mask clay peaks, chemical iron oxide removal can alter the XRD response of mixed-layer clay minerals and was considered unnecessary for anatase- and iron oxide-containing samples considering the risk [Moore and Reynolds, 1997].

Calcium sulfate removal was mostly successful: gypsum was removed from all samples, and anhydrite was removed from most. In contrast to our findings, anhydrite is expected to be more easily removed than gypsum due to its higher solubility [Bodine and Fernald, 1973].

Table 2.2 (next page): Minerals identified in samples before and after clay isolation procedure. Samples with confirmed clays are listed first. Tentative mineral detections are italicized. *=halite likely produced during dispersion. †=mineral that may be endogenous but not detected prior to the study, or due to contamination.

Sample	Criteria Matched	Minerals identified before and after study (both instruments)	Minerals remaining after study (Bruker)	Confirmed clays
Poás Fluv Clay 2	1	Natroalunite, cristobalite, kaolinite, alunogen, and montmorillonite	-	Kaolinite and montmorillonite
Tu N6	1,2	Natroalunite, cristobalite, hematite, goethite, kaolinite, amorphous silica	Natroalunite, hematite, goethite, amorphous silica	Kaolinite
Tu Center Crater 1	2,3	Natroalunite, cristobalite, labradorite, anhydrite, amorphous silica, <i>chlorite</i>	Natroalunite, cristobalite, anhydrite	Kaolinite
Tu Center Crater 3	2,3	Natroalunite, cristobalite, amorphous silica, kaolinite, sulfur, labradorite, pargasite, <i>tridymite</i>	Natroalunite, halite*	Kaolinite
Poás Dome Edge 2	1	Natroalunite, cristobalite, <i>labradorite</i>	Natroalunite, cristobalite	-
Poás Fumarole 0	1,3	Amorphous silica, natroalunite, labradorite, cristobalite, tridymite, gypsum, hematite, <i>anhydrite, nontronite</i>	Cristobalite, amorphous silica, natroalunite, labradorite, anhydrite, tridymite, <i>hematite</i>	-
Poás Fumarole 11	1,3	Natroalunite, cristobalite, anatase, tridymite, labradorite, amorphous silica	Cristobalite, amorphous silica, natroalunite, anatase, tridymite	-
Poás Fluv "Rock"	1,2,3	Amorphous silica, labradorite, cristobalite, anhydrite, <i>natroalunite, magnetite, tridymite</i>	Amorphous silica, anhydrite, cristobalite, natroalunite	-
Poás Fluv Clay 1	1	Natroalunite, cristobalite, sulfur, labradorite, amorphous silica	Natroalunite, halite*	-
Tu N8	1,2	Anatase, amorphous silica, natroalunite, <i>nontronite</i>	Anatase, amorphous silica, natroalunite, hornblende [†]	-
Turrialba 3	4	Natroalunite, gypsum, cristobalite, anhydrite, <i>amorphous silica</i>	Natroalunite	-
Turritop 8	1	Natroalunite, jarosite, natrojarosite, cristobalite, amorphous silica	Natroalunite, hornblende [†] , halite*, <i>jarosite</i>	-
Turritop 9	4	Sulfur, anhydrite, anatase, amorphous silica	Anatase, labradorite [†] , halite*	-
Tu Center Crater 2	3	Natroalunite, amorphous silica, <i>tridymite, cristobalite</i>	Natroalunite	-

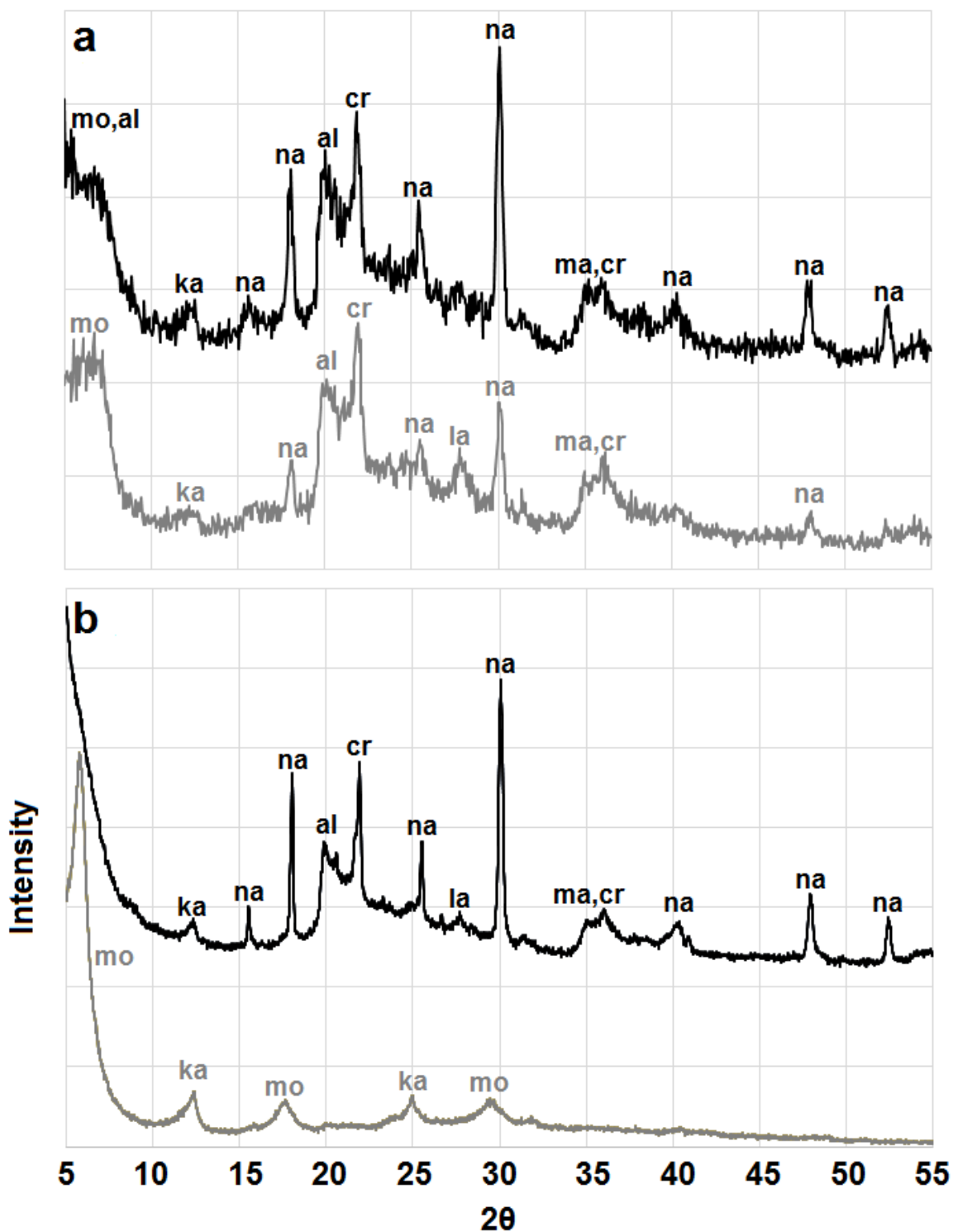


Figure 2.6: Poás Fluv Clay 2 (a) Terra XRD and (b) Bruker D2 Phaser XRD diffraction patterns before (black) and after (gray) clay isolation procedure. Labels: mo=montmorillonite, al=alunogen, ka=kaolinite, na=natroalunite, cr=cristobalite, ma=magnetite. Patterns offset for clarity.

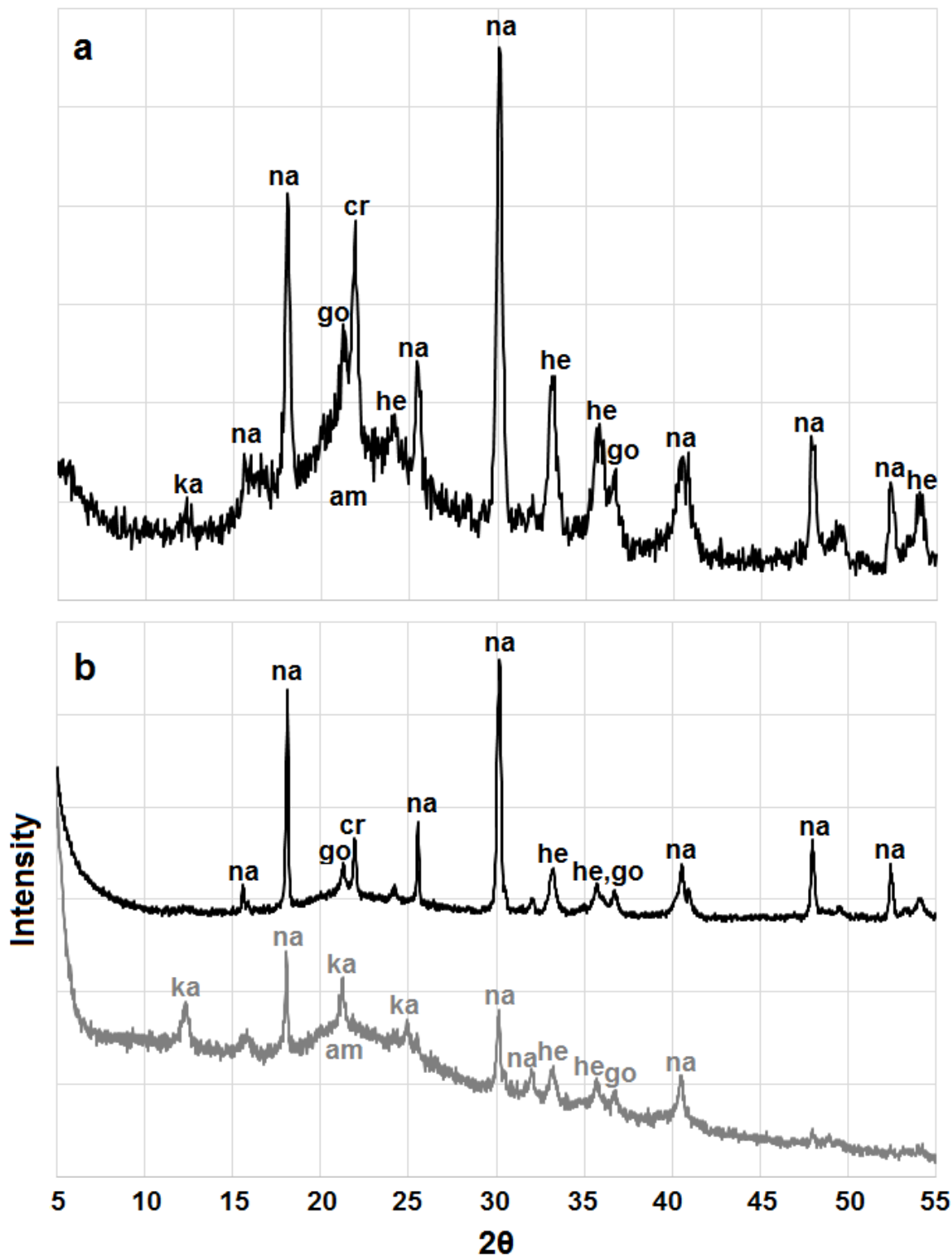


Figure 2.7: Tu N6 (a) Terra XRD and (b) Bruker D2 Phaser XRD diffraction patterns before (black) and after (gray) clay isolation procedure. Insufficient sample (<15 mg) remained after sulfate removal for Terra XRD analysis. Labels: ka=kaolinite, na=natroalunite, go=goethite, cr=cristobalite, he=hematite, am=amorphous silica. Patterns offset for clarity.

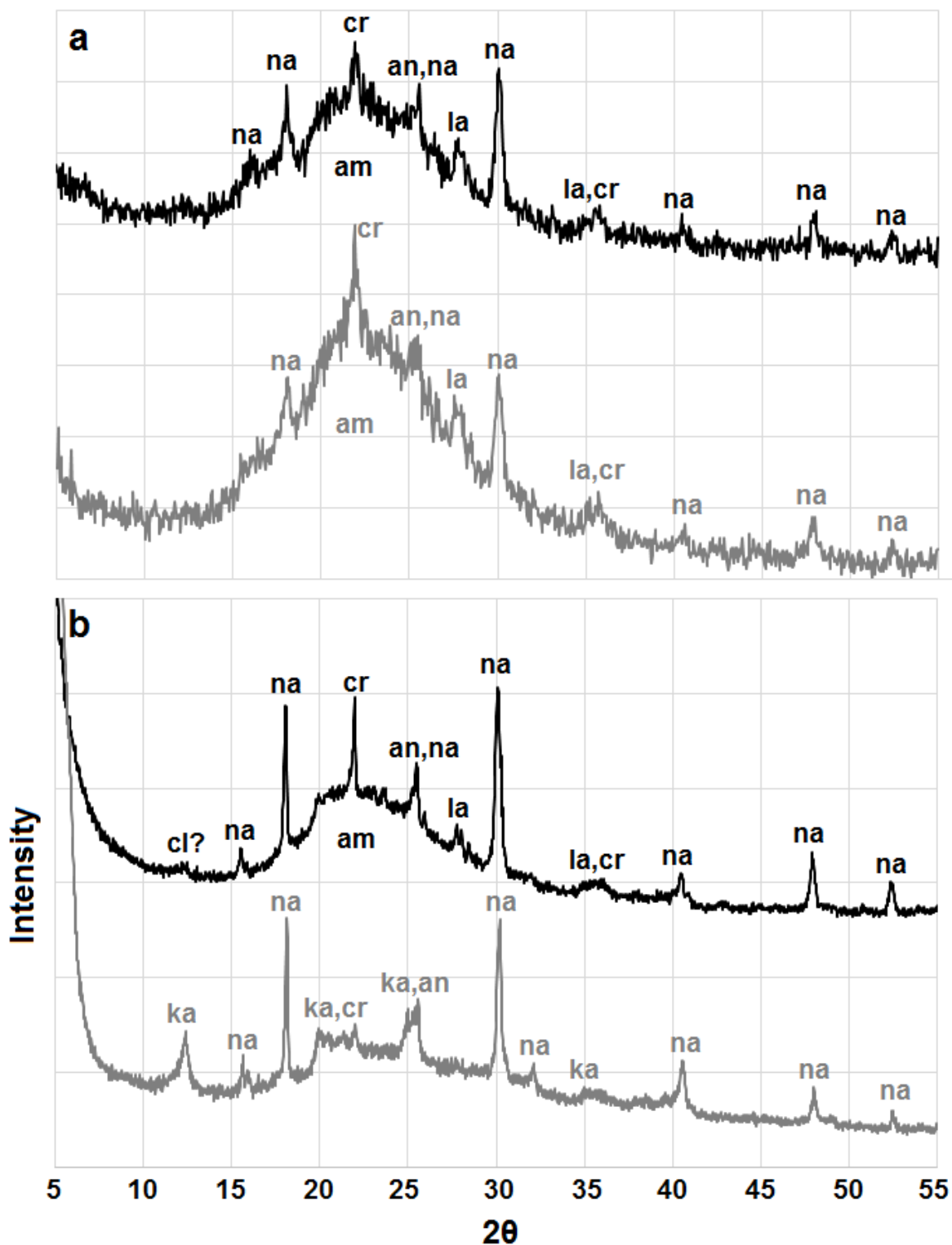


Figure 2.8: Tu Center Crater 1 (a) Terra XRD and (b) Bruker D2 Phaser XRD diffraction patterns before (black) and after (gray) clay isolation procedure. Labels: ka=kaolinite, na=natroalunite, cr=cristobalite, an=anhydrite, la=labradorite, am=amorphous silica, cl?=tentative clay detection. Patterns offset for clarity.

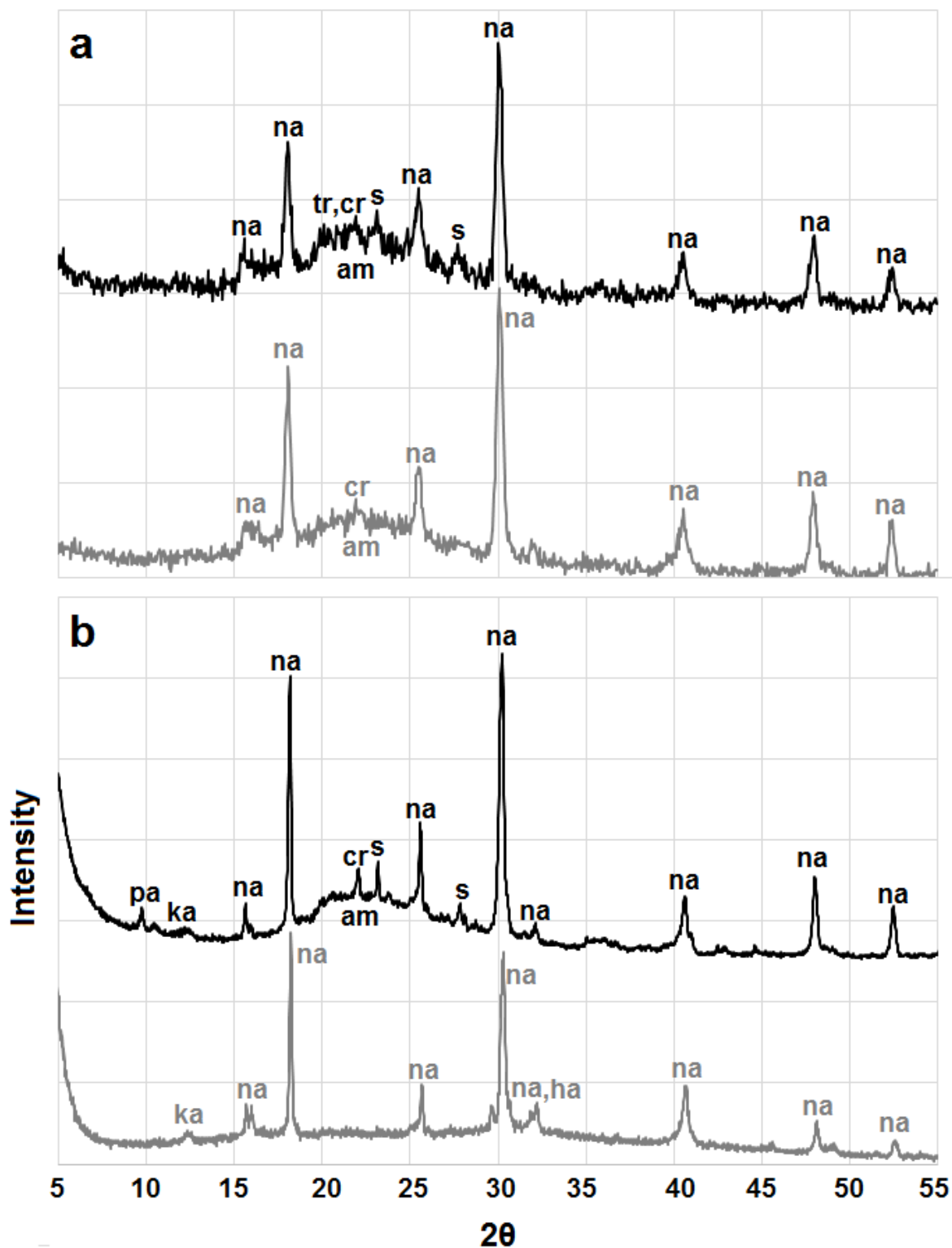


Figure 2.9: Tu Center Crater 3 (a) Terra XRD and (b) Bruker D2 Phaser XRD diffraction patterns before (black) and after (gray) clay isolation procedure. Note presence of halite after dispersion. Labels: ka=kaolinite, na=natroalunite, tr=tridymite, cr=cristobalite, s=sulfur, am=amorphous silica, pa=pargasite, ha=halite. Patterns offset for clarity.

Other sulfates—natroalunite, jarosite, and alunogen—were not removed. To date, no other study has attempted to remove sulfates other than gypsum and anhydrite for clay XRD analyses, or to remove sulfates from acid sulfate altered basalt. As the concentration and quantity of EDTA solution per sample were that needed for calcium sulfate removal from evaporites, 60 mL of 0.25 EDTA solution may have been insufficient for all sulfate cations to form a complex with EDTA. Differences in cations (Al^{3+} in alunogen, K^+ , Na^+ , Al^{3+} , and Fe^{3+} in alunite-jarosite group minerals, as compared to Ca^{2+} in gypsum and anhydrite) may have also played a role. Work outside this study has showed that natroalunite in some of these samples has minor Ca^{2+} substitution for Na^+ (natroalunite-2c, also known as minamiite); if cation differences mattered, some or all of the natroalunite-2c would be expected to have complexed with EDTA.

Removing Fe^{3+} from jarosite or Fe-rich natroalunite may also require procedures more similar to those used for iron oxide removal than for sulfate extraction. Sulfate removal could have been further complicated by solution loss during boiling, and by the large amount of sulfates, particularly natroalunite, in samples (estimated >50% sulfate for most samples). Changes to the *Bodine and Fernald* [1973] sulfate removal procedure are clearly necessary to remove these sulfates from acid sulfate altered basalts.

The incomplete removal of non-clay minerals also could have been due in part to human error. Grinding of samples may not have been adequately gentle and thus reduced non-clay minerals to the clay size (<2 μm) fraction. Another possibility is that decanting of the clay-containing supernatant after dispersion was performed too soon and larger, non-clay particles did not have adequate time to settle.

Although removal of non-clay minerals was incomplete, the relative intensity of clay peaks to other mineral peaks increased, which aided in clay detection and characterization. Tentative clay detections in Tu N6 and Tu Center Crater 1 were confirmed and characterized due to changes in relative peak intensities (Figures 2.7 and 2.8). Natroalunite peak intensities

were reduced in some cases (e.g. Figure 2.7b) and unremoved cristobalite peaks were reduced in most cases (e.g. Figure 2.9b).

2.6.3 Complications from Dispersion

Several air-dried samples showed reaction with dispersal agents or potential contamination. Diffraction patterns of four samples air-dried after flocculation (Poás Fluv Clay 1, Turritop 8, Turritop 9, and Tu Center Crater 3) contained halite (e.g. Figure 2.9). Halite was likely produced by the addition of sodium pyrophosphate and sodium carbonate during dispersion, although contamination in the laboratory is also possible. Two samples (Tu N8 and Turritop 8) also contained hornblende following the clay isolation procedure, which may have been present but undetected in the initial samples due to sample heterogeneity or could be a result of laboratory contamination.

2.6.4 Analysis with the Terra XRD Instrument

Samples could only be run on the Terra XRD instrument following sulfate removal, as insufficient material (<15 mg) remained after flocculation for most samples. Samples for which adequate material remained were difficult to analyze with the Terra instrument because flocculation concentrates clays for preferred orientation; consequently this material could not be easily vibrated for random orientation. Sulfates were incompletely removed from most samples; therefore, limited differences were noted between Terra diffraction patterns before and after sulfate removal for Poás Fluv Clay 2, Tu Center Crater 1, and Tu Center Crater 3. Due to limited sample following sulfate removal, Tu N6 could not be rerun on the Terra instrument to evaluate the effect of this step on the relative intensity of clay and non-clay peaks.

2.6.5 Ethylene Glycol Solvation

Ethylene glycol solvation is used in smectite identification because it expands smectite d-spacing, resulting in peak shifts towards lower 2θ values. Other phyllosilicates cannot accommodate ethylene glycol between layers, therefore ethylene glycol solvation was unnecessary for all samples except Poás Fluv Clay 2, in which montmorillonite was identified

prior to this study. Bruker D2 Phaser diffraction patterns (Figures 2.6, 2.7, 2.8, and 2.9) are accordingly for samples air-dried after flocculation.

Diffraction patterns of several samples that underwent ethylene glycol solvation displayed more amorphous characteristics than before, in particular those selected under criteria 4 (Turrialba 3 and Turritop 9). A broad hump centered at 2θ values of $\sim 12^\circ$ or 13° appeared, in addition to an increase in the extent of the hump centered at $\sim 30^\circ$ 2θ often associated with amorphous silica.

One hypothesis for the increased background noise is that samples were not perfectly flat because they were wet. This is unlikely as several samples were run both dry and wet with water in the Bruker D2 Phaser instrument prior to this study to determine if running wet samples would negatively affect diffraction pattern backgrounds. No difference was noted and it was determined that ethylene glycol solvation likewise would not pose such problems. Another possibility is that amorphous silica present in these samples absorbed some ethylene glycol, although this would only explain the increased background hump centered at $\sim 30^\circ$ 2θ and not the additional hump at $\sim 12^\circ$ 2θ .

2.7 Discussion

2.7.1 Isolation of Clays for XRD Analyses

After removing sulfates, concentrating clay-sized particles, and plating samples with preferred orientation, we detected or confirmed clays in four samples of acid sulfate altered basalt from Costa Rica (Table 2.2; Figures 2.6, 2.7, 2.8, and 2.9). Kaolinite was identified in all four, and one sample also contained montmorillonite. Prior to the clay isolation procedure, kaolinite was tentatively identified in two samples (Tu Center Crater 1 and Tu Center Crater 3) with the Bruker D2 Phaser XRD instrument, but was not detected with the Terra XRD instrument. These tentative kaolinite detections were confirmed after the procedure using the

Bruker D2 Phaser instrument, but kaolinite was still not observed in the Terra XRD diffraction patterns.

2.7.2 Implications for *In situ* Clay Analyses

Traditional sample preparation for clay mineral XRD analysis is not feasible on Mars. However, each step of our procedure (sulfate removal, particle size separation, and plating with preferred orientation) was useful in isolating clay minerals for XRD analysis. Sulfate removal and dispersion reduced or eliminated non-clay mineral peaks that interfered with clay peaks in diffraction patterns. For example, prior to the removal of natroalunite, the natroalunite peak at $\sim 25.5^\circ 2\theta$ masked the kaolinite peak at $\sim 24.9^\circ 2\theta$ in Poás Fluv Clay 2 (Figure 2.6). Flocculation concentrated clays for plating with preferred orientation, which facilitates clay identification by increasing the basal (00 l) reflection. Although it was not essential for this study, ethylene glycol solvation can be used after clay isolation and orientation to expand smectite layers, thereby causing peak shifts that can significantly assist in distinguishing between different smectites.

If it were possible to perform any part of the clay isolation procedure on Mars, it would significantly aid in the detection and characterization of clays. For example, removal of jarosite and trace amounts of anhydrite and bassanite detected in samples from Gale Crater [Vaniman *et al.*, 2014; Cavanagh *et al.*, 2015; Rampe *et al.*, 2015, 2016; Treiman *et al.*, 2016] would improve the visibility of clay mineral peaks in CheMin diffraction patterns. Although not performed in this study due to concerns about altering clay XRD responses, chemical removal of hematite and magnetite identified at Gale Crater [Vaniman *et al.*, 2014; Cavanagh *et al.*, 2015; Rampe *et al.*, 2015, 2016] could also eliminate peaks that interfere with clay mineral peaks. In addition, ethylene glycol solvation would greatly assist smectite characterization at Gale Crater, as suspected differences in swelling behavior and layer collapse have complicated smectite identification in Cumberland, John Klein, Windjana, and Confidence Hills samples [Vaniman *et al.*, 2014; Bristow *et al.*, 2015; Cavanagh *et al.*, 2015; Treiman *et al.*, 2016]. Analysis of these samples before and after ethylene glycol solvation would improve confidence

in the ferrian saponite identification by creating a consistent interlayer expansion across samples.

2.7.3 Implications for Interpreting Clay Mineral Assemblages on Mars

Clays were identified in samples collected from an active fumarolic region (T~60-100°C, pH 3-5; Tu N6), from the edge of the Turrialba center crater above the lake shoreline (Tu Center Crater 1 and 3), and from an outwash basin frequently inundated with acidic (pH~0.3) lake water and wet hot pyroclastics (Poás Fluv Clay 2). Kaolinite formed alongside natroalunite, cristobalite, anatase, and amorphous silica from incompletely weathered basalt at the Tu Center Crater, Tu N, and Poás Fluv sites. Calcium sulfates (gypsum and anhydrite), goethite, and hematite were also present at Tu N, and tridymite, magnetite, hematite, and montmorillonite at Poás Fluv. On Earth, similar mineral assemblages have been reported at volcanoes in Nicaragua [*Hynek et al.*, 2013; *McCullom et al.*, 2013a], sulfuric acid caves in New Mexico [*Polyak and Güven*, 1996; *Polyak et al.*, 2006], and volcanic ash weathered by solfataric alteration at the Deccan Volcanic Province in India [*Siva Siddaiah and Kumar*, 2009], to name a few examples.

Although Al phyllosilicates such as kaolinite and montmorillonite are less common on Mars than are Fe,Mg smectites and chlorites, these clays still comprise ~20% of the sedimentary clays and ~33% of the clays in stratigraphies on Mars [*Ehlmann et al.*, 2011]. Mineral assemblages analogous to those at Turrialba and Poás have been identified at Noctis Labyrinthus [*Weitz et al.*, 2011; *Thollot et al.*, 2012], and at Cross Crater [*Ehlmann et al.*, 2016] and Columbus Crater [*Wray et al.*, 2011] in the Terra Sirenum region. Acid sulfate alteration processes similar to those currently occurring at Turrialba and Poás may have formed these mineral assemblages on early Mars. Acid sulfate alteration has also been proposed to explain mineral assemblages at Northeastern Syrtis Major [*Ehlmann and Mustard*, 2012], Gusev Crater [*Ming et al.*, 2006; *Arvidson et al.*, 2008; *Yen et al.*, 2008], Meridiani Planum [*McCullom and Hynek*, 2005], and Mawrth Valles [*Farrand et al.*, 2009], among other sites.

In regards to the Curiosity rover investigation, the mineral assemblage at the Poás Fluv site in particular resembles that of Confidence Hills and Mojave 2, two samples drilled in the basal member of the Murray Formation at Mt. Sharp [Rampe *et al.*, 2016]. Mafic minerals, amorphous silica, cristobalite, tridymite, alunite-jarosite group minerals, hematite, magnetite, and phyllosilicates are present at both the Poás Fluv site and in the Murray Formation [Rampe *et al.*, 2016], which suggests that similar acid sulfate alteration pathways formed these mineral assemblages. At the Poás Fluv site, runoff from precipitation transports primary igneous material and minerals formed via water-limited acid fumarolic weathering from the surrounding dome edge, crater walls, and rim to the edge of the lake, where further alteration and input occurs when the outwash basin is inundated by the acid sulfate lake or pyroclastics. Based on the similarity of the mineral assemblages at these sites, we propose that Poás volcano may be a useful analog for understanding the mineralogy of the Murray Formation at Gale Crater.

Characterizing samples from an analog site following clay isolation may be particularly useful to “ground-truth” interpretations of upper members of the Murray Formation. Phyllosilicates were detected in minor amounts (<10 wt%) in Confidence Hills and Mojave 2, but were not detected in either Telegraph Peak (~6 meters above Mojave 2) or Buckskin (~6 meters above Telegraph Peak) [Morris *et al.*, 2016; Rampe *et al.*, 2016]. Rampe *et al.* [2016] therefore proposed that the Murray Formation mineral assemblage formed by lacustrine deposition of mafic minerals, phyllosilicates, and magnetite followed by the downward migration of acid sulfate fluids that leached mobile elements, partially dissolved igneous minerals and phyllosilicates, and precipitated jarosite and hematite. However, without the ability to remove non-clay minerals, isolate the clay-size fraction, and preferentially orient samples, CheMin may be unable to detect phyllosilicates in Telegraph Peak and Buckskin present at lower abundances than in Confidence Hills and Mojave 2. In this case, the diagenetic model of clay dissolution proposed by Rampe *et al.* [2016] is not required to explain the Murray Formation,

and alternative interpretations of how this stratigraphic sequence was deposited and altered should be considered, such as acid sulfate alteration alone as inferred for Poás.

2.8 Conclusion

We find that clay isolation through removal of non-clay minerals, particle size separation, and preferred orientation significantly improves clay detection and characterization with XRD in comparison to methods available to the CheMin instrument on Curiosity. Out of 14 samples studied of acid sulfate altered basalt from Costa Rican analogs to Mars, we identified kaolinite in four samples and montmorillonite in one using a laboratory XRD instrument. Kaolinite was not detected in two of these samples prior to the clay isolation procedure with the CheMin analog instrument, and was only successfully characterized after the procedure with the traditional laboratory XRD instrument. As the Terra XRD instrument was designed with a 1 wt% detection limit [Treiman *et al.*, 2010], and CheMin has a detection limit of 3 wt% [Blake *et al.*, 2012], CheMin would be further limited in its ability to detect kaolinite in these samples.

Although the clay isolation procedure generally did not remove all non-clay minerals, particularly sulfates, intensities of clay XRD peaks increased relative to non-clay mineral peaks, which greatly aided in clay detection and characterization. The challenge of implementing any part of this procedure on Mars suggests that greater caution must be taken in interpreting CheMin results. If CheMin, like the analogous Terra XRD instrument, cannot detect all clays in a sample without additional clay isolation steps, an accurate mineralogical assessment of a given site may not be possible. This may be particularly relevant to Curiosity's ongoing investigation of the Murray Formation at the base of Mt. Sharp, which has a mineral assemblage similar to that found at Poás volcano. CheMin has detected minor abundances of phyllosilicates at the base of the Murray Formation, but not farther up section; this could reflect differences in the depositional or alteration processes, or could be due to CheMin's inability to detect all clays in the sequence. Missing clay detections would affect interpretations of aqueous and geochemical processes and

habitability during the deposition and diagenesis of the Murray Formation and other mineral assemblages found at Gale Crater.

CHAPTER 3:

INVESTIGATING IRON SUBSTITUTION IN NATROALUNITE AT TERRESTRIAL ANALOGS
FOR EARLY MARS

3.1 Abstract

The mineral jarosite ($\text{KFe}_3(\text{SO}_4)_2(\text{OH})_6$) was first discovered on Mars in 2004 at Meridiani Planum. Jarosite forms under highly acidic ($\text{pH} < 4$), highly oxidizing, sulfur-rich conditions, which seriously constrains the geochemistry of early Mars. However, recent work suggests that some or all of the jarosite identified on Mars could be natroalunite ($\text{NaAl}_3(\text{SO}_4)_2(\text{OH})_6$) with substitution of iron for aluminum. Natroalunite can form over a broader range of pH, water:rock ratios, and redox conditions than can jarosite, therefore detecting iron-rich natroalunite on Mars could affect interpretations of early Mars' geochemistry and habitability. To determine if iron-rich natroalunite is a common alteration product at Mars analog sites, we evaluated iron content in natroalunite from Poás and Turrialba volcanoes in Costa Rica. We detected iron-rich natroalunite (up to ~30% iron substitution) at diverse geochemical settings across these two volcanoes. In addition to characterizing the extent and distribution of iron in natroalunite, we evaluated the feasibility of using x-ray diffraction (XRD) and Raman spectroscopy for *in situ* iron-rich natroalunite detection on Mars. We determined that CheMin, the XRD instrument on the Curiosity rover, and the Raman Laser Spectrometer on the upcoming ExoMars rover could detect iron-rich natroalunite with $\geq 25\%$ iron substitution. These findings are applicable to the Curiosity rover's ongoing investigation of Gale Crater, where the rover recently detected jarosite. Distinguishing between iron-rich natroalunite and jarosite on Mars could aid in interpreting geochemical conditions during mineral formation, which has implications for the habitability of early Mars.

3.2 Introduction

3.2.1 Sulfate Detections and Formation on Mars

In 2005, the Observatoire pour la Mineralogie, l'Eau, les Glaces et l'Activité (OMEGA) on Mars Express unambiguously detected sulfates on Mars [Gendrin *et al.*, 2005]. Since then, orbiters have discovered gypsum, kieserite, and additional mono- and polyhydrated Ca- and Mg-sulfates across Mars [Arvidson *et al.*, 2005; Bibring *et al.*, 2005, 2006; Gendrin *et al.*, 2005; Langevin *et al.*, 2005; Poulet *et al.*, 2007; Murchie *et al.*, 2009]. *In situ* observations with Mars Exploration Rovers Opportunity and Spirit found Mg- and Ca- sulfates at Meridiani Planum [Squyres *et al.*, 2004a; Squyres and Knoll, 2005], and Mg- and Fe(III) sulfates in Paso Robles and Troy soils at Gusev Crater [Gellert *et al.*, 2006; Ming *et al.*, 2006; Morris *et al.*, 2006; Squyres *et al.*, 2006; Yen *et al.*, 2008; Arvidson *et al.*, 2010]. Opportunity also identified Na- or K-rich jarosite with possible minor Al substitution for Fe with Mössbauer spectroscopy at Meridiani Planum [Klingelhöfer *et al.*, 2004]. More recently, the Curiosity rover has detected anhydrite, bassanite, and jarosite with x-ray diffraction at Gale Crater [Bish *et al.*, 2013; Vaniman *et al.*, 2014; Cavanagh *et al.*, 2015; Rampe *et al.*, 2015, 2016; Treiman *et al.*, 2016].

Although different mechanisms for sulfate formation may have operated at various times across Mars, hydrothermal acid sulfate weathering of basaltic crust is the most likely process responsible for assemblages identified at several sites. The detection of jarosite at Meridiani Planum is indicative of an aqueous acid sulfate alteration process at low water-rock ratios and pH ~2 to 4 [Elwood Madden *et al.*, 2004; Klingelhöfer *et al.*, 2004]. McCollom and Hynek [2005] proposed that jarosite and other hydrated sulfates at Meridiani Planum formed through fumarolic acid sulfate activity. Sulfate- and silica-rich soils and deposits at Gusev Crater are also interpreted as having formed through volcanic acid sulfate weathering [Arvidson *et al.*, 2008; Yen *et al.*, 2008]. In concert with these interpretations of *in situ* findings, orbital observations of diverse mineralogical assemblages, such as Fe(III) sulfates co-located with phyllosilicates and silica at Noctis Labyrinthus [Weitz *et al.*, 2011; Thollot *et al.*, 2012], likely formed through

hydrothermal acid sulfate alteration . Hydrothermal, acidic, sulfur-rich alteration of volcanic ash could have even extended beyond these localized sites and produced many of the layered sulfate deposits detected from orbit [Gendrin *et al.*, 2005].

3.2.2 Previous Work

Recent work suggests that some or all of the jarosite identified with the Mössbauer instrument on Opportunity could instead be Fe-rich natroalunite, as Mössbauer spectra of jarosite and Fe-rich natroalunite are almost indistinguishable (McCollom *et al.*, 2013b, 2014). These minerals are members of the alunite-jarosite group, which have an idealized formula of $AB_3(SO_4)_2(OH)_6$ with K^+ , Na^+ (natro-) or H_3O^+ (hydronium) and occasional minor Ca^{2+} (-2c) in the A site and Fe^{3+} or Al^{3+} in the B site (Table 3.1). In this paper, minerals with >50% Fe^{3+} are

Mineral end-member	Formula
Alunite	$KAl_3(SO_4)_2(OH)_6$
Natroalunite	$NaAl_3(SO_4)_2(OH)_6$
Natroalunite-2c (minamiite)	$Na_{0.6}Ca_{0.3}K_{0.1}Al_3(SO_4)_2(OH)_6$
Jarosite	$KFe_3(SO_4)_2(OH)_6$
Natrojarosite	$NaFe_3(SO_4)_2(OH)_6$
Hydroniumjarosite	$(H_3O^+)Fe_3(SO_4)_2(OH)_6$

Table 3.1: Idealized molecular formulae for common alunite-jarosite group minerals.

considered members of the jarosite subgroup and those with >50% Al^{3+} are members of the alunite subgroup. Cations in the A site display extensive solid solution state mixing, but limited mixing between Fe^{3+} or Al^{3+} was reported prior to 2013 in natural samples, although Fe-Al solid solutions were readily synthesized in laboratory settings [Brophy *et al.*, 1962; Stoffregen *et al.*, 2000; Papike *et al.*, 2006; McCollom *et al.*, 2013b]. Hynek *et al.* [2013] and McCollom *et al.*

[2013b] found that natroalunite naturally forming at several Nicaraguan volcanoes displayed Fe substitution in the *B* site with several samples spanning a wide range of Fe-Al compositions, up to almost 40% Fe-substitution for Al.

After this discovery, *McCollom et al.* [2014] investigated methods to detect Fe substitution in natroalunite with instruments applicable to mineralogy analyses on Mars. They synthesized and then characterized solid solutions between natroalunite and natrojarosite end-members with X-ray diffraction (XRD) and Raman, visible/near infrared, mid-infrared, and Mössbauer spectroscopies. Variations in diffraction patterns and spectra were found that could be used to distinguish between natroalunite and natrojarosite end-members and to approximate Fe-content of alunite-jarosite minerals on Mars.

The distinction between alunite and jarosite is crucial for interpretations of geochemical conditions during formation. Alunite minerals can form at higher pH (<5.5) than can jarosite (<4) [*Stoffregen et al.*, 2000; *Wray*, 2011] and remain stable at these higher pHs, while jarosite dissolves to form iron oxides at pH>4 or less [*Stoffregen et al.*, 2000; *Elwood Madden et al.*, 2004, 2012]. On Earth, jarosite is commonly associated with acid mine drainage and forms through the oxidation of iron sulfides, acid fog or fumarolic activity, or hydrothermal acid sulfate fluids, while alunite is commonly associated with lacustrine, weathering, or acidic hydrothermal environments [*Stoffregen et al.*, 2000; *Drouet et al.*, 2004]. On Mars, the discovery of alunite in Cross Crater is interpreted as evidence of upwelling acidic groundwaters, with geochemical modelling suggesting less acidic and less oxidizing conditions than those required for jarosite to have formed at Cross Crater [*Ehlmann et al.*, 2016].

To determine if iron-rich natroalunite is exclusive to acid sulfate alteration processes occurring in Nicaragua, we characterized iron content in natroalunite formed from different parent lithology. Here, we report iron substitution in natroalunite at Poás and Turrialba volcanoes in Costa Rica and evaluate the use of x-ray diffraction (XRD) and Raman spectroscopy in detecting Fe-rich natroalunite *in situ*. Because alunite minerals can form at

higher pH and water:rock ratios than can jarosite, the ability to distinguish between jarosite and iron-rich natroalunite with CheMin, the XRD instrument on the Curiosity rover, and with the Raman Laser Spectrometer on the upcoming ExoMars rover will enable better interpretations of geochemical conditions and habitability on early Mars.

3.3 Field Site Descriptions and Sample Collection

Fieldwork was conducted in November 2013 at Poás and Turrialba volcanoes in Costa Rica (Figure 3.1). The subduction of the Cocos Plate beneath the Caribbean Plate forms the Central American volcanic chain, which stretches 1100 km from Costa Rica through Guatemala [Prosser and Carr, 1987; Cigolini *et al.*, 1991]. Poás and Turrialba are members of Cordillera Central, a large massif of overlapping pyroclastic deposits in central Costa Rica [Prosser and Carr, 1987]. The lava composition in central Costa Rica is generally consistent with an ocean island basalt (OIB) with minimal contribution from the subducting slab, although He isotopic analysis suggests Turrialba has minor mid-ocean ridge basalt (MORB) components [Herrstrom *et al.*, 1995; Di Piazza *et al.*, 2015]. In contrast, Nicaraguan lavas studied by McCollom *et al.* [2013a, 2013b] and Hynek *et al.* [2013] and used for comparison here have a much greater contribution from the subducting slab due to thinner lithosphere, and a dominantly MORB composition [Herrstrom *et al.*, 1995].

Turrialba's current volcanic activity began ~1 million years ago, although the volcano overlies andesitic lavas dated at 2.15 ± 0.30 Ma [Reagan *et al.*, 2006]. Turrialba has three interior craters referred to as the center, east, and west craters, and an andesitic to basaltic lava composition [Reagan *et al.*, 2006; Di Piazza *et al.*, 2015]. Turrialba's most recent major eruptive period occurred between 1864 and 1866 and resulted in pyroclastic deposits, lahars, and ash deposits [Reagan *et al.*, 2006]. Some eruptive activity continues to the present, including phreatic eruptions in January 2010 and January 2012 that formed new openings near the west crater [van Manen, 2014; Di Piazza *et al.*, 2015].

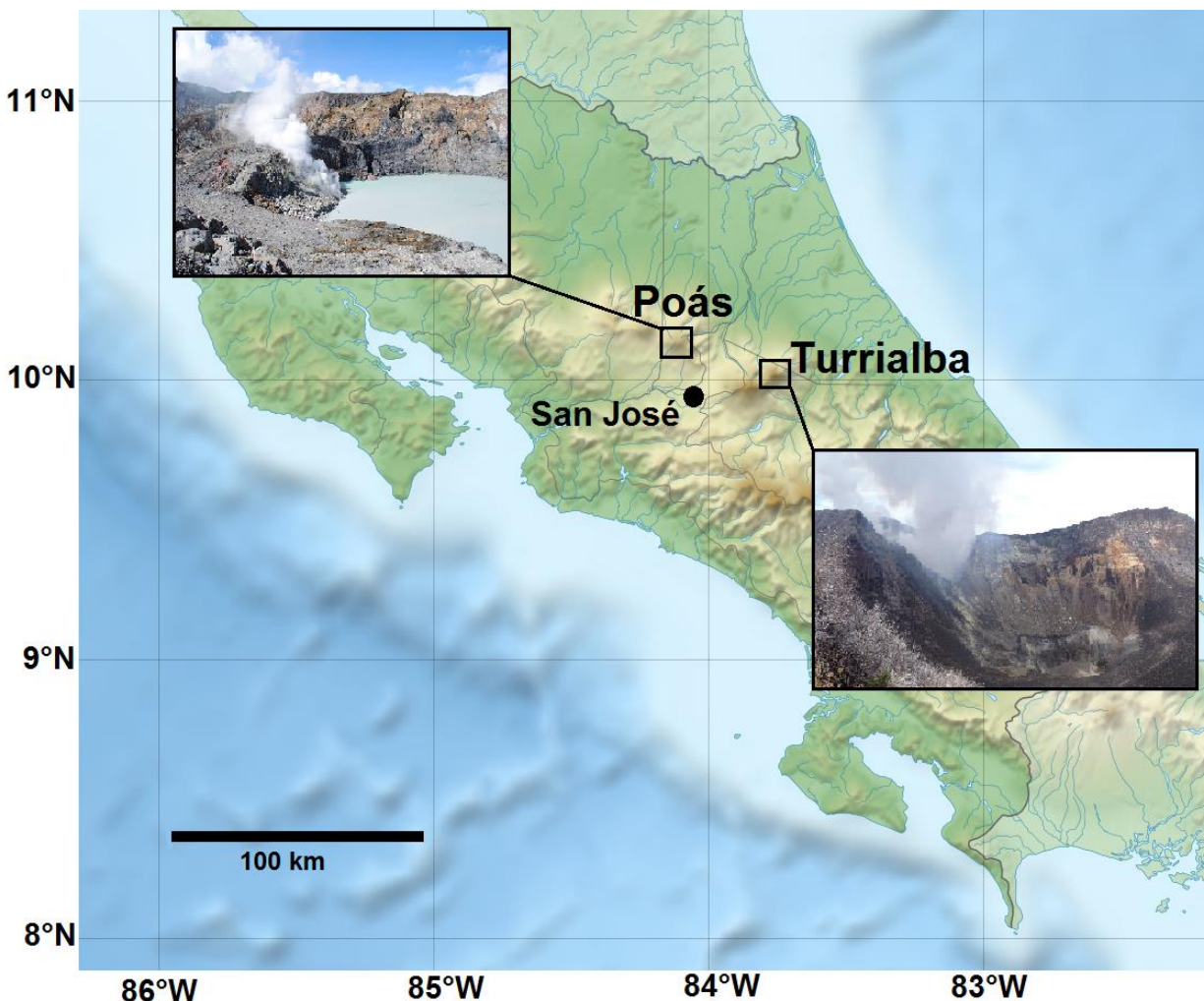


Figure 3.1: Fieldwork was conducted at Poás Volcano and Turrialba Volcano [photos inset]. The two volcanoes are part of the Central American Volcanic Chain formed by the subduction of the Cocos Plate under the Caribbean Plate. Adapted from elevation map by Eric Gaba.

Poás also is also ~1 million years old and has been continuously mildly active throughout its recorded history, with ongoing fumarole activity and frequent phreatic eruptions [Prosser and Carr, 1987; de Moor et al., 2016]. Between 2006 and 2014, Poás was highly active, with ~60 recorded phreatic eruptions from the crater lake in 2014 alone that ranged from small gas emissions to major pyroclastic eruptions reaching >400 m high [de Moor et al., 2016]. Magma composition shows a cyclical sequence of felsic to mafic, with recent eruptions indicating that Poás is currently in the mafic stage [Prosser and Carr, 1987]. Poás and Turrialba

have more calcic plagioclase ($\sim\text{An}_{50-70}$) than does Mars ($\sim\text{An}_{40-55}$) and a more minor olivine contribution [e.g., *Bibring and Erard, 2001; Bandfield, 2002; Christensen et al., 2003*], but overall mineralogy is relatively comparable .

Samples were collected from several sites at each volcano chosen to represent a range of environmental conditions (Figures 3.2 and 3.3). Sites ranged from outwash basins near crater lakes to active fumaroles. Temperatures and pH at the time of sampling ranged from $\sim 16^\circ\text{C}$ to 180°C and from <1 to 5, respectively. Samples had a variety of physical appearances, with colors including white, yellow, red, and purple, and were predominantly loose sediments or hand samples.

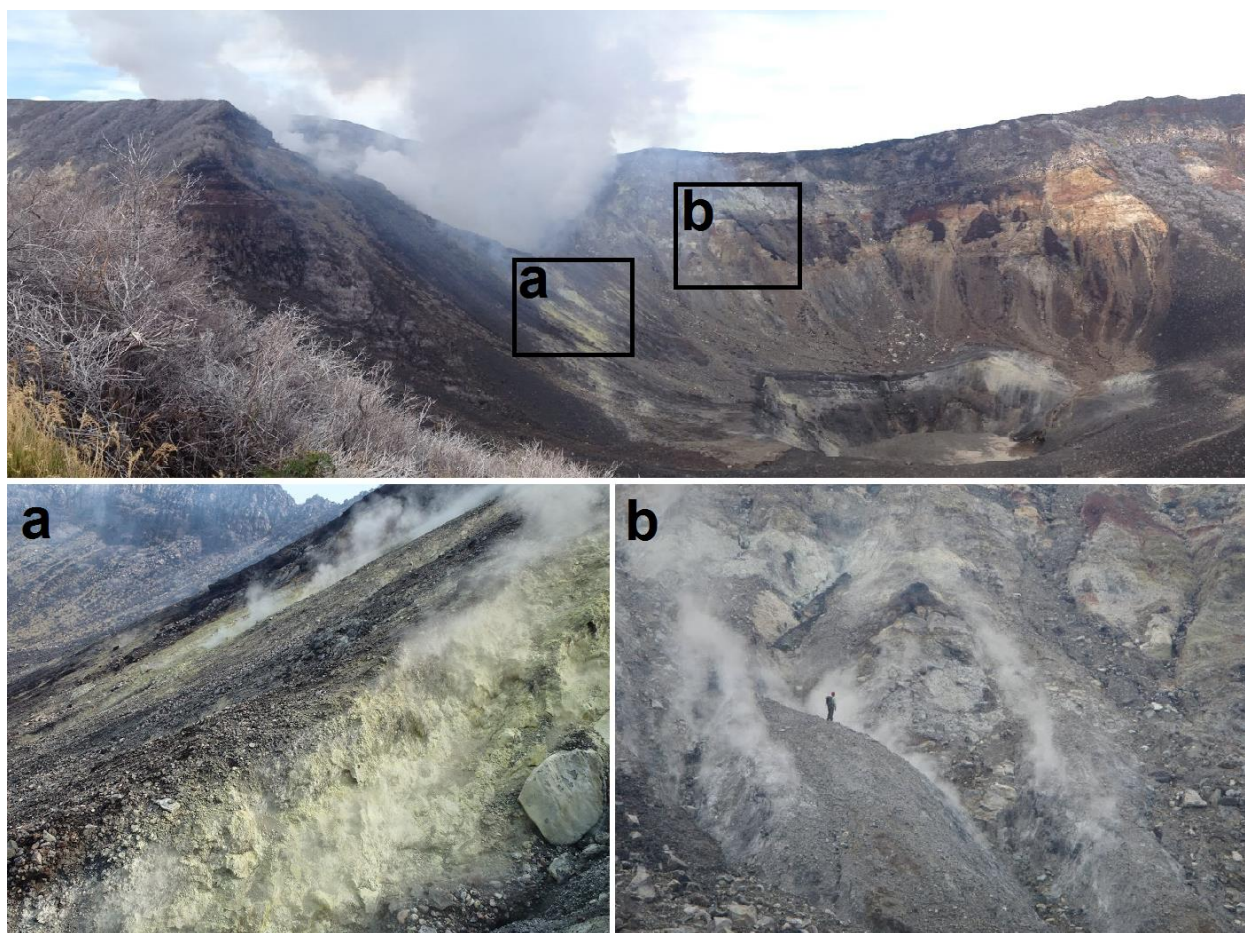


Figure 3.2: Sampling sites at Turrialba volcano used in this study: (a) Ttop samples were collected from roughly meter deep parallel gullies on the western crater's outer slope, and (b) TuN samples are from active fumaroles north of the center crater. Note person for scale in (b).



Figure 3.3: Sampling sites at Poás Volcano used in this study: (a) PDE samples come from edge of the small dome, and (b) PF samples were collected several meters west of PDE samples and immediately adjacent to active fumaroles.

Samples selected for this study came from two of three sampling sites at Turrialba and two of four sites at Poás. “Ttop” samples came from active fumaroles north of the center crater lake with temperature $\sim 60\text{-}100^\circ\text{C}$ and pH 3-5 at time of sampling (Figure 3.2a). “TuN” samples were from fumarolic gullies on the western crater’s outer slope with temperature $\sim 100^\circ\text{C}$ and pH 1.5-2 (Figure 3.2b). The “PF” sampling site was immediately adjacent to active fumaroles on the crater lake’s southern rim and had a temperature $\sim 90^\circ\text{C}$ and $\text{pH} < 1$ at time of sampling (Figure 3.3a). “PDE” samples were collected a few meters from PF samples on the edge of a small dome at ambient temperature and too dry for pH measurements during fieldwork (Figure 3.3b).

3.4 Methods

We evaluated all 57 samples collected from Poás and Turrialba with X-ray diffraction (XRD) analyses, which were performed with a field portable Terra X-ray diffraction/X-ray fluorescence (XRD/ XRF) instrument (formerly inXitu Incorporated, Campbell, CA, now marketed by Olympus Corporation, Tokyo, Japan). This instrument was designed as a commercial testbed for CheMin on Curiosity, which is currently operating in Gale Crater [Blake *et al.*, 2012]. We prepared samples by gently grinding and dry sieving to $<150\ \mu\text{m}$. The Terra instrument uses a stationary x-ray beam and continuously vibrates samples to produce a randomly oriented powder.

The instrument was operated at 30 kV with $\text{CuK}\alpha$ radiation ($\lambda = 1.5418\text{\AA}$) in the range of $5\text{-}55^\circ\ 2\theta$ and has a step size of $0.05^\circ\ 2\theta$ and a precision of $0.25^\circ\ 2\theta$ FWHM. We also analyzed several samples with a Bruker D2 Phaser XRD operated at 30 kV and 10 mA using $\text{CuK}\alpha$ radiation in the range $5\text{-}55^\circ\ 2\theta$ with a step size of 0.02 and collection time of 1 s per step. We used X Powder and the Diffrac Suite for analyses conducted with the Terra and Bruker D2 Phaser instruments, respectively. We then chose six samples with high natroalunite content for further analytical techniques.

Additional analyses were conducted with an electron microprobe (EMP), a scanning electron microscope (SEM) equipped with an electron-dispersive X-ray spectrometer (EDS), and a Raman microscope-spectrometer. EMP analyses were conducted on a JEOL JXA 8600 Electron Microprobe at the University of Colorado (CU) Boulder equipped with four wavelength dispersive spectrometers and Geller dQuant software. Samples were mounted in epoxy and carbon coated to prevent charging. We used feldspars as standards for sodium, silicon, aluminum, and potassium; olivine as the standard for iron, garnet as the manganese standard, and barite as the sulfur standard. An accelerating voltage of 15 kV was used. Most analyses were conducted with a $10\ \mu\text{m}$ beam and a beam current of 5 or 10 nA, but we also used beam sizes of $15\ \mu\text{m}$ and a 2.5 nA current for some samples due to concerns about beam damage.

Carbon-coated sample mounts prepared for EMP analyses were also used for SEM-EDS analyses, which we conducted on a JEOL 6480LV at CU Boulder in backscattered electron mode with an accelerating voltage of 15 kV. Spot size was set to 60 or 65 and working distance was 10 ± 1 mm. EDS analyses were performed with an Oxford Instruments collector and processed using INCA software.

We conducted Raman analyses with a Horiba LabRAM HR Evolution Raman microscope-spectrometer at CU Boulder. Analyses were conducted with a green (532 nm) laser on the sieved (<150 μm) powders used for XRD analyses with both single point analyses and compositional mapping across a small area of natroalunite. We used beam sizes from ~ 2 to 5 μm to obtain a complete assessment of a given grain and its context, and used a range of laser power (~ 30 to 50 mW), acquisition times, and number of acquisitions based on mineral susceptibility to burning. ICS corrections were applied to the initial spectra and fluorescent effects were removed. We then matched processed spectra to spectra from the RRuff database library with the KnowItAll software package. Raman spectra and XRD patterns were compared to spectra and patterns of natroalunite-natrojarosite standards synthesized by *McCollom et al.* [2014].

3.5 Results

A total of 57 samples were collected from Poás and Turrialba and analyzed with the Terra instrument. Of >30 samples containing natroalunite, six with an estimated ≥ 50 wt% natroalunite or natroalunite-2c were chosen for this study (Table 3.2, Figures 3.4 and 3.5). Three samples were from Poás and three from Turrialba, representing two sampling sites at each volcano. Other minerals in these samples included amorphous silica, hematite, jarosite, gypsum, and cristobalite (Table 3.2).

Sample	Mineralogy
TuN5	Natroalunite, cristobalite*, gypsum*, amorphous silica
Ttop2	Gypsum, natroalunite, amorphous silica
Ttop6	Hematite, natroalunite, amorphous silica
PDE1	Natroalunite, jarosite, amorphous silica, cristobalite ⁺
PDE3	Natroalunite-2c, labradorite, cristobalite, amorphous silica
PF9	Natroalunite, hematite

Table 3.2: Mineralogy from the Terra XRD instrument of the six samples chosen for further analyses. Two samples (PDE3 and TuN5) were also analyzed with the Bruker D2 Phaser XRD instrument. *=mineral identified solely with Bruker XRD, +=tentative detection.

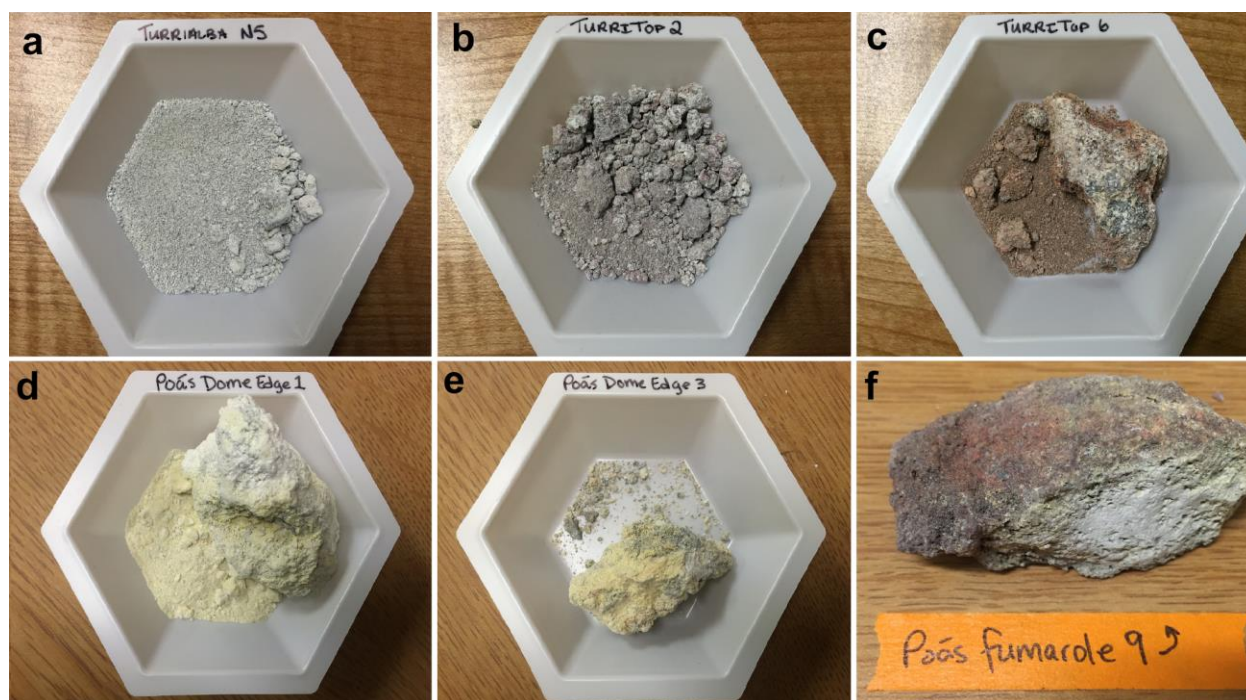


Figure 3.4: The six samples used in this study: (a) TuN5, (b) Ttop2, (c) Ttop6, (d) PDE1, (e) PDE3, and (f) PF9; a, b, and c are ~7 cm wide and d, e, and f are ~8 cm wide.

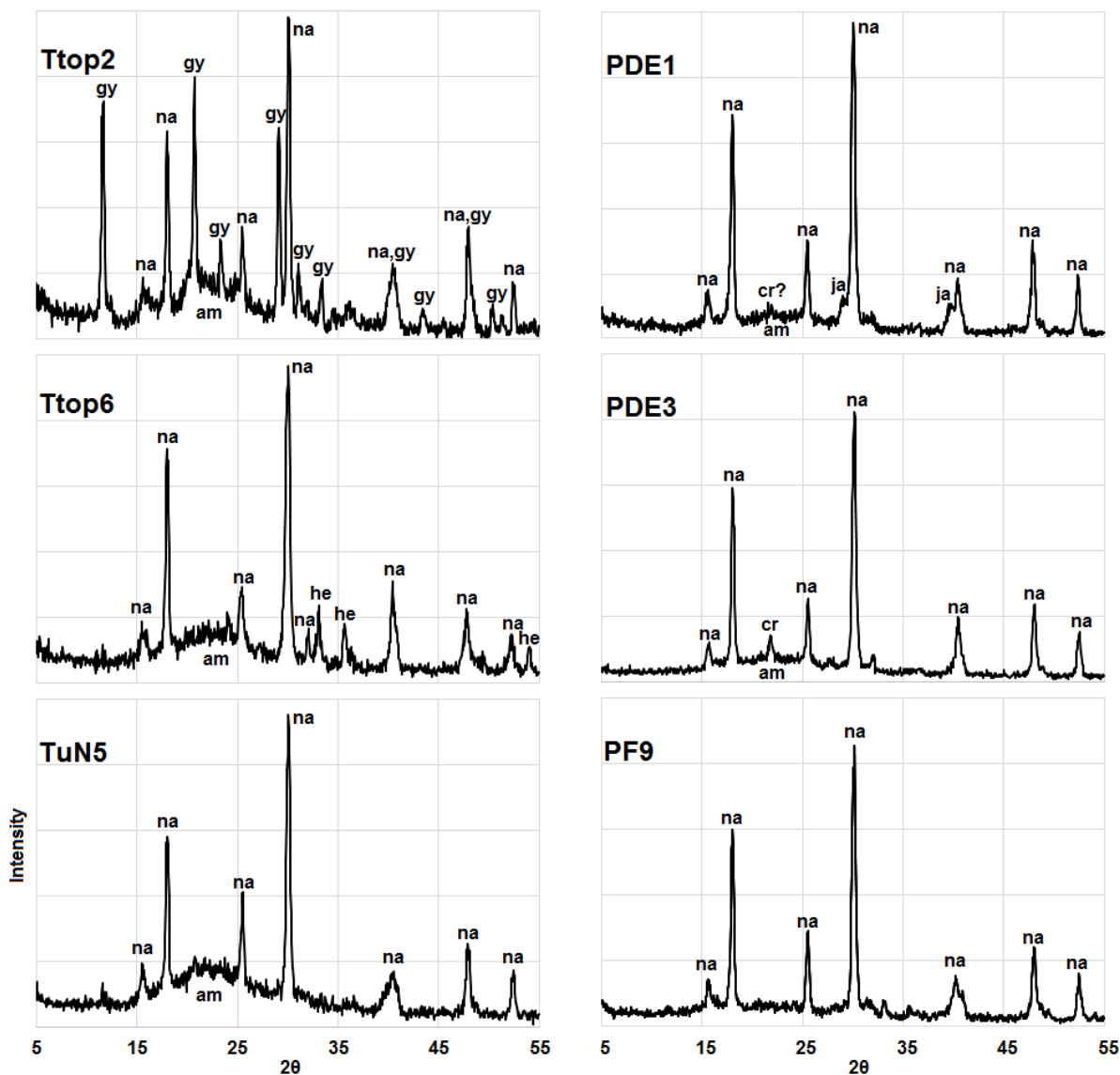


Figure 3.5: Diffraction patterns of the six samples chosen for this study. Labels: na=natroalunite or natroalunite-2c, am=amorphous silica, ja=jarosite, cr=cristobalite, gy=gypsum, and he=hematite.

3.5.1 Quantitative and Semiquantitative Analyses of Iron Content

EMP and SEM-EDS analyses detected Fe-rich natroalunite grains in four of the six samples. Elemental % and atomic % of Fe in natroalunite grains are reported as Fe# [=100 x Fe/(Al+Fe)], following the notation used in *McCollom et al.* [2013a, 2013b, 2014]. EMP and EDS analyses of grains in TuN5, Ttop6, PDE1, and PDE3 are summarized in Table 3.3. Chemical

compositions of selected natroalunite grains from EMP analyses are reported in Table 3.4, and chemical compositions from EDS analyses are reported in Table 3.5.

Sample	Method	# Analyses	Avg. Fe#	Std. Dev.	Range of Fe#s
TuN5 Grain1	EMP	5	2.4	0.3	-
TuN5 Total	EMP	14	1.9	0.8	0.7 - 3.4
TuN5 (with Fe)	EDS	3	3.1	1.0	2.5 - 4.5
TuN5 (no Fe)	EDS	2	No Fe detected		-
Ttop6 Grain 5	EMP	3	1.9	0.2	-
Ttop6 Grain 7	EMP	5	17	1.4	-
Ttop6 Total	EMP	16	11.5	9.5	1.8 - 33
Ttop6 (no Fe)	EDS	3	No Fe detected		-
Ttop6 (with Fe)	EDS	7	11	2.4	5.7 - 14
PDE1	EMP	16	0.6	0.5	0 - 1.4
PDE1	EDS	7	Fe-rich rims too thin for reliable analyses, or no Fe		-
PDE1	EDS	3	15	2.5	12 - 17
PDE3	EMP	4	4.8	1.9	3.3 - 7.6
PDE3	EDS	6	No Fe detected		-

Table 3.3: Summary of EMP and SEM-EDS analyses of representative natroalunite grains and overall average Fe#s of all natroalunite grains analyzes in TuN5, Ttop6, PDE1, and PDE3. No reliable analyses were feasible in Ttop2 and PF9.

Sample	Na	Mg	Al	Si	S	Cl	K	Ca	Fe	Mn	O	Total	Total +H2O	Fe#
TuN5	4.18	0.23	18.2	BD	14.9	0.85	1.07	0.16	0.36	BD	40.4	80.4	94.0	2.0
Ttop6 (3)	3.06	0.03	17.8	0.09	12.7	0.10	1.18	0.16	8.89	BD	40.2	84.2	97.8	33
Ttop6 (7)	3.18	0.03	17.7	BD	13.3	0.06	0.86	0.21	3.95	BD	38.7	78.0	91.6	18
PDE1	2.87	BD	20.2	0.07	14.6	0.07	0.56	0.83	0.23	BD	41.5	81.0	94.6	1.1
PDE3	1.63	0.10	18.8	0.18	14.0	0.61	0.57	0.23	1.54	BD	39.2	76.9	90.5	7.6

Table 3.4: Representative compositions (elemental %) of natroalunites determined by EMP. Two Ttop6 grains (grains 3 and 7) are shown to display the range of Fe# within that sample. BD=below detection limits.

Sample	TuN5	Ttop6 (high Fe)	Ttop6 (no Fe)	PDE1 (High Fe)	PDE1 (no Fe)
Element	Atomic percents (%)				
O	62.9	58.4	62.0	62.7	63.6
Na	2.91	2.76	2.54	2.79	2.13
Al	17.0	18.2	18.7	16.2	18.3
S	15.6	17.1	15.6	16.1	15.6
K	1.1	1.09	1.17	-	-
Ca	-	-	-	-	0.36
Fe	0.43	2.47	-	2.23	-
	Atoms per formula unit				
O	16.1	13.8	15.9	15.6	16.3
Na	0.52	0.45	0.45	0.48	0.38
Al	2.59	2.54	2.83	2.39	2.78
S	2.00	2.01	2.00	2.00	2.00
K	0.12	0.11	0.12	-	-
Ca	-	-	-	-	0.04
Fe	0.03	0.17	-	0.16	-
Fe#	2.5	12	-	12	-

Table 3.5: Representative compositions (atomic % and atoms per formula unit) of five natroalunite grains. Two grains are shown from both PDE1 and Ttop6 to demonstrate range of Fe content from below detection limit to ~12. Backscattered electron images of these representative TuN5, Ttop6 grain with no Fe; and both PDE1 grains are in Figure 3.6a, 3.6c, and 3.6d, respectively.

TuN5 and PDE3 grains had little iron substitution ($Fe\# < \sim 8$ for all analyses), while PDE1 and Ttop6 grains had $Fe\#$ s up to ~17 and ~33, respectively (Table 3.3, 3.4, 3.5; Figures 3.6 and 3.7). Similar to the findings of *McCullom et al.* [2013b], several grains displayed compositional zoning with Al-rich interiors and Fe-rich rims. These Fe-rich rim were generally too thin ($< 2 \mu\text{m}$) for reliable analyses, with the possible exception of one PDE1 grain with a wider rim ($Fe\# \sim 5.3$; Figure 3.6e). $Fe\#$ s also varied between grains within the same sample (e.g. PDE1, Figure 3.6d).

Although EMP analyses are considered quantitative, total elemental % were relatively low (~86-94%; Table 3.5). This may be due to loss of Na and K with beam damage in some grains, and interspersing of natroalunite with silica in other grains, particularly in PDE3, Ttop2, and PF9. Because of co-association with silica, only four reliable analyses of PDE1 were feasible, and no reliable analyses of Ttop2 grains were possible. Ti was not included in these

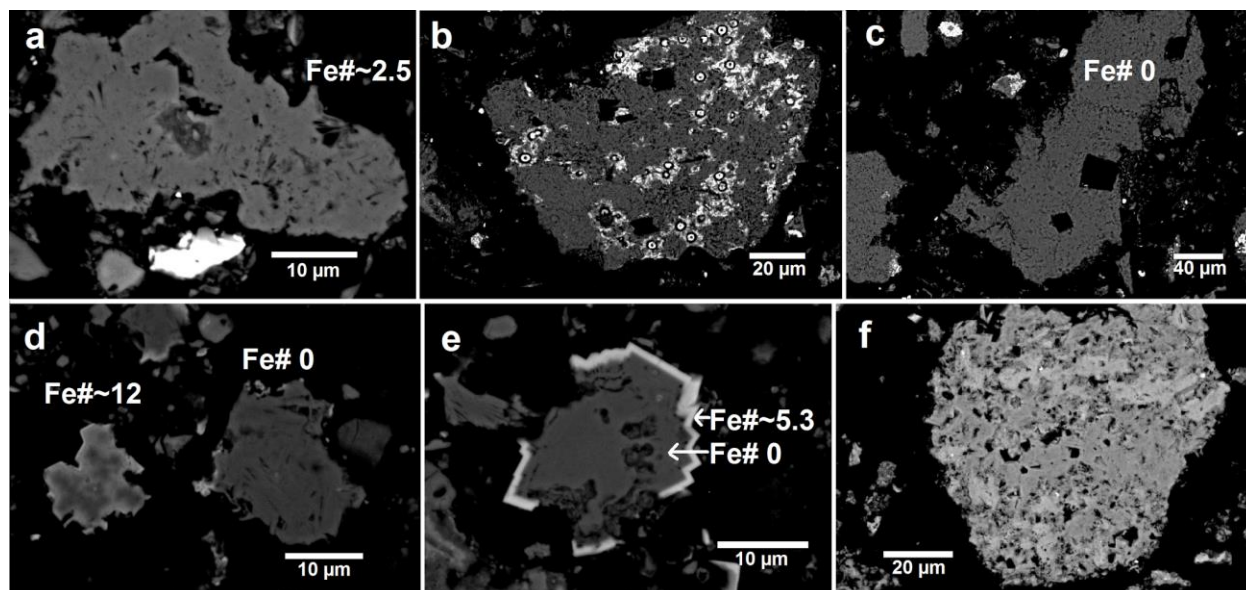


Figure 3.6: Backscattered electron images of representative natroalunite grains in TuN5, Ttop6, PDE1, and PDE3. SEM-EDS atomic % for grains in a, c, and d are reported in Table 5. (a) representative TuN5 natroalunite grain (Fe# ~2.5) above an iron sulfide; (b) Ttop6 grain with iron oxide spherules that hindered reliable analyses, (c) representative Ttop6 grain with no detectable iron, (d) two representative PDE1 grains; leftmost had Fe# ~12 and rightmost had no detectable iron, (e) Compositional zoning in PDE1 grain with no detectable iron in center and Fe-rich rim with Fe# ~5.3; (f) PDE3 grain of interspersed natroalunite and silica that hindered reliable analyses.

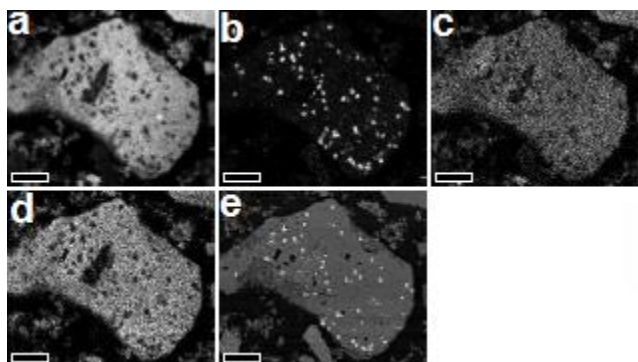


Figure 3.7: Elemental maps of (a) Al, (b) Fe, (c) K, and (d) Na, and backscattered electron image (e) of a Ttop6 grain with Fe# ~25. Scale bar = 20 μm . Note hematite spherules present on grain. Analyses were conducted $>10 \mu\text{m}$ from hematite spherules to ensure reliable analyses exclusively of natroalunite.

analyses, which could have had a minor effect on elemental % totals if trace Ti substitution for Al or Fe was present.

Ttop6 and PF9 had abundant hematite spherules $\leq 2 \mu\text{m}$ in diameter on many grain surfaces (Figures 3.7 and 3.8). Between silica and natroalunite intermixing in some grains and

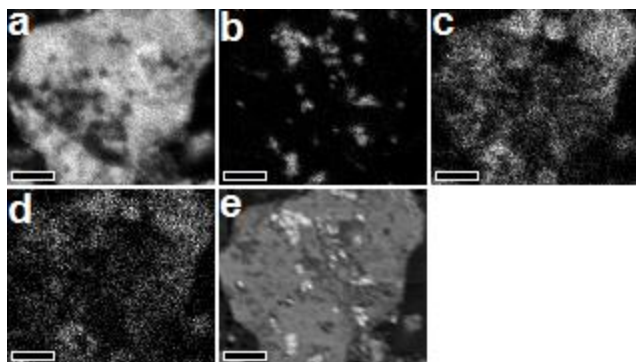


Figure 3.8: Elemental maps of (a) Al, (b) Fe, (c) K, and (d) Na, and backscattered electron image (e) of a PF9 grain covered with hematite spherules that prevented reliable analyses exclusively of natroalunite. Scale bar = 10 μm .

extensive hematite spherules coating others, no reliable EMP or EDS analyses were feasible for PF9 (Figure 3.8). In contrast, hematite spherules on Ttop6 grains were usually $>10\ \mu\text{m}$ apart, permitting relatively reliable analyses exclusively of natroalunite conducted with small beam diameters (Figure 3.7).

Semiquantitative EDS analyses generally agreed with EMP analyses within standard deviations for TuN5, Ttop6, and some PDE1 and PDE3 grains, suggesting that these analyses are relatively accurate (Tables 3.3, 3.4, and 3.5). All reliable EMP analyses of PDE1 had Fe#s <1.5 , which roughly concurs with seven EDS analyses of grains with no detectable iron (Table 3.3). However, EDS analyses of three other PDE1 grains had Fe#s of 12 to 17 (Table 3.3). No iron was detected with EDS analyses in PDE3, while EMP analyses identified PDE3 grains with Fe#s up to ~ 8 (Table 3.3).

3.5.2 Detecting and Estimating Iron Content with *In situ* Instruments

3.5.2.1 Raman

Raman shifts of three major peaks (~ 230 , ~ 390 , $\sim 1020\ \text{cm}^{-1}$) in the fingerprint region ($<1200\ \text{cm}^{-1}$) of natroalunite spectra were compared to peaks shifts of natroalunite-natrojarosite standards to approximate Fe#s (Table 3.6). Raman spectral patterns generally resembled natroalunite standards with Fe#10-Fe#20, suggesting minor Fe-substitution in all samples

	TuN5	Ttop2	Ttop6	PDE1	PDE3
Peak at ~230 cm ⁻¹	234	232	234	231	234
Peak at ~390 cm ⁻¹	394	394	392	391	395
Peak at ~1020 cm ⁻¹	1026	1024	1025	1024	1025
Approx. Fe# Range	~0-20	~10-30	~10-25	~20-40	~0-20

Table 3.6: Peak locations in natroalunite Raman spectra and approximate Fe# based on comparison to natroalunite-natrojarosite samples synthesized by *McCullom et al.* [2014]. Discrepancies between predicted Fe# based on peaks centered at ~230, ~390, ~1020 cm⁻¹ produced range of Fe#.

(Figure 3.9). Indications of significant iron content (Fe#>50), such as a shift in the prominent ν_1 symmetric stretching peak at ~1026 cm⁻¹ toward 1010 cm⁻¹, or the resolution of two broad peaks at ~480 and ~510 cm⁻¹ into one peak at ~450 cm⁻¹, were not apparent in any sample spectra.

Fe# estimates based on each of these three peaks disagreed with each other, and therefore a range of possible Fe#s for each sample is reported in Table 3.6. Fe# ranges for TuN5, PDE3, and Ttop6 grains roughly correlated with Fe#s calculated with EMP and EDS (Tables 3.3 and 3.6). Raman spectra provided insight into Fe-content in Ttop2 natroalunites (Fe#~10-30), which was not feasible with EMP or EDS due to silica intermixing in all observed grains. Without quantitative analyses, however, it is impossible to “ground-truth” this Fe# range in Ttop2.

In contrast to Fe# estimates obtained for TuN5, Ttop6, and PDE3, Raman peak shifts for PDE1 produced an estimated Fe# range (~20-40) that exceeded both EMP and EDS estimates (Fe#≤20; Table 3.3). This discrepancy could indicate either the presence of more Fe-rich natroalunite in PDE1 that was not detected with quantitative or semiquantitative methods, or the need for improved correlation between peak shifts and Fe-content.

As observed with EMP and EDS, abundant hematite spherules were visible on Ttop6 natroalunite grains (Figure 3.10). We exercised caution with Ttop6 analyses accordingly, and only used definitive natroalunite spectra to estimate Fe#s in this sample. No reliable analyses of natroalunites in PF9 were feasible, as grains exclusively co-occurred with other minerals.

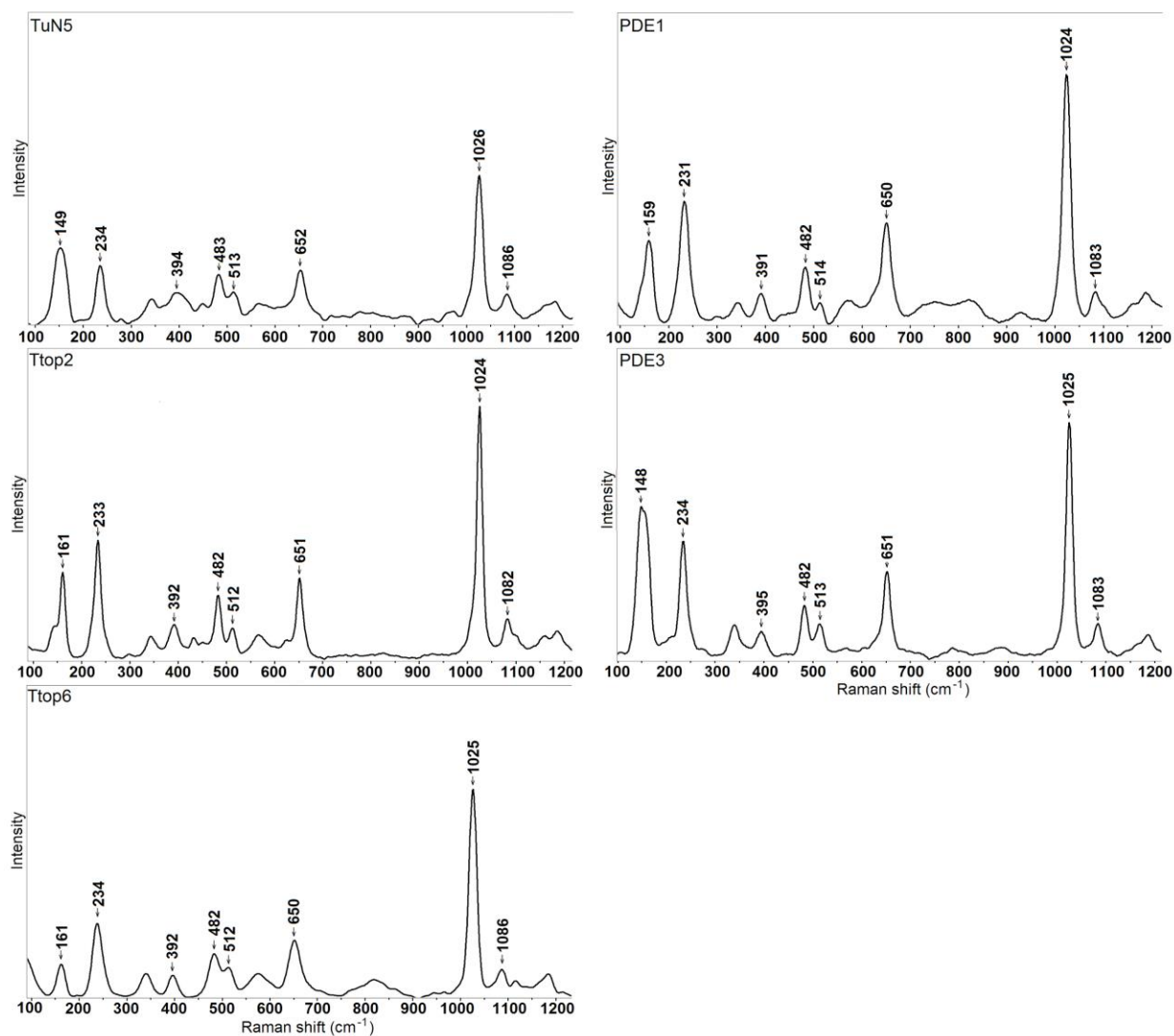


Figure 3.9: Average natroalunite Raman spectra from TuN5, Ttop2, Ttop6, PDE1, and PDE3.

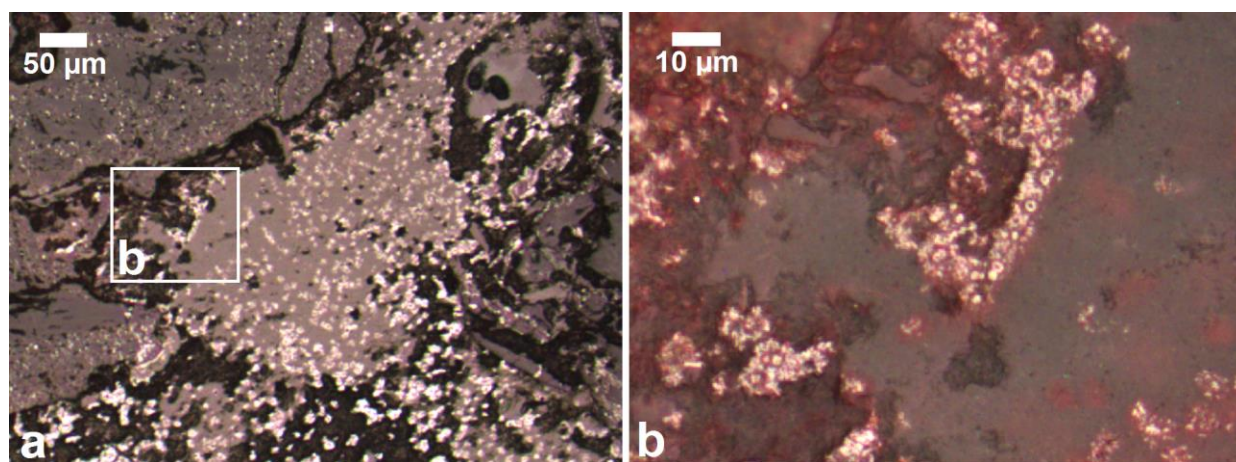


Figure 3.10: Raman microscope images of Ttop6. (a) Natroalunite grain coated with hematite spherules. (b) Close-up of section outlined in (a).

3.5.2.2 XRD

We also compared diffraction patterns of the six samples with XRD patterns of natroalunite-natrojarosite standards to estimate Fe-content (Table 3.7, Figure 3.5). We focused

	TuN5	Ttop 2	Ttop6	PDE1	PDE3	PF9
Peak at $\sim 18^\circ 2\theta$	18.00	18.00	18.05	18.05	18.05	18.05
Peak at $\sim 30^\circ 2\theta$	30.05	30.05	30.05	30.05	30.15	30.05
Approx. Fe# Range	$\sim 20-30$	$\sim 20-30$	$\sim 15-25$	$\sim 15-25$	$\sim 10-20$	$\sim 15-25$

Table 3.7: Peak locations in natroalunite diffraction patterns and approximate Fe# by comparison to natroalunite-natrojarosite samples synthesized by *McCullom et al.* [2014]. Discrepancies between predicted Fe# based on peaks at $\sim 18^\circ$ and $\sim 30^\circ 2\theta$ produced range of Fe#.

on shifts in the two highest intensity peaks at $\sim 18^\circ$ and $\sim 30^\circ 2\theta$, correlated with D1 and D2 spacing, respectively. As with Raman spectra peak shifts, diffraction patterns of all samples indicated some Fe-substitution, although more quantitative Fe# estimates based on shifts in each of these two major peaks disagreed, so a range of Fe#s are reported here (Table 3.7).

Estimated Fe-content in PDE1 mainly exceeded Fe-content determined with EMP and EDS, and Fe#s for TuN5 and PDE3 entirely exceeded quantitative and semiquantitative values. Fe#s in Ttop6 natroalunites, on the other hand, agreed with Fe#s determined with EMP and EDS.

Although no EMP or EDS analyses of Ttop2 and PF9 natroalunite grains were successful, Fe# estimates from XRD peak shifts were $\sim 20-30$ and $\sim 15-25$ for Ttop2 and PF9, respectively. The Fe# ranges of Ttop2 and Ttop6 natroalunites roughly agree with Fe-content estimated from Raman peak shifts, which may mean that *in situ* methods can succeed at evaluating approximate Fe#. As XRD peak shifts was the only method that provided insight into Fe-content in PF9, Fe# estimates of PF9 natroalunites may be unreliable.

3.6 Discussion

3.6.1 Iron Substitution in Natroalunite in Costa Rica

We identified Fe-rich natroalunite in four of the six representative samples from acid sulfate alteration sites in Costa Rica. Findings with EMP and SEM-EDS indicate relatively minor iron substitution (generally $Fe\# < 15$) in natroalunite at Poás and Turrialba. One sample, Ttop6, had a higher Fe# (up to $Fe\# \sim 33$ with EMP), significantly outside literature natroalunite composition. However, EMP analyses may not have been fully quantitative due to Na and K loss with beam damage, intermixing of natroalunite with silica, hematite spherules on grain surfaces, or other factors. EDS measurements are usually considered semiquantitative, but as $Fe\#$ s obtained with EMP and EDS analyses generally agreed for TuN5, Ttop6, and some PDE1 and PDE3 grains, these methods most likely represent Fe-content in these samples.

Fe-content in these Costa Rican samples is similar to that in samples from Nicaragua, particularly natroalunite from Cerro Negro volcano with $Fe\#s < 20$ [McCollom *et al.*, 2013a, 2014]. McCollom *et al.* [2013b, 2014] also identified higher Fe-content ($Fe\# \sim 25-40$) and greater ranges of Fe-content in some samples from Telica and Masaya volcanoes, comparable to Fe-content in Ttop and PDE samples from Costa Rica. The range of $Fe\#$ s both within and between grains suggests micron or even sub-micron processes are causing Fe-substitution in some natroalunite grains studied here.

3.6.2 X-ray Diffraction and Raman Spectroscopy Characterization of Fe-rich Natroalunite

Instruments available on current and upcoming rovers for *in situ* mineralogy are primarily CheMin, the x-ray diffraction (XRD) instrument on Curiosity [Blake *et al.*, 2012], and the Raman laser spectrometers onboard the upcoming ESA ExoMars rover [Rull *et al.*, 2011] and NASA 2020 rover [Beegle *et al.*, 2014]. We therefore evaluated the feasibility of detecting and quantifying Fe-substitution in naturally occurring natroalunites with Raman and XRD for applicability to Mars. We noted peak shifts in Raman spectra of five samples and in XRD

patterns of all six samples indicative of Fe-substitution, based on comparison to standards synthesized by *McCollom et al.* [2014]. However, attempts to quantify Fe-content from peak shifts proved difficult, as Fe# estimates varied based on which peak shift was investigated. Consequently, a range of possible Fe#s is reported for each sample, with standard deviations of ~2.5 to 4 with XRD and ~2 to 13 with Raman.

Estimated ranges of Fe-substitution from Raman and XRD peak shifting generally either encompassed or exceeded quantitative measurements from four of the six samples (Tables 3.3, 3.6, and 3.7). EMP and EDS analyses were not possible in Ttop2 or PF9 due to natroalunite intermixing with silica and hematite; however, estimates of Fe-content in Ttop2 from XRD and Raman peak shifting mainly agreed with each other (Tables 3.6 and 3.7). Of the four methods used to detect and estimate Fe-content, only XRD peak shifts indicated the presence of Fe-rich natroalunite in PF9. As XRD peak shifting mainly overestimated Fe-content in other samples, we consider this a tentative detection of Fe-rich natroalunite in PF9. Overall, the general consensus of these methods indicate that Raman and XRD peak shifts can be used with caution to detect Fe-rich natroalunites *in situ*.

Discrepancies between quantitative Fe# measurements and estimates from XRD and Raman peak shifts could be due to complications from silica intermixing (e.g. Ttop2), hematite spherules on grain surfaces (e.g. PF9 and Ttop6), or Ca- and K-substitution for Na (e.g. TuN5 and PDE3). However, hematite and silica peaks in Raman spectra and XRD patterns do not overlap with those of natroalunite, and therefore should not affect natroalunite peak positions. Although minor Ca was detected in TuN5, Ttop6, PDE1, and PDE3 natroalunites (Tables 3.2 and 3.4), insufficient Ca was present to qualify as literature natroalunite-2c, which suggests minimal Ca contribution to peak shifts. Furthermore, d-spacing correlated with the highest intensity peaks ($\sim 18^\circ$ and 30° 2θ) in natroalunite and natroalunite-2c differs by $\leq 0.01^\circ 2\theta$ and therefore could not be distinguished with the Terra XRD instrument. K substitution could cause peak shifts toward lower 2θ by $\geq 0.2^\circ 2\theta$, but $< 1\%$ K was present in samples. Consequently, the

minor amount of Ca and K in these natroalunites likely did not cause peak shifts that could interfere with those related to Fe-content.

Major discrepancies between Fe# estimates for PDE1 from XRD- and Raman-peak shifts and from quantitative methods were observed. This inconsistencies could have resulted from overlapping of natroalunite and jarosite peaks, or could reflect more intermediate compositions between endmember natroalunite and jarosite in PDE1 than observed with either EMP or EDS. As jarosite and natroalunite peaks were clearly distinguishable in both XRD patterns and Raman spectra of PDE1, and only natroalunite peaks were used to estimate Fe#s with these methods, the presence of more Fe-rich natroalunite is a more likely explanation than issues with peak overlap. However, micron-scale variation in Fe# within and between grains of the same sample could complicate peak shifting through unknown mechanisms.

Regardless, further work to refine the calibration of peak shifting in natural Fe-rich natroalunite is likely needed. Recent work on Raman peak shifting due to *A* site substitutions in jarosite [Ling *et al.*, 2016] could be replicated for alunite solid solutions and evaluated with both XRD and Raman spectroscopy. Natroalunite solid solutions with both *A* and *B* site substitutions could also be synthesized and analyzed with Raman and XRD to improve calibrations of Fe-related peak shifting. Evaluating shifts in additional minor XRD peaks (e.g. peaks at ~ 15.5 , 25.5 , 39.5 , 48 , and $52.5^\circ 2\theta$) could also further constrain Fe# estimates from XRD.

3.6.2.1 Applying Raman Spectroscopy for Fe-rich Natroalunite Detection *In situ*

3.6.2.1.1 ExoMars Raman Laser Spectrometer (RLS)

The green laser (532 nm) of the Horiba LabRAM HR Raman spectrometer used in this study was operated in the range of ~ 100 to ~ 1700 cm^{-1} and has a spectral resolution of < 1 cm^{-1} . In comparison, the ExoMars Raman Laser Spectrometer (RLS) will use a 531.5 nm laser in the range of ~ 150 to 3800 cm^{-1} with an intended spectral resolution of ~ 6 cm^{-1} below 2000 cm^{-1} [Rull *et al.*, 2011]. At $\text{Fe}\# < 25$, peaks at ~ 230 and ~ 1020 cm^{-1} shift by less than < 6 cm^{-1} and would be undetectable with the RLS. Although the peak at ~ 390 cm^{-1} could hypothetically be

used, basing an estimate of Fe-content off a single peak is suspect. Other prominent fingerprint peaks, such as the ν_2 band at $\sim 480\text{ cm}^{-1}$ and ν_4 band at $\sim 650\text{ cm}^{-1}$, were considered for this study, but clear shifts in these peaks at low Fe#s were difficult to discern; the peak at $\sim 480\text{ cm}^{-1}$ is a fairly broad doublet at low Fe-content, and shifts in the peak at $\sim 650\text{ cm}^{-1}$ with increasing Fe# follows a less linear pattern than do other peaks. Therefore more than 25% Fe-substitution is likely necessary for the ExoMars RLS to detect Fe-rich natroalunite *in situ*. Considering the wide range of possible Fe#s in these natroalunite samples based on Raman peak shifts, estimating Fe content *in situ* would be difficult.

This fall, the ExoMars descent module *Schiaparelli* will land in Meridiani Planum, where the Opportunity rover discovered jarosite in 2004 [Klingelhöfer *et al.*, 2004; Silvestro *et al.*, 2015]. However, *Schiaparelli* is a technological demonstration with limited analytical capability. The landing site of the ExoMars rover, set to launch in 2020, is yet to be determined. Were the rover to join *Schiaparelli* in Meridiani Planum, the RLS could be used to assess Opportunity's Mössbauer detection of jarosite in the region.

3.6.2.1.2 Mars 2020 Scanning Habitable Environments With Raman & Luminescence for Organics & Chemicals (SHERLOC) instrument

The primary goal of SHERLOC on the Mars 2020 rover is the detection of aromatic and aliphatic organic compounds. SHERLOC will use a deep-UV laser (248.6 nm) in the range of 800 to 4000 cm^{-1} [Beegle and Bhartia, press conference]. As detection of aqueously derived minerals is only a secondary objective, both the operation and objectives of SHERLOC differ from that of the Horiba Raman spectrometer used in this study. The Mars 2020 rover will also be equipped with SuperCam, an integrated instrument comprised of a Laser-Induced Breakdown Spectrometer, Raman spectrometer, time-resolved fluorescence spectrometer, visible and infrared (VISIR) reflectance spectrometer, and remote micro-imager, designed primarily for mineralogical assessments. SuperCam will use a 532 nm laser down to 200 cm^{-1} from a distance of 12 m from the sample.

Landing site selection for the Mars 2020 rover landing site is currently in progress, with eight possible locations under consideration. Jarosite and alunite have been detected with CRISM at two of these sites, Mawrth Vallis [Farrand *et al.*, 2009] and Northeast Syrtis Major [Ehlmann and Mustard, 2012], and could potentially exist within the sulfate and iron oxide mineral assemblages studied by Spirit *in situ* at Gusev Crater and via CRISM at Melas Chasma [Arvidson *et al.*, 2008; Yen *et al.*, 2008; Murchie *et al.*, 2009]. If one of these sites is chosen, SHERLOC may have the opportunity to study alunite-jarosite minerals; however, the instrument's design and purpose make this a remote possibility.

3.6.2.2 Applying XRD for Fe-rich Natroalunite Detection *In situ*

Both CheMin and the analog Terra XRD instrument operate from ~ 5 to $55^\circ 2\theta$, however CheMin has a $<0.35^\circ 2\theta$ resolution and a detection limit of 3 wt% [Blake *et al.*, 2012] while the Terra instrument was designed to have a resolution of $\sim 0.05^\circ 2\theta$ and detection limit of 1 wt% [Treiman *et al.*, 2010]. As peak locations of McCollom *et al.* [2014] standards differ by $\leq 0.35^\circ 2\theta$ between Fe#0 and Fe#25, detection of Fe-rich natroalunite with XRD, as with Raman, requires $>25\%$ Fe-content. Although XRD-based estimates of Fe-content were more narrow in range than were Raman-based estimates, using CheMin XRD peak shifts for estimating the amount of Fe-substitution in natroalunite is likely not feasible at low Fe#s *in situ*.

Following a tentative jarosite detection in the Windjana sample at Kimberley [Treiman *et al.*, 2016], jarosite was detected in the basal member of the Murray Formation at the base of Mt. Sharp [Cavanagh *et al.*, 2015; Rampe *et al.*, 2015, 2016]. Jarosite is at or near detection limits in Confidence Hills (CH), more abundant less than a meter above in Mojave 2 (MJ), and present in trace amounts roughly 6 meters up section from MJ at Telegraph Peak (TP) [Cavanagh *et al.*, 2015; Rampe *et al.*, 2015, 2016]. These detections at the base of Mt. Sharp could herald the discovery of more alunite-jarosite group minerals along Curiosity's traverse and therefore provide opportunities to identify intermediate members with XRD peak shifts of $\geq 0.35^\circ 2\theta$.

3.6.3 Partial Dissolution of Fe-rich Natroalunite to Form Hematite Spherules

Hematite was identified in diffraction patterns and Raman spectra in PF9 and Ttop6 (Table 3.2, Figure 3.5), and backscattered electron images and Raman images revealed that the hematite is present as spherules, $\leq 2 \mu\text{m}$ in diameter, on natroalunite grain surfaces (Figures 3.6b, 3.7, 3.8, and 3.10). The co-occurrence of jarosite and hematite spherules was also observed at Meridiani Planum [*Klingelhöfer et al.*, 2004], where millimeter-sized hematite concretions informally called “blueberries” were found in loose soil and jarosite-rich outcrops. Geochemical models and experimental work into jarosite stability predict that at $\text{pH} > 3.5$ in water-limited conditions, jarosite dissolution produces sub-micron maghemite and hematite that can aggregate into larger concretions; this process may have formed the “blueberries” at Meridiani Planum [*Elwood Madden et al.*, 2004, 2012]. The co-occurrence of natroalunite and micron-sized hematite spherules in PF9 and Ttop6 could be indicative of a similar dissolution pathway in Fe-rich natroalunite subjected to water-limited conditions. If exposed to prolonged acid sulfate alteration conditions, these hematite spherules could also aggregate into micron-sized “blueberries.” Consequently, PF9 and Ttop6 may have initially had significant Fe-rich natroalunite subsequently weathered to produce abundant hematite spherules in association with natroalunite.

Hematite was detected at or near detection limits in Rocknest [*Bish et al.*, 2013], John Klein and Cumberland [*Vaniman et al.*, 2014], and alongside trace amounts of jarosite in Windjana [*Treiman et al.*, 2016]. In the basal member of the Murray Formation, CH has jarosite near the detection limit and $\sim 8 \text{ wt}\%$ hematite, while a meter above, MJ contains more jarosite and less hematite [*Cavanagh et al.*, 2015; *Rampe et al.*, 2015, 2016]. This may be indicative of greater jarosite dissolution moving down section due to persistence of aqueous conditions and acid sulfate alteration processes lower in the formation.

3.7 Implications for Mars

We found that Fe-substitution in natroalunite is not limited to acid sulfate alteration sites in Nicaragua. Fe-rich natroalunite formed from a variety of parent lithologies in a range of geochemical settings (pH ~1.5 to 5, temperature up to ~100°C) at Poás and Turrialba. The six samples in this study are only a subset of more than 30 samples that contain natroalunite. As natroalunite was a major mineral across sites with temperatures from ~16°C to 180°C and pH <1 to 5, the range of geochemical conditions conducive to Fe-substitution in natroalunite may be more expansive than reported here. In comparison, natroalunite was a minor phase at acid sulfate alteration sites in Nicaragua [Hynek *et al.*, 2013; McCollom *et al.*, 2013a].

The presence of hematite spherules on natroalunite from active fumaroles at Poás and Turrialba further constrains pH and aqueous conditions during the formation of these mineral assemblages. Early diagenesis of Ttop6 and PF9 samples initiated Fe-rich natroalunite dissolution, which was arrested either by a change in water availability, or by the removal of samples during fieldwork. Incomplete weathering of jarosite to hematite also likely occurred in the Murray Formation at the base of Mt. Sharp [Rampe *et al.*, 2015, 2016].

This work may directly apply to sites on Mars where jarosite has been identified, particularly in the Murray Formation at Gale Crater [Cavanagh *et al.*, 2015; Treiman *et al.*, 2016], Mawrth Valles [Farrand *et al.*, 2009], Noctis Labyrinthus [Weitz *et al.*, 2011; Thollot *et al.*, 2012], Northeast Syrtis Major [Ehlmann and Mustard, 2012], and Meridiani Planum [Klingelhöfer *et al.*, 2004], as well to sites with alunite deposits, such as Cross Crater [Ehlmann *et al.*, 2016] and Columbus Crater [Wray *et al.*, 2011] in Terra Sirenum. Although peaks in X-ray diffraction patterns or Raman spectra obtained via rover instruments likely cannot provide quantitative estimates of Fe-content, these methods could detect significant ($\geq 25\%$) Fe-substitution in natroalunite *in situ*. Distinguishing Fe-rich natroalunite from jarosite *in situ* on Mars would provide additional constraints on the planet's early geochemistry and habitability.

CHAPTER 4: CONCLUSIONS

This thesis contributes to the characterization of mineralogy at Mars analog sites to aid with the interpretation of similar mineral assemblages on Mars. Chapter 1 introduced the relevant background information, including the history of the search for life on Mars, the geology of Mars, the mineralogic evidence for water on Mars, and the purpose of studying Mars analog sites. Chapters 2 and 3 were written for upcoming submission to peer-reviewed journals. Chapter 2 investigated the capability of the Mars Science Laboratory rover Curiosity to detect clays *in situ* with x-ray diffraction (XRD). Chapter 3 evaluated the iron content of natroalunite from Costa Rican hydrothermal systems and determined whether iron-rich natroalunite could be distinguished from jarosite *in situ* on Mars. The findings and implications of this work are summarized below.

4.1 Characterization of the Mineral Assemblage at Poás and Turrialba Volcanoes, Costa Rica

4.1.1 Motivation

Geochemical parameters such as temperature, pH, water:rock ratios, and parent lithology determine how and which alteration minerals will form at a particular site. By characterizing mineral assemblages produced through specific alteration pathways, the geochemical processes that formed similar mineral assemblages on Mars can be constrained. This in turn enables better interpretations of early Mars' habitability.

Acid sulfate alteration processes occurring at Poás and Turrialba volcanoes in Costa Rica are analogous to those that occurred on early Mars. To characterize these new terrestrial analogs for Mars, samples were collected from a variety of geochemical environments at each volcano in November 2013. Sampling sites ranged from active fumaroles to outwash basins near crater lakes, and temperatures and pH during field work ranged from ~16°C to 180°C and

<1 to 5, respectively. A total of 57 samples, primarily loose sediments and hand samples, were collected. To characterize the mineralogy at Poás and Turrialba, I analyzed this sample suite with XRD.

4.1.2 Findings

The major alteration minerals at Poás and Turrialba are cristobalite, amorphous silica, natroalunite, gypsum and anhydrite, iron and titanium oxides, tridymite, and sulfur. Minor alteration phases include jarosite and polyhydrated sulfates like sodium alum, mirabilite, and alunogen.

Samples for the projects described in Chapters 2 and 3 were selected from this suite of 57 samples. Based on these studies, the results of which are summarized below in sections 4.2 and 4.3, the mineral assemblages at these sites also include kaolinite and iron-rich natroalunite. Further characterization of this sample suite with additional instrumentation can be found in *Black et al.* [2016] and *Black et al.* [in prep.].

4.1.3 Implications

The mineral assemblages at Poás and Turrialba are similar to those identified at putative relict hydrothermal sites on Mars, including Noctis Labyrinthus [*Weitz et al.*, 2011; *Thollot et al.*, 2012], Northeastern Syrtis Major [*Ehlmann and Mustard*, 2012], Mawrth Valles [*Farrand et al.*, 2009], and Terra Sirenum [*Wray et al.*, 2011; *Ehlmann et al.*, 2016]. Hydrothermal acid sulfate alteration like that occurring at Poás and Turrialba may have also formed these mineral assemblages on Mars. Further characterization of the alteration mineralogy at Poás and Turrialba will provide additional insight into the geochemical conditions in which these mineral assemblages form.

4.2 Detection and Characterization of Clays with XRD

4.2.1 Motivation

Clays on Mars (and Earth) require an aqueous environment to form, whether it be a lacustrine, fluvial, or hydrothermal groundwater system [Eberl *et al.*, 1984]. The ability to detect clays is therefore crucial to uncovering evidence of water on early Mars. Identifying the clays within a particular mineral assemblage constrains the possible water:rock ratios, pH, redox conditions, temperature, and pressure at the time of formation [Eberl *et al.*, 1984; Ehlmann *et al.*, 2011].

XRD is a valuable tool for characterizing mineral assemblages. The Curiosity rover is equipped with CheMin, the first XRD instrument on Mars, for *in situ* mineralogy analyses at Gale Crater [Blake *et al.*, 2012]. CheMin is limited, however, by the physical and technological constraints of placing an instrument on another planet. By evaluating the effects of isolating and orienting clays for analysis with a CheMin analog instrument, I sought to determine whether CheMin can detect all clays in a mineral assemblage without additional sample preparation prior to XRD analyses.

4.2.2 Findings

Removing non-clay minerals, performing particle size separation (<2 μm), and preferentially orienting samples significantly improved the detection and identification of clays with XRD. Of the 14 samples of acid sulfate altered basalt selected for this study, kaolinite was identified in four samples, one of which also contained montmorillonite. Tentative clay detections with a traditional laboratory XRD instrument in two samples were identified as kaolinite after clay isolation. Kaolinite was not detected either before or after the clay isolation procedure with the CheMin analog instrument in these samples.

Although the clay isolation procedure improved clay detection, it was not entirely successful in removing non-clay minerals, particularly sulfates. Only one sample was free of all non-clay minerals after the procedure. However, the intensities of clay XRD peaks increased

relative to non-clay peaks following the procedure, which greatly aided clay detection and characterization.

4.2.3 Implications

4.2.3.1 *In situ* Clay Detections with XRD

None of the steps used in this study to isolate clays are currently feasible on Mars. Were it possible to conduct this procedure *in situ*, the removal of the sulfates, iron oxides, cristobalite, tridymite, and hydrated silica identified in samples at Gale Crater [Vaniman *et al.*, 2014; Cavanagh *et al.*, 2015; Rampe *et al.*, 2015, 2016] would eliminate any peaks masking clay peaks in XRD patterns. Ethylene glycol solvation in particular would improve identification of the ambiguous Fe,Mg smectite identified at Yellowknife Bay [Vaniman *et al.*, 2014; Bristow *et al.*, 2015] and in the Kimberley Formation [Treiman *et al.*, 2016], as it would create consistent interlayer spacing in smectites from all samples.

By comparison to the Terra XRD instrument, the CheMin analog used in this study, CheMin may be failing to detect clays at Gale Crater without additional sample preparation before XRD analyses. As the Terra XRD was designed with a 1 wt% detection limit [Treiman *et al.*, 2010], and CheMin has a detection limit of 3 wt% [Blake *et al.*, 2012], CheMin is even further limited in its ability to detect clays.

4.2.3.2 Interpreting Mineral Assemblages on Mars

Clays were detected in samples from active fumaroles, the edge of an ambient crater lake above the shoreline, and an outwash basin frequently inundated with highly acidic (pH~0.3) lake water and wet hot pyroclastics. In addition to clays, the mineral assemblages at these sites included natroalunite, cristobalite, calcium sulfates, iron oxides, anatase, and amorphous silica produced from incompletely weathered basalt (see section 4.1.2) and are similar to those identified at multiple sites on Mars. The coeval formation of clays, sulfates, iron oxides, and hydrated silica at Poás and Turrialba suggests that the formation of similar mineral

assemblages on Mars does not require the global climate change from neutral to acidic conditions often invoked to explain these varied mineral assemblages [Bibring *et al.*, 2006].

Analysis of the mineral assemblage at the fluvial outwash basin at Poás is especially relevant to characterization and interpretation of the basal member of the Murray Formation in Gale Crater. A mineral assemblage including phyllosilicates, amorphous silica, cristobalite, tridymite, alunite-jarosite group minerals, hematite, magnetite, and primary basaltic minerals is found at both sites [Cavanagh *et al.*, 2015; Rampe *et al.*, 2015, 2016; Morris *et al.*, 2016]. At Poás, this assemblage forms through transport of primary igneous material and minerals produced by water-limited acid fumarolic weathering from the surrounding dome edge, crater walls, and rim to the edge of the crater lake, where further alteration and input occurs when the outwash basin is inundated by pyroclastics or acid sulfate lake water. A similar pathway may be responsible for the mineral assemblage in the lower members of the Murray Formation.

Phyllosilicates were not detected farther up-section in the Murray Formation [Rampe *et al.*, 2015, 2016; Morris *et al.*, 2016]. This absence could be due to changes in the depositional environment or to diagenesis, the preferred interpretations of the MSL Team. Alternatively, phyllosilicates may be present in the upper member of the Murray Formation, but CheMin is unable to detect these minerals without additional clay isolation techniques. The presence of phyllosilicates throughout the Murray Formation, even at low abundances, would alter interpretations of the formation of this mineral assemblage.

4.3 Iron Substitution in Natroalunite at Costa Rica

4.3.1 Motivation

The Mars Exploration Rover Opportunity detected jarosite ($\text{KFe}_3(\text{SO}_4)_2(\text{OH})_6$) at Meridiani Planum [Klingelhöfer *et al.*, 2004], and Curiosity has recently detected jarosite in the Murray Formation at Gale Crater [Cavanagh *et al.*, 2015; Rampe *et al.*, 2015, 2016]. The presence of alunite-jarosite group minerals on Mars is indicative of acid sulfate alteration

processes. However, alunite ($\text{KAl}_3(\text{SO}_4)_2(\text{OH})_6$) can form in a broader range of pH, water:rock ratios, and redox conditions than can jarosite. Therefore, by distinguishing between minerals within this family, additional constraints can be placed on the acid sulfate alteration pathway that produced a particular mineral assemblage.

The recent discovery of naturally occurring iron-rich natroalunite ($\text{Na}(\text{Al,Fe})_3(\text{SO}_4)_2(\text{OH})_6$) in Nicaragua [McCollom *et al.*, 2013a] raised the question of whether this intermediate member of the alunite-jarosite group exists on Mars, and what its presence would mean for interpretations of early Mars' geochemical processes. This study aimed to determine if iron-rich natroalunite is unique to acid sulfate alteration processes in Nicaragua, and whether this mineral could be distinguished from jarosite using methods available to current and upcoming *in situ* Mars missions.

4.3.2 Findings

Iron-rich natroalunite was detected in four of six samples of acid sulfate altered basalt from Costa Rica with Electron Microprobe (EMP) analyses and Scanning Electron Microscopy (SEM). Overall, iron substitution for aluminum was usually <15%, but iron content ranged from no detectable iron in some grains up to 33% iron substitution in other grains, even within the same hand sample. Variations in iron content, usually seen as compositional zoning with aluminum-rich interiors and iron-rich rims, also occurred within natroalunite grains. Natroalunite in some samples had hematite spherules $\leq 2 \mu\text{m}$ in diameter on grain surfaces, but this did not prevent reliable EMP or SEM analyses in one of these samples. In two samples, however, reliable analyses were not feasible due to interbedding of natroalunite with silica and/or an extensive coating of hematite spherules. These findings generally agree with those for iron-rich natroalunite from Nicaraguan analogs for Mars [McCollom *et al.*, 2013a, 2014]. Iron content in natroalunite at Costa Rica is similar to amounts reported from Nicaragua, and some natroalunite grains from both sites display compositional zoning or coating with iron oxide/hydroxides [McCollom *et al.*, 2013a, 2014].

Whether Curiosity and the upcoming ESA ExoMars and NASA 2020 rovers will be able to distinguish between iron-rich natroalunite and jarosite *in situ* was also assessed. Curiosity is equipped with CheMin for XRD and the ESA ExoMars and NASA 2020 rovers will be equipped with Raman spectrometers. Peak shifts in XRD patterns and in the fingerprint region of Raman spectra of natroalunite caused by iron substitution were evaluated. Ranges of estimated iron content in natroalunite with XRD and Raman peak shifts were broad, with large standard deviations, and usually either encompassed or exceeded measurements made with EMP or SEM. In the two samples for which reliable EMP or SEM analyses were not feasible, ~10-30% iron substitution is present based on XRD and Raman peak shifts. However, without the ability to “ground-truth” these estimates with EMP or SEM, these estimates should be treated with caution.

4.3.3 Implications

4.3.3.1 Iron Content in Natroalunite in Costa Rica

Of six representative samples chosen for this study, iron substitution of >5% occurred in three based on quantitative or semiquantitative methods (EMP and SEM). Variations in iron distribution between and within grains were present at a micron or submicron scale and are indicative of highly localized processes responsible for the incorporation of iron into natroalunite in these samples. These samples are a subset of more than 30 containing natroalunite at Poás and Turrialba, therefore further measurements of iron content in natroalunite at these sites may reveal that iron-rich natroalunite is a major alteration mineral at Costa Rica.

4.3.3.2 *In situ* Detection of Iron-rich Natroalunite

Although wide ranges of possible iron content were estimated with XRD and Raman peak shifts, these methods successfully identified iron-rich natroalunite in samples. Based on the intended spectral resolution ($\sim 6 \text{ cm}^{-1}$) for the Raman spectrometer on ExoMars [Rull *et al.*, 2011] and the resolution ($< 0.35^\circ 2\theta$) of CheMin [Blake *et al.*, 2012], $\geq 25\%$ iron substitution in natroalunite is required for Curiosity and ExoMars instrumentation to distinguish between

jarosite and iron-rich natroalunite *in situ*. As the Raman spectrometer on the upcoming NASA 2020 rover operates in a different spectral range and is primarily intended for detection and analysis of organic molecules, this instrument likely will not be able to distinguish between jarosite and iron-rich natroalunite.

4.3.3.3 Interpreting Jarosite- and Hematite-Rich Outcrops at Meridiani Planum

Opportunity's discovery of jarosite at Meridiani Planum was made with Mössbauer spectroscopy [*Klingelhöfer et al.*, 2004]. Hematite was also found in association with jarosite as millimeter-sized concretions referred to as "blueberries." These "blueberries" may have formed through the dissolution of jarosite at $\text{pH} > 3.5$ in water-limited conditions, which produces sub-micron maghemite and hematite that can aggregate into larger concretions [*Elwood Madden et al.*, 2004, 2012]. The presence of micron-sized hematite spherules on some natroalunite grains from Costa Rica and Nicaragua suggests that iron-rich natroalunite undergoes a similar dissolution process to jarosite but not necessarily at $\text{pH} > 3.5$, as evidenced from the field measurements. As Mössbauer spectroscopy cannot distinguish between jarosite and iron-rich natroalunite [*McCollom et al.*, 2014], some or all of the jarosite detected by Opportunity could be iron-rich natroalunite undergoing alteration to form hematite.

4.3.3.4 Interpreting the Murray Formation at Gale Crater

Curiosity recently detected jarosite and hematite in the Murray Formation with CheMin. The similarity of the mineral assemblage in the basal member of the Murray Formation to the mineralogy at Poás, as discussed in section 4.2.3, suggests that Curiosity could find iron-rich natroalunite during its ongoing traverse over stratigraphically higher members of the Murray Formation.

4.4 Implications for Astrobiology

Hynek et al. [in prep.] is currently conducting the first investigation into the microbial ecology at Poás and Turrialba volcanoes. Preliminary work has revealed a single genus

(*Acidiphilium*) of Alphaproteobacteria from lake water collected in November 2013 [*Hynek et al.* in prep.]. Even with the extreme pH (0.3) and continuous volcanic activity (~60 phreatic eruptions through the crater lake occurred the following year), microorganisms persist. Alunite and jarosite deposits on Mars likely formed in more habitable fluids at higher, albeit still acidic, pH.

Further work across different geochemical settings at Poás and Turrialba may reveal that these hydrothermal systems are populated by similar microbial communities to those characterized at similar sites. For example, at Solfatara Crater in Italy, from which the term for a sulfurous fumarole like those at Poás and Turrialba originates, a diverse bacterial community was found [*Glamoclija et al.*, 2004]. Work at Cerro Negro, Nicaragua, where iron-rich natroalunite was first discovered [*McCollom et al.*, 2013a], has revealed photosynthetic communities within silica crusts on fumaroles [*Rogers et al.*, 2011, 2013]. Archaea were found within the highly acidic Kawah Ijen crater lake in Indonesia, which has the same pH (~0.3) as the Poás crater lake [*Löhr et al.*, 2006]. Based on preliminary sequencing efforts and comparison to sites with similar acid sulfate alteration processes, Poás and Turrialba likely provide plenty of habitable niches for extremophiles. Further characterization of the microbial diversity at Turrialba and Poás, particularly in the Poás fluvial outwash basin, could provide insight into the microorganisms that could survive in analogous systems on early Mars, including at Gale Crater.

4.5 Recommendations for Future Work

4.5.1 Further Characterization of Poás and Turrialba as Mars Analog Sites

Characterization of the full sample suite from Poás and Turrialba with XRD, Raman spectroscopy, x-ray fluorescence (XRF), and visible/near-infrared spectroscopy (VNIR) are described by *Black et al.* [2016] and *Black et al.* [in prep.]. Evaluation of iron content in natroalunite from additional samples in this suite could determine the extent and range of iron-rich natroalunite at Poás and Turrialba.

Another field campaign to Poás and Turrialba is planned for fall 2016 for a more thorough analysis of the mineralogy and geochemical conditions. Further study of these sites, and of the fluvial outwash basin at Poás in particular, will enable better interpretations of the Murray Formation at Gale Crater. In addition, ongoing work to characterize the microbiology across different geochemical settings at Poás and Turrialba will not only reveal the microbial ecology of these Mars analog sites, but also allow inferences of the habitability of Gale Crater and other sites on Mars.

4.5.2 Clay Detection with XRD at Mars Analog Sites

The removal of non-clay minerals in this study was primarily based on methods developed for removing gypsum and anhydrite from evaporites [*Bodine and Fernald, 1973*]. However, additional sulfates, including natroalunite, jarosite, and alunogen, were present in these samples of acid sulfate altered basalt, and in most cases these minerals were not removed with this procedure. No work to date has developed clay isolation techniques specific to acid sulfate alteration mineral assemblages, which have been detected at numerous sites on Mars [e.g., *Klingelhöfer et al., 2004; Yen et al., 2008; Weitz et al., 2011; Ehlmann and Mustard, 2012*]. Although not feasible on Mars, isolating clays from samples at Mars analog sites for XRD analyses would produce a more complete picture of the mineral assemblages at these sites, which could enable better interpretations of similar mineral assemblages on Mars.

REFERENCES

- Acuna, M. H. et al. (1999), Global distribution of crustal magnetization discovered by the Mars global surveyor MAG/ER experiment, *Science*, 284(5415), 790–793.
- Agee, C. B. et al. (2013), Unique meteorite from early Amazonian Mars: water-rich basaltic breccia Northwest Africa 7034, *Science*, 339(6121), 780–785.
- Albee, A. L., R. E. Arvidson, F. Palluconi, and T. Thorpe (2001), Overview of the Mars Global Surveyor mission, *Journal of Geophysical Research*, 106(E10), 23291–23316.
- Amils, R. et al. (2007), Extreme environments as Mars terrestrial analogs: The Rio Tinto case, *Planet. Space Sci.*, 55(3), 370–381.
- Amundsen, H. E. F., F. Westall, A. Steele, J. Vago, and N. Schmitz (2010), Integrated Exomars PanCam, Raman, and close-up imaging field tests on AMASE 2009, *EGU General Assembly*.
- Anders, E. (1996), Evaluating the evidence for past life on Mars, *Science*, 274(5295), 2119–21; author reply 2122–5.
- Andrews-Hanna, J. C., and R. J. Phillips (2007), Hydrological modeling of outflow channels and chaos regions on Mars, *Journal of Geophysical Research*, 112(E8).
- Archer, P. D. et al. (2014), Abundances and implications of volatile-bearing species from evolved gas analysis of the Rocknest aeolian deposit, Gale Crater, Mars, *Journal of Geophysical Research: Planets*, 119, 237–254.
- Arvidson, R. E., F. Poulet, J.-P. Bibring, M. Wolff, A. Gendrin, R. V. Morris, J. J. Freeman, Y. Langevin, N. Mangold, and G. Bellucci (2005), Spectral reflectance and morphologic correlations in eastern Terra Meridiani, Mars, *Science*, 307(5715), 1591–1594.
- Arvidson, R. E. et al. (2008), Spirit Mars Rover Mission to the Columbia Hills, Gusev Crater: Mission overview and selected results from the Cumberland Ridge to Home Plate, *Journal of Geophysical Research*, 113(E12), doi:10.1029/2008JE003183.
- Arvidson, R. E. et al. (2010), Spirit Mars Rover Mission: Overview and selected results from the northern Home Plate Winter Haven to the side of Scamander crater, *Journal of Geophysical Research*, 115(E00F03), doi:10.1029/2010JE003633.
- Arvidson, R. E. et al. (2014), Ancient aqueous environments at Endeavour crater, Mars, *Science*, 343(6169), 1248097.
- Arvidson, R. E. et al. (2016), High concentrations of manganese and sulfur in deposits on Murray Ridge, Endeavour Crater, Mars, *American Mineralogist*, 101(6), 1389–1405.
- Aubrey, A., H. J. Cleaves, J. H. Chalmers, A. M. Skelley, R. A. Mathies, F. J. Grunthaner, P. Ehrenfreund, and J. L. Bada (2006), Sulfate minerals and organic compounds on Mars, *Geology*, 34(5), 357–360.
- Azua-Bustos, A., C. Urrejola, and R. Vicuña (2012), Life at the dry edge: microorganisms of the

- Atacama Desert, *FEBS Letters*, 586(18), 2939–2945.
- Balta, J. B., and H. Y. McSween (2013), Water and the composition of Martian magmas, *Geology*, 41(10), 1115–1118.
- Bandfield, J. L. (2000), A Global View of Martian Surface Compositions from MGS-TES, *Science*, 287(5458), 1626–1630.
- Bandfield, J. L. (2002), Global mineral distributions on Mars, *Journal of Geophysical Research*, 107(E6, 5042).
- Banin, A., F. X. Hah, I. Kan, and A. Cieelsky (1997), Acidic volatiles and the Mars Soil, *Journal of Geophysical Research*, 102(E6), 13341–13356.
- Beegle, L. W. et al. (2014), SHERLOC: Scanning Habitable Environments With Raman & Luminescence for Organics & Chemicals, an Investigation for 2020, *AGU Fall Meeting*.
- Bell, J. F. (1996), Evaluating the evidence for past life on Mars, *Science*, 274(5295), 2121–2; author reply 2122–3.
- Benison, K. C., and B. B. Bowen (2006), Acid saline lake systems give clues about past environments and the search for life on Mars, *Icarus*, 183(1), 225–229.
- Bibring, J.-P., and S. Erard (2001), The martian surface composition, *Space Science Reviews*, 96(February), 293–316.
- Bibring, J.-P. et al. (2005), Mars surface diversity as revealed by the OMEGA/Mars Express observations, *Science*, 307(5715), 1576–1581.
- Bibring, J.-P. et al. (2006), Global mineralogical and aqueous mars history derived from OMEGA/Mars Express data, *Science*, 312(5772), 400–404.
- Biemann, K. et al. (1976), Search for organic and volatile inorganic compounds in two surface samples from the chryse planitia region of Mars, *Science*, 194(4260), 72–76.
- Bish, D. L. et al. (2013), X-ray diffraction results from Mars Science Laboratory: mineralogy of Rocknest at Gale crater, *Science*, 341(6153), 1238932.
- Black, S. R., B. M. Hynek, and G. E. Alvarado (2015), Spectral identification of acid sulfate alteration products in Costa Rica Volcanoes: Implications early Mars, *46th Lunar and Planetary Science Conference*, (Abstract 2260).
- Black, S. R., B. M. Hynek, R. Hoover, L. G. Beckerman, and G. E. Alvarado (2016), Characterization of Hydrothermal Alteration in Costa Rica: Mineralogy, Methodology, and Implications for Mars, *47th Lunar and Planetary Science Conference*, (Abstract 2546).
- Blake, D. et al. (2012), Characterization and Calibration of the CheMin Mineralogical Instrument on Mars Science Laboratory, *Space Science Reviews*, 170(1-4), 341–399.
- Bodine, M. W., Jr, and T. H. Fernald (1973), EDTA dissolution of gypsum, anhydrite, and Ca-Mg carbonates, *Journal of Sedimentary Petrology*, 43(4), 1152–1156.
- Bristow, T. F. et al. (2015), The origin and implications of clay minerals from Yellowknife Bay,

- Gale crater, Mars, *American Mineralogist*, 100(4), 824–836.
- Brophy, G. P., E. S. Scott, and R. A. Snellgrove (1962), Sulfate Studies II. Solid Solution Between Alunite and Jarosite, *American Mineralogist*, 47(1-2), 112–126.
- Carr, M. H. (1996), *Water on Mars*, Oxford University Press, New York.
- Carr, M. H. (2002), Elevations of water-worn features on Mars: Implications for circulation of groundwater, *Journal of Geophysical Research*, 107(E12).
- Carr, M. H., and J. W. Head (2010a), Acquisition and history of water on Mars, in *Lakes on Mars*, pp. 31–67, Elsevier.
- Carr, M. H., and J. W. Head III (2010b), Geologic history of Mars, *Earth and Planetary Science Letters*, 294(3–4), 185–203.
- Cassi, C. (2008), ExoMars: The Enhanced Baseline Mission, *6th International Planetary Probe Workshop Conference Proceedings*.
- Cavanagh, P. D. et al. (2015), Confidence Hills Mineralogy and CheMin Results from Base of Mt. Sharp, Pahrump Hills, Gale Crater, Mars, *46th Lunar and Planetary Science Conference*, (Abstract 2735).
- Chevrier, V. F., and E. G. Rivera-Valentin (2012), Formation of recurring slope lineae by liquid brines on present-day Mars, *Geophysical Research Letters*, 39(21).
- Christensen, P. R. et al. (1998), Results from the Mars Global Surveyor Thermal Emission Spectrometer, *Science*, 279(5357), 1692–1698.
- Christensen, P. R. et al. (2003), Morphology and composition of the surface of Mars: Mars Odyssey THEMIS results, *Science*, 300(5628), 2056–2061.
- Christensen, P. R. et al. (2004), Mineralogy at Meridiani Planum from the Mini-TES Experiment on the Opportunity Rover, *Science*, 306(5702), 1733–1739.
- Cigolini, C., A. M. Kudo, D. G. Brookins, and D. Ward (1991), The petrology of Poas Volcano lavas: basalt-andesite relationship and their petrogenesis within the magmatic arc of Costa Rica, *Journal of Volcanology and Geothermal Research*, 48(3-4), 367–384.
- Cockell, C. S., and N. G. Barlow (2002), Impact Excavation and the Search for Subsurface Life on Mars, *Icarus*, 155(2), 340–349.
- Craddock, R. A., and A. D. Howard (2002), The case for rainfall on a warm, wet early Mars, *Journal of Geophysical Research*, 107(E11), 5111.
- Crumpler, L. S., R. E. Arvidson, D. W. Mittlefehldt, B. L. Jolliff, W. H. Farrand, V. Fox, and M. P. Golombek (2016), Opportunity, Geologic and Structural Context of Aqueous Alteration in Noachian Outcrops, Marathon Valley and Rim and Endeavour Crater, *47th Lunar and Planetary Science Conference*, (Abstract 2272).
- Dehouck, E., V. Chevrier, A. Gaudin, N. Mangold, P.-E. Mathé, and P. Rochette (2012), Evaluating the role of sulfide-weathering in the formation of sulfates or carbonates on Mars, *Geochimica et Cosmochimica Acta*, 90, 47–63.

- Di Achille, G., and B. M. Hynek (2010), Ancient ocean on Mars supported by global distribution of deltas and valleys, *Nature Geoscience*, 3(7), 459–463.
- Di Piazza, A., A. L. Rizzo, F. Barberi, M. L. Carapezza, G. De Astis, C. Romano, and F. Sortino (2015), Geochemistry of the mantle source and magma feeding system beneath Turrialba volcano, Costa Rica, *Lithos*, 232, 319–335.
- Doran, P. T., W. B. Lyons, and D. M. McKnight (2010), *Life in Antarctic Deserts and other Cold Dry Environments: Astrobiological Analogs*, Cambridge Astrobiology, Cambridge University Press.
- Drouet, C., K. L. Pass, D. Baron, S. Draucker, and A. Navrotsky (2004), Thermochemistry of jarosite-alunite and natrojarosite-natroalunite solid solutions, *Geochimica et Cosmochimica Acta*, 68(10), 2197–2205.
- Eberl, D. D., V. C. Farmer, and R. M. Barrer (1984), Clay Mineral Formation and Transformation in Rocks and Soils, *Philosophical Transactions of the Royal Society A: Mathematical, Physical and Engineering Sciences*, 311(1517), 241–257, doi:10.1098/rsta.1984.0026.
- Ehlmann, B. L., and J. F. Mustard (2012), An in-situ record of major environmental transitions on early Mars at Northeast Syrtis Major, *Geophysical Research Letters*, 39(11), doi:10.1029/2012GL051594.
- Ehlmann, B. L., J. F. Mustard, C. I. Fassett, S. C. Schon, J. W. Head III, D. J. Des Marais, J. a. Grant, and S. L. Murchie (2008), Clay minerals in delta deposits and organic preservation potential on Mars, *Nature Geoscience*, 1(6), 355–358.
- Ehlmann, B. L. et al. (2009), Identification of hydrated silicate minerals on Mars using MRO-CRISM: Geologic context near Nili Fossae and implications for aqueous alteration, *Journal of Geophysical Research*, 114(10), 1–33.
- Ehlmann, B. L., J. F. Mustard, and S. L. Murchie (2010), Geologic setting of serpentine deposits on Mars, *Geophysical Research Letters*, 37(6), doi:10.1029/2010GL042596.
- Ehlmann, B. L., J. F. Mustard, S. L. Murchie, J.-P. Bibring, A. Meunier, A. A. Fraeman, and Y. Langevin (2011), Subsurface water and clay mineral formation during the early history of Mars, *Nature*, 479(7371), 53–60.
- Ehlmann, B. L., G. Berger, N. Mangold, J. R. Michalski, D. C. Catling, S. W. Ruff, E. Chassefière, P. B. Niles, V. Chevrier, and F. Poulet (2013), Geochemical Consequences of Widespread Clay Mineral Formation in Mars' Ancient Crust, *Space Science Reviews*, 174(1-4), 329–364.
- Ehlmann, B. L. et al. (2016), Discovery of alunite in Cross crater, Terra Sirenum, Mars: Evidence for acidic, sulfurous waters, *American Mineralogist*, 101(7), 1527–1542.
- Elwood Madden, M. E., R. J. Bodnar, and J. D. Rimstidt (2004), Jarosite as an indicator of water-limited chemical weathering on Mars, *Nature*, 119(August), 821–824.
- Elwood Madden, M. E., A. S. Madden, J. D. Rimstidt, S. Zahrai, M. R. Kendall, and M. A. Miller (2012), Jarosite dissolution rates and nanoscale mineralogy, *Geochimica et Cosmochimica Acta*, 91, 306–321.

- Fairén, A. G. et al. (2010), Astrobiology through the ages of Mars: the study of terrestrial analogues to understand the habitability of Mars, *Astrobiology*, 10(8), 821–843.
- Farmer, J. D., and D. J. Des Marais (1999), Exploring for a record of ancient Martian life for Mars Exopaleontology, *Journal of Geophysical Research*, 104(E11), 26977–26995.
- Farrand, W. H., T. D. Glotch, J. W. Rice Jr., J. A. Hurowitz, and G. A. Swayze (2009), Discovery of jarosite within the Mawrth Vallis region of Mars: Implications for the geologic history of the region, *Icarus*, 204(2), 478–488.
- Farr, T. G. (2004), Terrestrial analogs to Mars: The NRC community decadal report, *Planetary and Space Science*, 52(1–3), 3–10.
- Fassett, C. I., and J. W. Head III (2008), Valley network-fed, open-basin lakes on Mars: Distribution and implications for Noachian surface and subsurface hydrology, *Icarus*, 198(1), 37–56.
- Fernández-Remolar, D. C., R. V. Morris, J. E. Gruener, R. Amils, and A. H. Knoll (2005), The Río Tinto Basin, Spain: Mineralogy, sedimentary geobiology, and implications for interpretation of outcrop rocks at Meridiani Planum, Mars, *Earth and Planetary Science Letters*, 240(1), 149–167.
- Fernández-Remolar, D. C., O. Prieto-Ballesteros, R. Amils, F. Gómez, L. Friedlander, R. Arvidson, R. V. Morris, and D. Gómez (2009), Production of phyllosilicates and sulfates on Mars through acidic weathering: the Rio Tinto Mars analog model, in *Bioastronomy 2007: Molecules, Microbes and Extraterrestrial Life*, vol. 420, edited by K. J. Meech, J. V. Keane, M. J. Mumma, J. L. Siefert, and D. J. Werthimer, pp. 129–134.
- Freissinet, C. et al. (2015), Organic molecules in the Sheepbed Mudstone, Gale Crater, Mars, *Journal of Geophysical Research: Planets*, 120, 495–514.
- Freissinet, C. et al. (2016), First Detection of Non-Chlorinated Organic Molecules Indigenous to a Martian Sample, *47th Lunar and Planetary Science Conference*, (2568).
- Gellert, R. et al. (2006), Alpha particle X-ray spectrometer (APXS): Results from Gusev crater and calibration report, *Journal of Geophysical Research*, 111(E2).
- Gendrin, A., N. Mangold, J.-P. Bibring, Y. Langevin, B. Gondet, G. Bonello, C. Quantin, J. F. Mustard, and R. E. Arvidson (2005), Sulfates in Martian Layered Terrains: The OMEGA / Mars Express View, *Science*, 307, 1587–1591.
- Glamoclija, M., L. Garrel, J. Berthon, and P. López-García (2004), Biosignatures and Bacterial Diversity in Hydrothermal Deposits of Solfatara Crater, Italy, *Geomicrobiology Journal*, 21(8), 529–541.
- Grotzinger, J. P. et al. (2012), Mars Science Laboratory Mission and Science Investigation, *Space Science Reviews*, 170, 5–56.
- Grotzinger, J. P. et al. (2014), A habitable fluvio-lacustrine environment at Yellowknife Bay, Gale crater, Mars, *Science*, 343(6169), 1242777.
- Grotzinger, J. P. et al. (2015), Deposition, exhumation, and paleoclimate of an ancient lake deposit, Gale crater, Mars, *Science*, 350(6257), doi:10.1126/science.aac7575.

- Hartmann, W. K., and G. Neukum (2001), Cratering chronology and the evolution of Mars, *Space Science Reviews*, 96, 165–194.
- Hassler, D. M. et al. (2014), Mars' surface radiation environment measured with the Mars Science Laboratory's Curiosity rover, *Science*, 343(6169), 1244797.
- Head, J. W., 3rd, H. Hiesinger, M. A. Ivanov, M. A. Kreslavsky, S. Pratt, and B. J. Thomson (1999), Possible ancient oceans on Mars: evidence from Mars Orbiter Laser Altimeter data, *Science*, 286(5447), 2134–2137.
- Hecht, M. H. et al. (2009), Detection of perchlorate and the soluble chemistry of martian soil at the Phoenix lander site, *Science*, 325(5936), 64–67.
- He, Q., L. Xiao, W. Hsu, J. B. Balta, H. Y. McSween, and Y. Liu (2013), The water content and parental magma of the second chassignite NWA 2737: Clues from trapped melt inclusions in olivine, *Meteoritics & Planetary Science*, 48(3), 474–492.
- Herrstrom, E. A., M. K. Reagan, and J. D. Morris (1995), Variations in lava composition associated with flow of asthenosphere beneath southern Central America, *Geology*, 23(7), 617–620.
- Howard, A. D., J. M. Moore, and R. P. Irwin (2005), An intense terminal epoch of widespread fluvial activity on early Mars: 1. Valley network incision and associated deposits, *Journal of Geophysical Research*, 110(E12S14), doi:10.1029/2005JE002459.
- Hynek, B. M., and R. J. Phillips (2003), New data reveal mature, integrated drainage systems on Mars indicative of past precipitation, *Geology*, 31(9), 757–760.
- Hynek, B. M., M. Beach, and M. R. T. Hoke (2010), Updated global map of Martian valley networks and implications for climate and hydrologic processes, *Journal of Geophysical Research*, 115(E9), E09008.
- Hynek, B. M., T. M. McCollom, E. C. Marcucci, K. Brugman, and K. L. Rogers (2013), Assessment of environmental controls on acid-sulfate alteration at active volcanoes in Nicaragua: Applications to relic hydrothermal systems on Mars, *Journal of Geophysical Research: Planets*, 118(10), 2083–2104.
- Hynek, B. M., T. M. McCollom, L. J. McHenry, and G. E. Alvarado (2014), Assessing Hydrothermal Alteration on Early Mars Through Analog Environments in Nicaragua, Costa Rica, Iceland, and Hawaii, *45th Lunar and Planetary Science Conference*, (2172).
- Jakosky, B. M. et al. (2015), The Mars Atmosphere and Volatile Evolution (MAVEN) Mission, *Space Science Reviews*, 195(1-4), 3–48.
- Klingelhöfer, G. et al. (2004), Jarosite and hematite at Meridiani Planum from Opportunity's Mossbauer Spectrometer, *Science*, 306(5702), 1740–1745.
- Langevin, Y., F. Poulet, J.-P. Bibring, and B. Gondet (2005), Sulfates in the North Polar Region of Mars Detected by OMEGA/Mars Express, *Science*, 307(5715), 1584–1586.
- Lentz, R. C. F., H. Y. McSween Jr, J. Ryan, and L. R. Riciputi (2001), Water in martian magmas: clues from light lithophile elements in shergottite and nakhlite pyroxenes, *Geochimica et Cosmochimica Acta*, 65(24), 4551–4565.

- Levin, G. V., and P. A. Straat (1976), Viking labeled release biology experiment: interim results, *Science*, 194(4271), 1322–1329.
- Levin, G. V., and P. A. Straat (1979), Viking Mars labelled release results, , 277(5694), 326–326.
- Lichtenberg, K. A. et al. (2010), Stratigraphy of hydrated sulfates in the sedimentary deposits of Aram Chaos, Mars, *Journal of Geophysical Research*, 115(E6), E00D17.
- Ling, Z., F. Cao, Y. Ni, Z. Wu, J. Zhang, and B. Li (2016), Correlated analysis of chemical variations with spectroscopic features of the K–Na jarosite solid solutions relevant to Mars, *Icarus*, 271, 19–29.
- Löhr, A. J., A. M. Laverman, M. Braster, N. M. van Straalen, and W. F. M. Röling (2006), Microbial communities in the world’s largest acidic volcanic lake, Kawah Ijen in Indonesia, and in the Banyupahit river originating from it, *Microbial Ecology*, 52(4), 609–618.
- Lowell, P. (1908), *Mars as the Abode of Life*, The Macmillan Company.
- Malin, M. C., and K. S. Edgett (2000), Evidence for recent groundwater seepage and surface runoff on Mars, *Science*, 288(5475), 2330–2335.
- Malin, M. C., and K. S. Edgett (2001), Mars Global Surveyor Mars Orbiter Camera: Interplanetary cruise through primary mission, *Journal of Geophysical Research*, 106(E10), 23429–23570.
- Malin, M. C., and K. S. Edgett (2003), Evidence for persistent flow and aqueous sedimentation on early Mars, *Science*, 302(5652), 1931–1934.
- van Manen, S. M. (2014), Hazard and risk perception at Turrialba volcano (Costa Rica); implications for disaster risk management, *Applied Geography*, 50, 63–73.
- Marlow, J. J., Z. Martins, and M. A. Sephton (2008), Mars on Earth: soil analogues for future Mars missions, *Astronomy and Geophysics*, 49(2), 2.20–2.23.
- McCanta, M. C., M. D. Dyar, and A. H. Treiman (2014), Alteration of Hawaiian basalts under sulfur-rich conditions: Applications to understanding surface-atmosphere interactions on Mars and Venus, *American Mineralogist*, 99(2-3), 291–302.
- McCullom, T. M., and B. M. Hynek (2005), A volcanic environment for bedrock diagenesis at Meridiani Planum on Mars, *Nature*, 438(7071), 1129–1131.
- McCullom, T. M., B. M. Hynek, K. L. Rogers, B. Moskowitz, and T. S. Berquó (2013a), Chemical and mineralogical trends during acid-sulfate alteration of pyroclastic basalt at Cerro Negro volcano and implications for early Mars, *Journal of Geophysical Research: Planets*, 118, 1719–1751.
- McCullom, T. M., M. Robbins, B. Moskowitz, T. S. Berquó, N. Jöns, and B. M. Hynek (2013b), Experimental study of acid-sulfate alteration of basalt and implications for sulfate deposits on Mars, *Journal of Geophysical Research: Planets*, 118, 577–614.
- McCullom, T. M., B. L. Ehlmann, A. Wang, B. M. Hynek, B. Moskowitz, and T. S. Berquó (2014), Detection of iron substitution in natroalunite-natrojarosite solid solutions and potential

- implications for Mars, *American Mineralogist*, 99(5-6), 948–964.
- McEwen, A. S., L. Ojha, C. M. Dundas, S. S. Mattson, S. Byrne, J. J. Wray, S. C. Cull, S. L. Murchie, N. Thomas, and V. C. Gulick (2011), Seasonal flows on warm Martian slopes, *Science*, 333(6043), 740–743.
- McEwen, A. S., C. M. Dundas, S. S. Mattson, A. D. Toigo, L. Ojha, J. J. Wray, M. Chojnacki, S. Byrne, S. L. Murchie, and N. Thomas (2013), Recurring slope lineae in equatorial regions of Mars, *Nature Geoscience*, 7(1), 53–58.
- McKay, D. S., E. K. Gibson Jr, K. L. Thomas-Keprta, H. Vali, C. S. Romanek, S. J. Clemett, X. D. Chillier, C. R. Maechling, and R. N. Zare (1996), Search for past life on Mars: possible relic biogenic activity in martian meteorite ALH84001, *Science*, 273(5277), 924–930.
- McSween, H. Y. et al. (2004), Basaltic rocks analyzed by the Spirit Rover in Gusev Crater, *Science*, 305(5685), 842–845.
- Michalski, J. R., J. Cuadros, P. B. Niles, J. Parnell, A. Deanne Rogers, and S. P. Wright (2013), Groundwater activity on Mars and implications for a deep biosphere, *Nature Geoscience*, 6(2), 133–138.
- Ming, D. W. et al. (2006), Geochemical and mineralogical indicators for aqueous processes in the Columbia Hills of Gusev crater, Mars, *Journal of Geophysical Research*, 111(E2), E02S12.
- Moore, D. M., and R. C. Reynolds (1997), *X-ray Diffraction and the Identification and Analysis of Clay Minerals*, Oxford University Press.
- de Moor, J. M., A. Aiuppa, J. Pacheco, G. Avar, C. Kern, M. Liuzzo, M. Martínez, G. Giudice, and T. P. Fischer (2016), Short-period volcanic gas precursors to phreatic eruptions: Insights from Poás Volcano, Costa Rica, *Earth and Planetary Science Letters*, 442, 218–227.
- Morris, R. V. et al. (2006), Mössbauer mineralogy of rock, soil, and dust at Gusev crater, Mars: Spirit's journey through weakly altered olivine basalt on the plains and pervasively altered basalt in the Columbia Hills, *Journal of Geophysical Research: Planets*, 111(E2).
- Morris, R. V. et al. (2016), Silicic volcanism on Mars evidenced by tridymite in high-SiO₂ sedimentary rock at Gale Crater, *Proceedings of the National Academy of Sciences*, doi:10.1073/pnas.1607098113.
- Murchie, S. L. et al. (2009), A synthesis of Martian aqueous mineralogy after 1 Mars year of observations from the Mars Reconnaissance Orbiter, *Journal of Geophysical Research*, 114(9), 1–30.
- Mustard, J. F., S. L. Murchie, S. M. Pelkey, B. L. Ehlmann, R. E. Milliken, J. A. Grant, J.-P. Bibring, F. Poulet, and J. Bishop (2008), Hydrated silicate minerals on Mars observed by the Mars Reconnaissance Orbiter CRISM instrument, *Nature*, 454(7202), 305–309.
- Mustard, J. F. et al. (2013), *Report of the Mars 2020 science definition team*, The Mars Exploration Program Analysis Group (MEPAG).
- Navarro-González, R. et al. (2003), Mars-like soils in the Atacama Desert, Chile, and the dry

- limit of microbial life, *Science*, 302(5647), 1018–1021.
- Navarro-González, R., E. Vargas, J. de La Rosa, A. C. Raga, and C. P. McKay (2010), Reanalysis of the Viking results suggests perchlorate and organics at midlatitudes on Mars, *Journal of Geophysical Research*, 115(E12).
- Noe Dobrea, E. Z., J. J. Wray, F. J. Calef, T. J. Parker, and S. L. Murchie (2012), Hydrated minerals on Endeavour Crater's rim and interior, and surrounding plains: New insights from CRISM data, *Geophysical Research Letters*, 39(23), L23201.
- Pace, N. R. (1997), A molecular view of microbial diversity and the biosphere, *Science*, 276(5313), 734–740.
- Papike, J. J., J. M. Karner, and C. K. Shearer (2006), Comparative planetary mineralogy: Implications of martian and terrestrial jarosite. A crystal chemical perspective, *Geochimica et Cosmochimica Acta*, 70(5), 1309–1321.
- Peters, G. H., W. Abbey, G. H. Bearman, and G. S. Mungas (2008), Mojave Mars simulant—Characterization of a new geologic Mars analog, *Icarus*.
- Polyak, V. J., and N. Güven (1996), Alunite, natroalunite and hydrated halloysite in carlsbad cavern and lechuguilla cave, new mexico, *Clays and Clay Minerals*, 44(6), 843–850.
- Polyak, V. J., W. C. McIntosh, P. P. Provencio, and N. Güven (2006), Alunite and Natroalunite Tell a Story – the Age and Origin of Carlsbad Cavern , Lechuguilla Cave , and Other Sulfuric-Acid Type Caves of the Guadalupe Mountains, in *Caves and Karst of Southeastern New Mexico*, pp. 203–210, New Mexico Geological Society Guidebook.
- Poulet, F. et al. (2005), Phyllosilicates on Mars and implications for early martian climate, *Nature*, 438(7068), 623–627.
- Poulet, F., C. Gomez, J.-P. Bibring, Y. Langevin, B. Gondet, P. Pinet, G. Belluci, and J. F. Mustard (2007), Martian surface mineralogy from Observatoire pour la Minéralogie, l'Eau, les Glaces et l'Activité on board the Mars Express spacecraft (OMEGA/MEx): Global mineral maps, *Journal of Geophysical Research*, 112(E8), E08S02.
- Prosser, J. T., and M. J. Carr (1987), Poas Volcano, Costa Rica: Geology of the summit region and spatial and temporal variations among the most recent lavas, *Journal of Volcanology and Geothermal Research*, 33(1-3), 131–146.
- Rampe, E. B. et al. (2015), Evidence for Acid-Sulfate Alteration in the Pahrump Hills Region, Gale Crater, Mars, *AGU Fall Meeting*.
- Rampe, E. B. et al. (2016), Diagenesis in the Murray Formation, Gale Crater, Mars, *47th Lunar and Planetary Science Conference*, (Abstract 2543).
- Reagan, M., E. Duarte, G. J. Soto, and E. Fernández (2006), The eruptive history of Turrialba volcano, Costa Rica, and potential hazards from future eruptions, *Geological Society of America Special Papers*, 412(13), 235–257.
- Rodriguez, J. A. P. et al. (2016), Tsunami waves extensively resurfaced the shorelines of an early Martian ocean, *Scientific Reports*, 6, 25106.

- Rogers, K. L., B. M. Hynek, and T. M. McCollom (2011), Photosynthesis within Mars' volcanic craters?: Insights from Cerro Negro Volcano, Nicaragua, *AGU Fall Meeting*.
- Rogers, K. L., B. M. Hynek, and T. M. McCollom (2013), Endolithic Microbial Communities in Mars Analog Volcanic Fumaroles, Cerro Negro Volcano, Nicaragua, *Analog Sites for Mars Missions II: Past, Present and Future Missions to Mars*, (Abstract 1738).
- Rull, F. et al. (2011), ExoMars Raman Laser Spectrometer for Exomars, in *Instruments, Methods, and Missions for Astrobiology XIV*, vol. 8152, edited by R. B. Hoover, P. C. W. Davies, G. V. Levin, and A. Y. Rozanov, pp. 81520J1–13.
- Saunders, R. S. et al. (2004), 2001 Mars Odyssey Mission Summary, in *2001 Mars Odyssey*, edited by C. T. Russell, pp. 1–36, Springer Netherlands.
- Seelos, K. D., R. E. Arvidson, B. L. Jolliff, S. M. Chemtob, R. V. Morris, D. W. Ming, and G. A. Swayze (2010), Silica in a Mars analog environment: Ka'u Desert, Kilauea Volcano, Hawaii, *Journal of Geophysical Research*, 115(E4).
- Silvestro, S., D. A. Vaz, G. Di Achille, I. C. Popa, and F. Esposito (2015), Evidence for different episodes of aeolian construction and a new type of wind streak in the 2016 ExoMars landing ellipse in Meridiani Planum, Mars, *Journal of Geophysical Research: Planets*, 120, 760–774.
- Siva Siddaiah, N., and K. Kumar (2009), Discovery of minamiite from the Deccan Volcanic Province, India: Implications for Martian surface exploration, *Current Science*, 97, 1664–1669.
- Sleep, N. H., and K. Zahnle (1998), Refugia from asteroid impacts on early Mars and the early Earth, *Journal of Geophysical Research*, 103(E12), 28529–28544.
- Smith, D. E. et al. (2001), Mars Orbiter Laser Altimeter: Experiment summary after the first year of global mapping of Mars, *Journal of Geophysical Research*, 106(E10), 23689–23722.
- Smith, P. H. et al. (2009), H₂O at the Phoenix landing site, *Science*, 325(5936), 58–61.
- Solomon, S. C., O. Aharonson, and J. M. Aurnou (2005), New perspectives on ancient Mars, *Science*, 307(5713), 1214–1220.
- Squyres, S. et al. (2004a), In situ evidence for an ancient aqueous environment at Meridiani Planum, Mars, *Science*, 306(5702), 1709–1714.
- Squyres, S. et al. (2012), Ancient impact and aqueous processes at Endeavour Crater, Mars, *Science*, 336(6081), 570–576.
- Squyres, S. W., and A. H. Knoll (2005), Sedimentary rocks at Meridiani Planum: Origin, diagenesis, and implications for life on Mars, *Earth and Planetary Science Letters*, 240(1), 1–10.
- Squyres, S. W. et al. (2004b), The Spirit Rover's Athena science investigation at Gusev Crater, Mars, *Science*, 305(5685), 794–799.
- Squyres, S. W. et al. (2006), Rocks of the Columbia Hills, *Journal of Geophysical Research: Planets*, 111(E2), doi:10.1029/2005JE002562.

- Squyres, S. W. et al. (2008), Detection of Silica-Rich Deposits on Mars, *Science*, 320, 1064–1067.
- Stern, J. C. et al. (2013), Isotopic and geochemical investigation of two distinct Mars analog environments using evolved gas techniques in Svalbard, Norway, *Icarus*, 224(2), 297–308.
- Stoffregen, R. E., C. N. Alpers, and J. L. Jambor (2000), Alunite-Jarosite Crystallography, Thermodynamics, and Geochronology, *Reviews in Mineralogy and Geochemistry*, 40(1), 453–479.
- Sumner, D. Y. (2004), Poor preservation potential of organics in Meridiani Planum hematite-bearing sedimentary rocks, *Journal of Geophysical Research*, 109(E12).
- Thollot, P., N. Mangold, V. Ansan, S. Le Mouélic, R. E. Milliken, J. L. Bishop, C. M. Weitz, L. H. Roach, J. F. Mustard, and S. L. Murchie (2012), Most Mars minerals in a nutshell: Various alteration phases formed in a single environment in Noctis Labyrinthus, *Journal of Geophysical Research*, 117(E11), doi:10.1029/2011JE004028.
- Titus, T. N., H. H. Kieffer, and P. R. Christensen (2003), Exposed water ice discovered near the south pole of Mars, *Science*, 299(5609), 1048–1051.
- Tosca, N. J. (2004), Acid-sulfate weathering of synthetic Martian basalt: The acid fog model revisited, *Journal of Geophysical Research*, 109(E5), E05003.
- Treiman, A. H. (2005), The nakhlite meteorites: Augite-rich igneous rocks from Mars, *Chemie der Erde - Geochemistry*, 65(3), 203–270.
- Treiman, A. H., K. L. Robinson, D. F. Blake, and D. Bish (2010), Mineralogy Determinations by CheMin XRD, Tested on Ultramafic Rocks (Mantle Xenoliths), *41st Lunar and Planetary Science Conference*, (Abstract 1472).
- Treiman, A. H., D. L. Bish, D. T. Vaniman, S. J. Chipera, D. F. Blake, D. W. Ming, and Morris (2016), Mineralogy, provenance, and diagenesis of a potassic basaltic sandstone on Mars: CheMin X-ray diffraction of the Windjana sample (Kimberley area, Gale Crater) Allan, *Journal of Geophysical Research: Planets*, 121, 75–106.
- Vago, J. L., and G. Kminek (2007), Putting Together an Exobiology Mission: The ExoMars Example, in *Complete Course in Astrobiology*, edited by G. Horneck and P. Rettberg, pp. 321–351, Wiley.
- Vaniman, D. et al. (2014), Mineralogy of a mudstone at Yellowknife Bay, Gale crater, Mars, *Science*, 343(6169), 1243480.
- Weitz, C. M., R. E. Milliken, J. A. Grant, A. S. McEwen, R. M. E. Williams, J. L. Bishop, and B. J. Thomson (2010), Mars Reconnaissance Orbiter observations of light-toned layered deposits and associated fluvial landforms on the plateaus adjacent to Valles Marineris, *Icarus*, 205(1), 73–102.
- Weitz, C. M., J. L. Bishop, P. Thollot, N. Mangold, and L. H. Roach (2011), Diverse mineralogies in two troughs of Noctis Labyrinthus, Mars, *Geology*, 39(10), 899–902.
- Whiteway, J. A. et al. (2009), Mars water-ice clouds and precipitation, *Science*, 325(5936), 68–70.

- Wray, J. J., E. Z. Noe Dobrea, R. E. Arvidson, S. M. Wiseman, S. W. Squyres, A. S. McEwen, J. F. Mustard, and S. L. Murchie (2009), Phyllosilicates and sulfates at Endeavour Crater, Meridiani Planum, Mars, *Geophysical Research Letters*, *36*(21), 1–5.
- Wray, J. J. et al. (2011), Columbus crater and other possible groundwater-fed paleolakes of Terra Sirenum, Mars, *Journal of Geophysical Research*, *116*(E1).
- Wray, R. A. (2011), Alunite formation within silica stalactites from the Sydney Region, South-eastern Australia, *International Journal of Speleology*, *40*(2), 109–116.
- Yen, A. et al. (2008), Hydrothermal processes at Gusev Crater: An evaluation of Paso Robles class soils, *Journal of Geophysical Research*, *113*(E6).